

REPORT DOCUMENTATION PAGE			Form Approved OMB No. 0704-0188	
Public reporting burden for this collection of information is estimated to average 1 hour per response, including the time for reviewing instructions, searching existing data sources, gathering and maintaining the data needed, and completing and reviewing the collection of information. Send comments regarding this burden estimate or any other aspect of this collection of information, including suggestions for reducing this burden, to Washington Headquarters Services, Directorate for Information Operations and Reports, 1215 Jefferson Davis Highway, Suite 1204, Arlington, VA 22202-4302, and to the Office of Management and Budget, Paperwork Reduction Project (0704-0188), Washington, DC 20503.				
1. AGENCY USE ONLY (Leave blank)		2. REPORT DATE 05/01/01		3. REPORT TYPE AND DATES COVERED Final Technical, 01/01/93 - 09/30/98
4. TITLE AND SUBTITLE Numerical Study of Three-Dimensional Turbulent Flows			5. FUNDING NUMBERS G: N00014-94-1-0016	
6. AUTHORS John Kim				
7. PERFORMING ORGANIZATION NAME(S) AND ADDRESS(ES) Mechanical and Aerospace Engineering Department 48-121 Engineering IV, Box 951597 University of California, Los Angeles Los Angeles, CA 90095-1597			8. PERFORMING ORGANIZATION REPORT NUMBER	
9. SPONSORING/MONITORING AGENCY NAME(S) AND ADDRESS(ES) ONR 800 North Quincy Street Ballston Tower One, Code 333 Arlington, VA 22217-5660			10. SPONSORING/MONITORING AGENCY REPORT NUMBER	
11. SUPPLEMENTARY NOTES The views, opinions and/or findings contained in this report are those of the author(s) and should not be construed as an official Department of the Navy position, policy or decision, unless so designated by other documentation.				
12a. DISTRIBUTION/AVAILABILITY STATEMENT Approved for public release; distribution unlimited			12b. DISTRIBUTION CODE UL	
13. ABSTRACT (Maximum 200 words) Direct numerical and large-eddy simulations were used to perform 'numerical experiments' relevant to the cases of interest. We employ a plane-channel geometry and impose mean-flow perturbations by subjecting fully developed 2D Poiseuille flow to irrotational deformations and/or in-plane motion of the channel walls. The former corresponds to outer-layer strains induced in boundary layers by pressure gradients, the latter to sudden variations in the near-wall region, caused by either step changes in the surface conditions or the combination of an outer-layer change and the no-slip boundary condition. This combination allows the physics of a broad class of spatially developing wall shear layers to be duplicated with a temporally evolving channel flow. The temporal computations can be realized much more effectively than can simulations of a spatial boundary layer, providing a much more extensive study for a given cost. As a consequence, we can consider a wide variety of mean-flow perturbations. Moreover, since mean statistics for these flows satisfy a one-dimensional unsteady problem that contains the essential features of the spatial flow, they provide an efficient means of testing one-point closure models.				
14. SUBJECT TERMS Direct numerical simulations, large-eddy simulations, 2D Poiseuille flow, turbulence modeling data			15. NUMBER OF PAGES 68	
			16. PRICE CODE	
17. SECURITY CLASSIFICATION OF REPORT Unclassified	18. SECURITY CLASSIFICATION OF THIS PAGE Unclassified	19. SECURITY CLASSIFICATION OF ABSTRACT Unclassified	20. LIMITATION OF ABSTRACT UL	

Final Report

NUMERICAL STUDY OF THREE-DIMENSIONAL TURBULENT FLOWS

John Kim

Mechanical and Aerospace Engineering Department

University of California, Los Angeles

Los Angeles, CA 90095-1597

310-825-4393 (voice), 310-206-4830 (fax), jkim@seas.ucla.edu (e-mail)

Grant N00014-94-1-0016

ONR Program Officer: Dr. Patrick L. Purtell

Research Objectives:

Obtain a deeper understanding of the fundamental physics of turbulent flows subjected to mean three-dimensionality, with an eye toward improving the accuracy of the engineering turbulence models used to predict them.

Science & Technology (S&T) Objectives:

- 1) Investigate the effect of various three-dimensional mean-flow perturbations ('extra strains') upon the structure and statistics of turbulent boundary layers.
- 2) Provide an extensive high-quality turbulence modeling database, which can be used to test and develop large-eddy simulation and Reynolds-averaged closures.

Summary:

Direct numerical and large-eddy simulations were used to perform 'numerical experiments' relevant to the cases of interest. We employ a plane-channel geometry and impose mean-flow perturbations by subjecting fully developed 2D Poiseuille flow to irrotational deformations and/or in-plane motion of the channel walls. The former corresponds to outer-layer strains induced in boundary layers by pressure gradients, the latter to sudden variations in the near-wall region, caused by either step changes in the surface conditions or the combination of an outer-layer change and the no-slip boundary condition. This combination allows the physics of a broad class of spatially developing wall shear layers to be duplicated with a temporally evolving channel flow. The temporal computations can be realized much more effectively than can simulations of a spatial boundary layer, providing a much more extensive study for a given cost. As a consequence, we can consider a wide variety of mean-flow perturbations. Moreover, since mean statistics for these flows satisfy a one-dimensional unsteady problem that contains the essential features of the spatial flow, they provide an efficient means of testing one-point closure models.

We have been able to understand and explain a range of 2D and 3D extra-strain effects – some of which are counter-intuitive and difficult for current turbulence models to duplicate – while creating an extensive set of unique and valuable turbulence modeling data. Further details of our findings are described in the attached papers.

A numerical study of strained three-dimensional wall-bounded turbulence

By G. N. COLEMAN¹†, J. KIM¹ AND P. R. SPALART²

¹Mechanical and Aerospace Engineering Department, UCLA, 48-121 Engr. IV,
Box 951597, Los Angeles, CA 90095-1597, USA

²Boeing Commercial Airplanes, PO Box 3707, Seattle, WA 98124-2207, USA

(Received 22 July 1999 and in revised form 6 March 2000)

Channel flow, initially fully developed and two-dimensional, is subjected to mean strains that emulate the effect of rapid changes of streamwise and spanwise pressure gradients in three-dimensional boundary layers, ducts, or diffusers. As in previous studies of homogeneous turbulence, this is done by deforming the domain of a direct numerical simulation (DNS); here however the domain is periodic in only two directions and contains parallel walls. The velocity difference between the inner and outer layers is controlled by accelerating the channel walls in their own plane, as in earlier studies of three-dimensional channel flows. By simultaneously moving the walls and straining the domain we duplicate both the inner and outer regions of the spatially developing case. The results are used to address basic physics and modelling issues. Flows subject to impulsive mean three-dimensionality with and without the mean deceleration of an adverse pressure gradient (APG) are considered: strains imitating swept-wing and pure skewing (sideways turning) three-dimensional boundary layers are imposed. The APG influences the structure of the turbulence, measured for example by the ratio of shear stress to kinetic energy, much more than does the pure skewing. For both deformations, the evolution of the Reynolds stress is profoundly affected by changes to the velocity–pressure-gradient correlation Π_{ij} . This term—which represents the finite time required for the mean strain to modify the shape and orientation of the turbulent motions—is primarily responsible for the difference (lag) in direction between the mean shear and the turbulent shear stresses, a well-known feature of perturbed three-dimensional boundary layers. Files containing the DNS database and model-testing software are available from the authors for distribution, as tools for future closure-model testing.

1. Introduction

The subject of this study is turbulent three-dimensional boundary layers (3DBLs), that is boundary layers with mean velocity profiles that change direction with distance from the surface. As a consequence, the mean velocity and mean vorticity are not everywhere orthogonal as they are in two-dimensional boundary layers. Our objective is to better understand the non-equilibrium case, where the 3DBL is created by an abrupt mean-flow perturbation. (We shall use ‘perturbed’ and ‘non-stationary’ as synonyms for the traditional meaning of non-equilibrium, to describe a flow subjected to a rapid change of the mean field to which the turbulence has not yet adjusted.)

† Present address: School of Engineering Sciences, Aeronautics and Astronautics, University of Southampton, Highfield, Southampton SO17 1BJ, UK.

These flows are abundant in both meteorology and engineering (Smits & Wood 1985). Although stationary 3DBLs (such as the Ekman layer) are not without importance and physical complexity (see e.g. Spalart 1989; Littell & Eaton 1994; Wu & Squires 1997; Coleman 1999), it is the transient response of the turbulence to an impulsively imposed mean deformation that is the most challenging to understand, and is the subject of this investigation. Specifically, we examine the transition of a statistically stationary two-dimensional incompressible turbulent flow to non-stationary states created by sudden application of three-dimensional mean strains. The focus here is upon the resulting statistics (rather than the behaviour of the instantaneous coherent-structures[†]), with an eye toward improving the performance of one-point turbulence models. Similar, less thorough, presentations of this work have appeared in Coleman, Kim & Spalart (1996*b*, 1997).

Since turbulence is inherently unsteady and three-dimensional, it might seem reasonable to assume that the three-dimensionality of the mean flow is irrelevant. Turbulence in perturbed 3DBLs would then be a simple extension of that found in stationary two-dimensional or three-dimensional boundary layers. It is not. There is now abundant evidence that suddenly adding mean three-dimensionality to a flow alters its character. (Reviews of stationary and perturbed turbulent 3DBL experiments and simulations can be found in Fernholz & Vagt 1981; van den Berg *et al.* 1988; Schwarz & Bradshaw 1994; Eaton 1995; or Johnston & Flack 1996). As an example, when a fully developed two-dimensional boundary layer is suddenly subjected to a spanwise mean shear by the impulsive motion of the surface, the flow often experiences a decrease of turbulent shear stress and drag (Moin *et al.* 1990; Jung, Mangiavacchi & Akhavan 1992; Laadhari, Skandaji & Morel 1994; Coleman, Kim & Le 1996*a*). Because addition of mean shear usually causes the turbulence to become more energetic, this behaviour is difficult to explain (and predict). We hope to clarify this phenomenon.

When the crossflow appears not because of applied surface shear but as the result of a spanwise pressure gradient, such as that found in a curved duct, upstream of a blunt obstacle, or over a swept wing, the 'streamwise component' of turbulent shear stress, $-\overline{u'v'}$, near the wall again tends to decrease (Bradshaw & Pontikos 1985); away from the surface, however, the stress typically increases (Pierce & Duerson 1975; Anderson & Eaton 1989; Schwarz & Bradshaw 1994; Ölçmen & Simpson 1995), presumably due to the outer-layer deformation associated with the mean streamwise pressure gradient. (More on this point below.) The suddenly distorted 3DBL therefore demonstrates a complexity associated with all perturbed boundary layers, in that the regions away from and very near the wall are dominated by separate inner- and outer-layer dynamics (Smits & Wood 1985).

Mean three-dimensionality is most fundamentally quantified not by the mean crossflow but by the non-zero mean streamwise vorticity associated with the mean spanwise shear $\partial W/\partial y$. (The x , y , and z coordinates, with corresponding U , V , and W velocity components, are used throughout to respectively denote the streamwise, wall-normal, and spanwise directions, with respect to a two-dimensional reference flow for which W is identically zero. In other coordinate systems non-zero $\partial W/\partial y$ might simply correspond to a two-dimensional flow directed away from the x -axis, and therefore not necessarily represent a lack of orthogonality of the mean velocity and mean vorticity, as it does here.) In the course of examining the impact of mean-flow changes upon the inner and outer regions, it is useful to differentiate between two types

[†] The effect of mean three-dimensionality upon the near-wall turbulence structures has been studied by Sendstad & Moin (1992), Littell & Eaton (1994), Kang, Choi & Yoo (1998), Le, Coleman & Kim (1999), Kiesow & Plesniak (1999), and Le (1999).

of perturbed 3DBL found in practice, according to the manner in which mean three-dimensionality (that is, $\partial W/\partial y$) is introduced to the flow. In the first, the pressure-driven variety,[†] $\partial W/\partial y$ appears in the outer layer because of inviscid skewing arising from streamwise variations of the mean spanwise pressure gradient. Mean streamwise vorticity (i.e. $\partial W/\partial y$) is induced by the irrotational strain $\partial W/\partial x = \partial U/\partial z$ (such that $\Omega_y \equiv 0$) which 'scissors' (rotates in opposite directions) the mean velocity U and mean vorticity Ω vectors in the streamwise-spanwise (x, z) plane: the initial spanwise mean vorticity ($\partial U/\partial y$) is redirected such that it has a streamwise component ($\partial W/\partial y$) (Bradshaw 1987); see figure 3(a) below. This case includes the curved-duct, blunt-obstacle, and swept-wing experiments mentioned above. The other type of perturbed 3DBL is the mean-shear-driven version, for which spanwise shear is generated in the inner layer by a step change in surface conditions. The rotating-cylinder experiments of Furuya, Nakamura & Kawachi (1966), Lohmann (1976) and Driver & Hebbbar (1991) (which involve longitudinal flow along the cylinder recovering from or first encountering a rotating section) fall into this category, as do the plane spanwise-moving-wall studies of Moin *et al.* (1990), Sendstad & Moin (1992), Jung *et al.* (1992), Laadhari *et al.* (1994), Howard & Sandham (1996), Coleman *et al.* (1996a), Kiesow & Plesniak (1999), and Le (1999). Our interest here is in the pressure-driven case, but we will still have occasion to consider shear-driven effects. Even in pressure-driven 3DBLs, near the surface $\partial W/\partial y$ is created by a shearing force, as the no-slip boundary condition affects the accelerating spanwise flow (figure 1b). Consequently outer-layer strains contain both irrotational and vortical components (representing respectively the direct and indirect effect of the skewing), while those near the surface (where skewing is negligible) are essentially vortical (i.e. rotational). That both types of 3DBL experience mean spanwise shear near the wall raises the possibility that the near-wall physics of the two flows are similar—which would explain the inner-layer reduction of $-u'v'$ mentioned above, observed in 3DBL experiments with and without a spanwise pressure gradient. Addressing this issue is another goal of this work.

A consistent trend in all perturbed 3DBLs is a reduction of the ratio of the magnitude of the Reynolds shear stress to the turbulence kinetic energy, compared to the initial equilibrium two-dimensional state. As pointed out by Schwarz & Bradshaw (1994), this alteration of the statistical structure of the flow implies that the turbulence becomes less efficient in extracting energy from the mean after $\partial W/\partial y$ has appeared, presumably as the result of the imposed strain deforming the turbulent eddies compared to the natural shape that they develop in two-dimensional flow. However, other types of outer-layer strains—notably those due to adverse pressure gradients (APGs)—are also known to diminish the stress/energy ratio (Nagano, Tagawa & Tsuji 1991; Spalart & Watmuff 1993; Coleman *et al.* 1997). Further complicating the picture is the fact that most (if not all) practical 3DBLs are subject to a combination of spanwise (inviscid skewing) and streamwise (APG) strains, so it is hard to distinguish between stress/energy ratio reductions that are caused by streamwise deceleration and those due solely to mean crossflow. Schwarz & Bradshaw addressed this challenge by designing an experiment in which the streamwise pressure gradient $\partial P/\partial x$ was minimized along the centreline of their curved wind tunnel; since they found a reduction of the stress/energy ratio in the centreline plane, it appears that mean spanwise shear (either in its near-wall form, or because of the outer-layer skewing) is sufficient to modify the turbulence structure. However, since $\partial P/\partial x$ is non-zero at spanwise locations on either side of the centreline in the Schwarz & Bradshaw flow,

[†] Also known as skew-induced, or Prandtl's first kind of secondary flow (Bradshaw 1987).

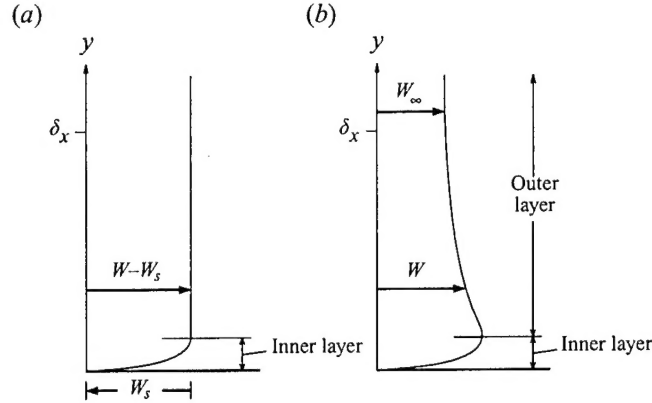


FIGURE 1. Non-stationary spanwise (lateral) mean velocity profiles in three-dimensional boundary layers. (a) Mean-shear-driven case: lateral flow created by surface moving with velocity W_s . (b) Pressure-driven case: lateral flow is an indication of non-zero $\partial W/\partial x$, which is created directly by spanwise mean pressure gradient $\partial P/\partial z$ (cf. figure 3a). In the outer layer spanwise shear $\partial W/\partial y$ is due to inviscid skewing of $\partial U/\partial y$; in the inner layer $\partial W/\partial y$ is caused by the no-slip condition on W . (Thickness of streamwise boundary layer denoted by δ_x .)

the possibility of the turbulence being affected by non-skewing deformations cannot be entirely ruled out. Moreover, the experimental findings of Gleyzes *et al.* (1993) and Webster, DeGraaff & Eaton (1996) (who respectively studied flows over a finite swept wing and a swept bump) suggest that pressure-driven 3DBLs may be much more sensitive to APG-induced strains (streamwise deceleration $\partial U/\partial x < 0$ and/or wall-normal divergence $\partial V/\partial y$) than to $\partial W/\partial y$. In what follows we attempt to quantify the ability of the mean skewing- and normal-strain components to separately alter the 3DBL turbulence.

Another ambiguity we hope to help resolve is that surrounding the development of the turbulent shear stresses in perturbed 3DBLs. A well-known feature of both the shear- and pressure-driven flows is the tendency for the stresses to lag behind the mean shear: the 'spanwise' component $-v'w'$ grows very slowly (Bradshaw & Pontikos 1985; Driver & Hebbbar 1987, 1991), and the spanwise-to-streamwise shear-stress ratio $v'w'/u'v'$ is usually much smaller than the corresponding mean velocity-gradient ratio, $(\partial W/\partial y)/(\partial U/\partial y)$. This lack of alignment between the Reynolds stress and mean shear also exists in stationary 3DBLs (see for example figure 14 of Coleman, Ferziger & Spalart 1990) but is generally largest immediately after $\partial W/\partial y$ appears in an initially stationary two-dimensional flow, as the inertia of the turbulent motions prevents them from instantly realigning with the direction of the new mean strain. The stress/strain misalignment cannot be captured by any turbulence model that assumes an isotropic (scalar) eddy viscosity, and thus represents a clear-cut inconsistency for many popular turbulence model closures. To overcome this difficulty one must understand which terms in the Reynolds-stress transport equation are responsible for slowing the growth of $-v'w'$, and how those terms are affected by various mean deformations—two objectives that are undertaken below.

Each of the issues outlined above is addressed by employing direct numerical simulation (DNS) of a parallel-flow approximation to the 3DBL; as explained in §2, we associate changes in time of a three-dimensional wall-bounded shear flow (3DWL, for 'three-dimensional wall layer') with convective changes of the spatially developing case of interest. Although we do not exactly recreate any existing experimental flows

using this approach, we can duplicate their defining features and connect various causes and effects in a straightforward manner. Other advantages and limitations are detailed below. The aims of this paper are to motivate and describe the numerical approach, apply it to two three-dimensional cases, and determine the general physical and modelling implications of the results, especially regarding the issues just discussed. Testing of specific turbulence models is deferred to future studies.

After introducing and formulating the strained-channel approach in the next section, the physical and numerical parameters used to obtain the DNS results are given. Two cases are simulated, one corresponding to a pressure-driven 3DBL with no APG, the other to the decelerated and skewed boundary layer over a 45° infinite swept wing. We examine the temporal evolution of the mean statistics and Reynolds-stress budgets in §3, finding that 3DWL turbulence is much more sensitive to mean streamwise-deceleration strains than it is to the mean spanwise shear. The critical role played by the velocity–pressure-gradient terms Π_{ij} (see equation (3.2) below) in the evolution of the Reynolds-stress budgets is also documented. Finally, closing remarks are presented in §4 regarding the broader implications of this study.

2. Approach

2.1. Overview

We create a perturbed 3DWL by imposing a mean strain rate and a change of the driving pressure gradient upon turbulence that had previously been in a statistically stationary state. Incompressible turbulent two-dimensional plane channel flow is subjected to spatially uniform divergence-free irrotational distortions characteristic of those induced in the outer region of turbulent boundary layers by pressure gradients. Solutions are obtained using DNS to resolve all relevant scales of motion, so no turbulence or subgrid-scale model is needed.

This strained-channel strategy is based on the observation that the pertinent characteristic of the pressure-driven boundary layer is not the pressure gradient as such, but the mean strains (such as the $\partial W/\partial x = \partial U/\partial z$ skewing, and $\partial U/\partial x = -\partial V/\partial y < 0$ deceleration) that they cause. We utilize a three-dimensional flow domain that is spatially periodic in the streamwise x and spanwise z directions and has two no-slip plane walls, and approximate the real spatially developing problem with a temporally evolving one. The channel turbulence is subjected to mean-flow variations in time that correspond to convective changes experienced by the turbulence in a boundary layer. The defining features of spatially developing pressure-driven shear layers are thereby captured in a wall-bounded flow that maintains its streamwise and spanwise homogeneity. When averages are discussed we use U and \bar{u} respectively to denote the imposed deformations, and the temporally evolving profiles in the channel (sampling over the directions parallel to the walls, and referring velocities to the local wall value). The streamwise/spanwise homogeneity is the reason explicit strains must be added to emulate the pressure-driven flow. Merely applying a spanwise pressure gradient (which is uniform in space by definition) in the channel results in a purely shear-driven 3DWL (cf. Moin *et al.* 1990)—since the effect of a spatially uniform pressure gradient in one direction is equivalent to an acceleration of the channel walls in the other (Sendstad & Moin 1992). (The distinction between previous and present three-dimensional channel flows is thus illustrated in figure 1: the shear-driven case (figure 1a) corresponds to the spanwise pressure-gradient/moving-wall DNS of Moin *et al.* (1990) and Coleman *et al.* (1996a), the pressure-driven case (figure 1b) to

the present simulations.) A primary test of the correctness of this approach will be verification that the outer-layer mean velocity profiles evolve according to the Squire–Winter–Hawthorne (SWH) criterion in the appropriate limits† (Squire & Winter 1951; Hawthorne 1951, 1954; Bradshaw 1987).

The imposed strain field is given by the divergence-free irrotational deformation,

$$\mathcal{A}_{ij} \equiv \frac{\partial U_i}{\partial x_j} = \begin{bmatrix} \partial U/\partial x & 0 & \partial U/\partial z \\ 0 & \partial V/\partial y & 0 \\ \partial W/\partial x & 0 & \partial W/\partial z \end{bmatrix}, \quad (2.1a)$$

where

$$\mathcal{A}_{ii} = \mathcal{A}_{11} + \mathcal{A}_{22} + \mathcal{A}_{33} = 0, \quad \text{and} \quad \mathcal{A}_{13} = \mathcal{A}_{31}. \quad (2.1b,c)$$

This form is chosen so that the y (wall-normal) direction is a principal axis of the strain tensor (hence the four zeros in (2.1a)). Because of the irrotationality constraint (2.1c) the imposed mean strain $\mathcal{S}_{ij} = \frac{1}{2}(\mathcal{A}_{ij} + \mathcal{A}_{ji})$ is equivalent to \mathcal{A}_{ij} . Each component \mathcal{A}_{ij} is assumed to be a function of time only, and therefore uniform in space. Spatial uniformity of \mathcal{A}_{ij} in the streamwise and spanwise directions is consistent with homogeneity. The lack of y dependence maintains a rectangular domain, as required by the code. We use only simple time histories here, in which the strain is off until time zero and constant from then on. (A broader range of perturbed flows could also be considered simply by imposing a series of distinct $\partial \mathcal{A}_{ij}/\partial t = 0$ phases one after the other, or by suddenly removing the constant strain and examining the return toward the fully developed two-dimensional state. When less-sudden perturbations are desired, the strain rate could be gradually applied, with for example \mathcal{A}_{ij} increasing smoothly from zero at $t = 0$ to an asymptotic value at finite time.) The strain supplies a continuous source of momentum and energy to the flow, as well as a redistribution of energy between components (see equations (2.7a), (2.10a) and (3.3b) below).

There are three independent strain parameters in (2.1a). The rates of stretching or compression in the wall-normal direction y and in two mutually orthogonal directions in the (x, z) -plane all sum to zero, thus defining the first two parameters. The third is the orientation (defined by the ‘angle of sweep’—so termed for reasons given in the next section) of the horizontal stretching/compression axis with respect to x , the direction of the initial two-dimensional flow. When this angle is zero, the (x, z) coordinates coincide with the principal axes of the horizontal plane strain, and $\mathcal{A}_{13} = \mathcal{A}_{31} = 0$. Although these three outer quantities, which are associated with the distorting or warping influence of the mean pressure gradient, completely determine the behaviour of the flow away from the surface, there are two more parameters needed in order to fully represent the impact of pressure-gradient $\nabla \mathcal{P}$ variations. They quantify the ‘bulk’ effect of $\nabla \mathcal{P}$ as it accelerates/decelerates the core of the channel flow, which in turn creates a viscous internal layer at the surface that diffuses into the outer layer as the flow develops (Smits & Wood 1985; Bradshaw 1987). A description of these two inner parameters follows.

The relationship between the temporally evolving and spatial flows is quantified by defining a vector $\mathbf{U}_{\text{avg}} = (U_{\text{avg}}, W_{\text{avg}})$ that is representative of the mean velocity in the outer layers of both flows. The time derivative of our flow, $\partial/\partial t$, approximates the material derivative $U_{\text{avg}}\partial/\partial x + W_{\text{avg}}\partial/\partial z$ in the spatial case. We further associate the three straining parameters in (2.1a), \mathcal{A}_{11} , \mathcal{A}_{33} , and $\mathcal{A}_{13} = \mathcal{A}_{31}$, with the strains imposed in the free stream of the 3DBL, $\partial U_{\infty}/\partial x$, $\partial W_{\infty}/\partial z$, and $\partial U_{\infty}/\partial z = \partial W_{\infty}/\partial x$,

† The agreement cannot be exact, since only inviscid terms enter the SWH prediction.

respectively. We assume that the strain rates in the outer layer of the 3DBL are close to those in the free stream, which is justified by their relatively large magnitude (compared to the outer-layer shear, or equivalently the timescale of the large eddies) and the small defect found in practice particularly at high Reynolds numbers; in other words $(U_{\text{avg}}, W_{\text{avg}}) \approx (U_\infty, W_\infty)$.

Each point of the flow volume is affected by the strain (see figures 3c and 14c). We are distorting the fluid and the computational box consisting of the periodic boundaries in x and z , and the two walls at $y = \pm\delta(t)$, where δ is the channel half-width, which when $\mathcal{A}_{22} \neq 0$ is a function of time. Physically the channel walls have become elastic impervious membranes, which remain plane and parallel and continue to enforce the no-slip condition. The fact that the walls are elastic slightly obscures the comparison between the near-wall regions of the present and actual pressure-driven boundary layers, making this study most relevant to the behaviour of the outer layer. But since typical 3DBL strains are weak compared with the shear rate near the wall (and therefore the inverse of the turbulence time scale), it is possible to draw conclusions about the near-wall layer as well.

It is helpful to differentiate between the irrotational and vortical mean fields. The former is prescribed solely by \mathcal{A}_{ij} , while the latter is due to wall-normal variations of the mean streamwise \bar{u} and spanwise \bar{w} velocity between the walls:

$$\mathcal{S}_{ij} = \begin{bmatrix} \mathcal{A}_{11} & 0 & \mathcal{A}_{13} \\ 0 & \mathcal{A}_{22} & 0 \\ \mathcal{A}_{31} & 0 & \mathcal{A}_{33} \end{bmatrix} + \begin{bmatrix} 0 & \frac{1}{2}\partial\bar{u}/\partial y & 0 \\ \frac{1}{2}\partial\bar{u}/\partial y & 0 & \frac{1}{2}\partial\bar{w}/\partial y \\ 0 & \frac{1}{2}\partial\bar{w}/\partial y & 0 \end{bmatrix}, \quad (2.2a)$$

but $\boldsymbol{\Omega} = \nabla \times (\mathbf{U} + \bar{\mathbf{u}})$ is

$$\Omega_i = \begin{pmatrix} 0 \\ 0 \\ 0 \end{pmatrix} + \begin{pmatrix} \partial\bar{w}/\partial y \\ 0 \\ -\partial\bar{u}/\partial y \end{pmatrix} = \bar{\omega}_i, \quad (2.2b)$$

where $\bar{\omega}_i = \epsilon_{ijl}\partial\bar{u}_l/\partial x_j$. We are free to choose the three independent components of the irrotational term in (2.2a) (in the sense that it is realistic to drive the flow with pressure gradients), but not the two wall-normal gradients $\partial\bar{u}/\partial y$ and $\partial\bar{w}/\partial y$ (which obey the vorticity transport equation). In the outer layer the correct vorticity history is induced by \mathcal{A}_{ij} , via inviscid skewing for example. However, because of the lack of y variation of the applied straining field, the inviscid-skewing mechanism and the other outer-layer strains will be active over the entire flow, all the way to the wall, where they are too weak to be relevant in practice. In order to also obtain the correct near-wall shear histories the walls are accelerated in the (x, z) -plane such that the difference between the mean streamwise and spanwise velocities at the channel centreline and the wall varies in time at the same rate that the outer-layer velocity in the spatial flow changes as it convects downstream.

The temporal/spatial analogy is completed by equating the free-stream (edge) velocity of the boundary layer with the difference between the mean centreline velocity of the channel (\bar{u}_c, \bar{w}_c) and the wall velocity (u_w, w_w) , and posing that that difference $\Delta\bar{\mathbf{u}}_c$ evolves as

$$\frac{\partial\Delta\bar{u}_c}{\partial t} = U_\infty \frac{\partial U_\infty}{\partial x} + W_\infty \frac{\partial U_\infty}{\partial z} = \Delta\bar{u}_c \mathcal{A}_{11} + \Delta\bar{w}_c \mathcal{A}_{13}, \quad (2.3a)$$

$$\frac{\partial\Delta\bar{w}_c}{\partial t} = U_\infty \frac{\partial W_\infty}{\partial x} + W_\infty \frac{\partial W_\infty}{\partial z} = \Delta\bar{u}_c \mathcal{A}_{31} + \Delta\bar{w}_c \mathcal{A}_{33}, \quad (2.3b)$$

where $\Delta \bar{\mathbf{u}}_c = (\Delta \bar{u}_c, \Delta \bar{w}_c)$, with $\Delta \bar{u}_c = \bar{u}_c - u_w$ and $\Delta \bar{w}_c = \bar{w}_c - w_w$. The histories of the two components of this velocity difference represent the final two (the inner or bulk acceleration/deceleration) independent perturbation parameters mentioned above. Their role is to ensure that $\mathbf{U}_{\text{avg}} - \mathbf{u}_w$ changes in time in the strained channel much as it does in the downstream direction in the spatially developing flow, so that the appropriate inner layer (i.e. near-wall shear) will result. Since the mean shear near the wall is typically much greater than \mathcal{A}_{ij} (whose magnitude is set by the outer-layer strain), the accelerating walls are able to duplicate gross mean-flow features of the near-wall region, such that realistic 3DWL velocity profiles are obtained over the entire channel (see figures 4 and 15 below).

The strategy outlined above allows us to systematically approximate spatial 3DBLs with a temporally evolving channel flow. Channel simulations are much more efficient than those of a spatial boundary layer, allowing a much more extensive study for a given cost. Advantages include being able to use fully developed two-dimensional channel flow as a single clearly defined initial condition, and thus to avoid the ambiguity of often-troublesome inflow and outflow conditions. Obtaining the Reynolds-stress tensor and budgets is easier from a programming point of view, and having two spatial averaging directions more than offsets the loss of homogeneity in time, when it comes to obtaining statistical samples. Spatial simulations require much larger streamwise domains, which are costly both in terms of memory and of time required to reach steady state (Spalart & Watmuff 1993; Spalart & Coleman 1997). Also, ensemble averaging can be applied over the two halves of the channel and further samples can be gathered by starting the distortion at different times of the two-dimensional simulation (Moin *et al.* 1990) or by applying it in the opposite direction. Another benefit is the generality: combinations of distortions and wall-velocity histories can be arranged to isolate pure straining effects, two-dimensional or three-dimensional, or to closely approximate deformations experienced by the near-wall and outer regions of a wide range of boundary layers. The generality of most spatial DNS studies is constrained by their homogeneity in the spanwise direction. A final advantage is that the simulation statistics depend only on time and the wall-normal coordinate y , which implies that an unsteady one-dimensional problem can be used to investigate 3DBL physics and to test and develop turbulence models for various spatially evolving flows. Reynolds-averaged solutions can be obtained rapidly from a personal computer.

2.2. Problem formulation

An incompressible flow with velocity \mathcal{V}_i ($i = 1, 2, 3$) and pressure \mathcal{P} is considered in an orthogonal reference frame $\mathbf{x} = (x_1, x_2, x_3) = (x, y, z)$. The approach is similar to that of Rogallo (1981) (see also Lee & Reynolds 1985), except that instead of distorting spatially homogeneous turbulence $\mathbf{u}'(\mathbf{x}, t)$, here the flow $\mathbf{u}(\mathbf{x}, t)$ is between two no-slip surfaces and will contain both fluctuations $\mathbf{u}'(\mathbf{x}, t)$ and an inhomogeneous mean $\bar{\mathbf{u}}(y, t)$. Rogers (2000) has also performed a homogeneous-strain/inhomogeneous-flow DNS study, for a free shear flow.

The numerical code uses coordinates $\mathbf{x}^* = (x_1^*, x_2^*, x_3^*) = (x^*, y^*, z^*)$ aligned with the principal axes of the deformation tensor \mathcal{A}_{ij} , so that

$$\mathcal{A}_{ij}^* \equiv \frac{\partial U_i^*}{\partial x_j^*} = \begin{bmatrix} \mathcal{A}_{11}^* & 0 & 0 \\ 0 & \mathcal{A}_{22}^* & 0 \\ 0 & 0 & \mathcal{A}_{33}^* \end{bmatrix}, \quad (2.4)$$

with $\mathcal{A}_{ii}^* = 0$. We have

$$x^* = x \cos \sigma - z \sin \sigma, \quad y^* = y, \quad z^* = z \cos \sigma + x \sin \sigma, \quad (2.5a)$$

where $\mathbf{x} = (x, y, z)$ are the 'downstream coordinates' (x is the initial streamwise direction of the two-dimensional channel flow), and equivalent relations for the velocity components. The angle σ is defined as positive when clockwise (i.e. from x toward z —see figure 3c). Because of its meaning over swept wings (which nominally impose a strain at a right angle to their leading edge; Bradshaw & Pontikos 1987), σ will be referred to as the angle of sweep. We have

$$\mathcal{A}_{11} = \mathcal{A}_{11}^* \cos^2 \sigma + \mathcal{A}_{33}^* \sin^2 \sigma, \quad (2.5b)$$

$$\mathcal{A}_{22} = \mathcal{A}_{22}^*, \quad (2.5c)$$

$$\mathcal{A}_{33} = \mathcal{A}_{11}^* \sin^2 \sigma + \mathcal{A}_{33}^* \cos^2 \sigma, \quad (2.5d)$$

$$\mathcal{A}_{13} = \mathcal{A}_{31} = -\mathcal{A}_{11}^* \cos \sigma \sin \sigma + \mathcal{A}_{33}^* \cos \sigma \sin \sigma. \quad (2.5e)$$

As mentioned above, there are three independent strain parameters: σ and any two of \mathcal{A}_{11}^* , \mathcal{A}_{22}^* and \mathcal{A}_{33}^* , with the third following from $\mathcal{A}_{ii}^* = 0$. With respect to the downstream axes, the independent parameters are \mathcal{A}_{13} and any two of \mathcal{A}_{11} , \mathcal{A}_{22} and \mathcal{A}_{33} .

The straining is imposed for $t \geq 0$ and the initial condition at $t = 0$ is fully developed turbulent plane channel flow. At $t = 0$ the flow becomes

$$\mathcal{V}_i(\mathbf{x}, t) = u_i(\mathbf{x}, t) + U_i(\mathbf{x}, t), \quad (2.6)$$

and the pressure \mathcal{P} changes from p to $p + \mathcal{Q}$. The imposed deformation field U_i varies linearly in space according to $U_i(\mathbf{x}, t) = \mathcal{A}_{ij}(t) x_j$, where the spatially uniform velocity gradient \mathcal{A}_{ij} is given by (2.1), and each component is a function solely of time.

The DNS domain is aligned with the principal axes of the superimposed strain, with the walls at $y^* = y = \pm \delta$. When $\sigma \neq 0$ a 'swept' initial condition is used; that is the initial two-dimensional flow direction is oriented at the angle σ with respect to the x^* -axis (cf. figure 3c below), by specifying that the z^* -component of the bulk mass flux be non-zero. (The initial conditions are obtained by running the strained-channel code with no strain, as a conventional Poiseuille DNS.) Each component of \mathbf{u}^* is required to satisfy the no-slip condition $\mathbf{u}^* = \mathbf{u}_w^*$ at $y = \pm \delta$, where $\mathbf{u}_w^* = (u_w^*, 0, w_w^*)$ is the velocity of the walls.

As a result of (2.6), the 'embedded' wall-bounded flow \mathbf{u}^* will be strained at the rate $\mathcal{S}_{ij}^* = \frac{1}{2}(\mathcal{A}_{ij}^* + \mathcal{A}_{ji}^*) = \mathcal{A}_{ij}^*$, and will satisfy

$$\frac{\partial u_i^*}{\partial t} + u_j^* \mathcal{A}_{ij}^* + u_j^* \frac{\partial u_i^*}{\partial x_j^*} = - \left. \frac{\partial \bar{p}}{\partial x_i^*} \right|_{\text{app}} - \frac{\partial p'}{\partial x_i^*} + \frac{1}{Re} \frac{\partial^2 u_i^*}{\partial x_j^* \partial x_j^*} - \mathcal{A}_{j\ell}^* x_\ell^* \frac{\partial u_i^*}{\partial x_j^*} \quad (2.7a)$$

and

$$\frac{\partial u_i^*}{\partial x_i^*} = 0. \quad (2.7b)$$

All variables in (2.7) are non-dimensionalized by the initial channel half-width $\delta(0)$ and a reference velocity U_{ref} (which here will be of the order of the initial friction velocity $u_\tau(0)$). The reference Reynolds number is $Re = U_{\text{ref}} \delta(0) / \nu$, where ν is the kinematic viscosity, and p is the non-dimensional kinematic pressure, which we have decomposed into its mean \bar{p} and fluctuating component p' . The quantity $\partial \bar{p} / \partial x_i^*|_{\text{app}}$ is the applied mean pressure gradient, a time-dependent, spatially uniform body force.

The momentum contribution for the imposed field was removed from (2.7a) because it is curl-free:

$$\left(\frac{\partial U_i^*}{\partial t} + U_{\ell}^* \mathcal{A}_{i\ell}^* \right) = \left(\frac{\partial \mathcal{B}_{ij}^*}{\partial t} + \mathcal{B}_{i\ell}^* \mathcal{A}_{\ell j}^* \right) x_j^* = -\frac{\partial \mathcal{Q}}{\partial x_i^*}, \quad (2.8)$$

and is attributed to a pressure field \mathcal{Q} , which is quadratic in space.

Following Rogallo (1981) we now introduce the coordinates

$$\xi_i = \mathcal{B}_{ij}(t) x_j^*, \quad \hat{t} = t, \quad (2.9a)$$

defined by the transformation \mathcal{B}_{ij} , subject to the constraint that the new spatial variables (ξ_1, ξ_2, ξ_3) be material properties of the imposed strain flow:

$$\frac{\partial \xi_i}{\partial t} + U_j \frac{\partial \xi_i}{\partial x_j^*} = \left(\frac{\partial \mathcal{B}_{ij}}{\partial t} + \mathcal{B}_{i\ell} \mathcal{A}_{\ell j}^* \right) x_j^* = 0,$$

or

$$\frac{\partial \mathcal{B}_{ij}}{\partial t} + \mathcal{B}_{i\ell} \mathcal{A}_{\ell j}^* = 0, \quad (2.9b)$$

and $\mathcal{B}_{ij}(0) = \delta_{ij}$. This choice for (2.9) removes the secular term (explicitly containing x_i^*) from (2.7a) and thus allows periodic conditions in planes parallel to the walls. The distance (measured in x_i^*) between lines of constant ξ_i indicates the total amount of deformation produced by \mathcal{A}_{ij}^* . Transforming (2.7) from (x_i^*, t) to (ξ_i, \hat{t}) coordinates, and using (2.9b), gives

$$\frac{\partial u_i^*}{\partial \hat{t}} + u_j^* \mathcal{A}_{ij}^* + u_j^* \mathcal{B}_{\ell j} \frac{\partial u_i^*}{\partial \xi_{\ell}} = -\frac{\partial \bar{p}}{\partial x_i^*} \Big|_{\text{app}} - \mathcal{B}_{\ell i} \frac{\partial p'}{\partial \xi_{\ell}} + \frac{1}{Re} \mathcal{B}_{\ell j} \mathcal{B}_{nj} \frac{\partial^2 u_i^*}{\partial \xi_{\ell} \partial \xi_n} \quad (2.10a)$$

and

$$\mathcal{B}_{ji} \frac{\partial u_i^*}{\partial \xi_j} = 0, \quad (2.10b)$$

which are subject to the boundary conditions $\mathbf{u}^* = \mathbf{u}_w^*$ at $\xi_2 = \pm 1$. The form of (2.10) is identical to that for simple Poiseuille flow, except for the time-dependent metric terms \mathcal{B}_{ij} multiplying each spatial derivative, and the \mathcal{A}_{ij}^* term on the left-hand side. It is, however, important to bear in mind the new significance of the unsteady term in (2.10a), which now indicates the temporal change at fixed $\xi_i(\mathbf{x}^*, t) = \mathcal{B}_{ij}(t) \xi_j(\mathbf{x}^*, 0)$ (rather than at fixed x_i^*). For modelling studies, the Reynolds-averaged equations can be deduced from (2.10a).

To solve (2.10) a closed-form expression for the coordinate-mapping function $\mathcal{B}_{ij}(t)$ is required. Limiting our attention to the special case of constant strain rate, for which $\partial \mathcal{A}_{ij}^* / \partial t = 0$, we have for the solution of (2.9b)

$$\mathcal{B}_{ij}(t) = \begin{bmatrix} \exp(-\mathcal{A}_{11}^* t) & 0 & 0 \\ 0 & \exp(-\mathcal{A}_{22}^* t) & 0 \\ 0 & 0 & \exp(-\mathcal{A}_{33}^* t) \end{bmatrix}. \quad (2.11)$$

Applying (2.11) to (2.9a) reveals the histories of the channel half-width,

$$\delta(t) = \delta(0) \exp(\mathcal{A}_{22}^* t), \quad (2.12a)$$

and of the horizontal domain sizes A_{x^*} and A_{z^*} in the x^* - and z^* -directions,

$$A_{x^*}(t) = A_{x^*}(0) \exp(\mathcal{A}_{11}^* t) \quad \text{and} \quad A_{z^*}(t) = A_{z^*}(0) \exp(\mathcal{A}_{33}^* t). \quad (2.12b,c)$$

Equation (2.12) shows how the DNS domain deforms when \mathcal{A}_{ij}^* is constant in t . (Recall that other straining histories are possible.)

We now consider the wall-velocity histories $u_w^*(t)$ needed to control the temporal evolution of the rotational mean-velocity gradients near the walls. As explained above, this is done by ensuring that the centreline-wall mean velocity difference $\Delta\bar{u}_c^*$ satisfies equation (2.3), which in principal-strain axes reduces to

$$\frac{\partial \Delta\bar{u}_c^*}{\partial t} = \Delta\bar{u}_c^* \mathcal{A}_{11}^*, \quad (2.13a)$$

$$\frac{\partial \Delta\bar{w}_c^*}{\partial t} = \Delta\bar{w}_c^* \mathcal{A}_{33}^*, \quad (2.13b)$$

with $\Delta\bar{u}_c^* = \bar{u}_c^* - u_w^*$ and $\Delta\bar{w}_c^* = \bar{w}_c^* - w_w^*$. The simplest way to enforce (2.13)–the approach used to generate the results presented below—is to monitor the mean centreline velocity and adjust u_w^* according to

$$u_w^*(t) = \bar{u}_c^*(t) - \bar{u}_c^*(0) \exp(\mathcal{A}_{11}^* t), \quad (2.14a)$$

$$w_w^*(t) = \bar{w}_c^*(t) - \bar{w}_c^*(0) \exp(\mathcal{A}_{33}^* t), \quad (2.14b)$$

where $\bar{u}_c^*(0)$ and $\bar{w}_c^*(0)$ are the initial mean centreline velocities, the values at the instant the strain is imposed. We notice that the wall velocities explicitly depend on \mathcal{A}_{ij} and t through the exponential terms in (2.14). (They are also affected by the influence of \mathcal{A}_{ij} on \bar{u}_c .) During the computation the centreline values from the previous timestep are used to prescribe the wall velocities needed to calculate the current step.

More-empirical approaches can also be taken to specify u_w^* and w_w^* . The one used for our earlier finite- \mathcal{A}_{13} DNS results (Coleman *et al.* 1996b, 1997) was based on closing the inner leg of the mean velocity hodograph. While this more *ad hoc* method successfully causes the mean spanwise velocity profile $\bar{w}(y)$ to develop in time as it should (see figure 2 of Coleman *et al.* 1997), control of the streamwise component \bar{u} is less satisfactory, especially when normal-strain components are applied, which prompted us to employ the simpler and more rigorous formulation (2.14) for the present simulations. As we shall see below, since it yields centreline-wall velocity histories in close agreement with both (2.13a) and (2.13b), equation (2.14) produces streamwise and spanwise velocities that both evolve as the spatial-temporal analogy requires.

To complete the problem formulation we describe the behaviour of the pressure gradients $\nabla^* \bar{p}|_{\text{app}} = (\partial \bar{p} / \partial x^*, 0, \partial \bar{p} / \partial z^*)_{\text{app}}$ that appear on the right-hand sides of (2.7a) and (2.10a). Before the \mathcal{A}_{ij}^* strain is applied, they balance the mean wall-shear stress in the average. They can be constant in time (allowing temporal fluctuations of centreline velocity and total mass flux), or dynamically adjusted to keep the mean centreline velocity constant (which would be most consistent with our approach during the strain), or dynamically adjusted to keep the total mass flux constant. We use the third procedure, since it causes the two-dimensional statistics to converge more rapidly (Kim, Moin & Moser 1987). In the limit of an infinitely large domain (for which fully converged statistics would result from a single plane average) the three approaches would give identical results. Because the governing equations are invariant under streamwise and spanwise accelerations, whether we use $\nabla^* \bar{p}|_{\text{app}}$ or u_w^* to control the velocity difference between the outer layer and the channel walls is irrelevant. Once the strain is applied, we specify $\Delta\bar{u}_c^*$ via (2.14), and set and maintain $\nabla^* \bar{p}|_{\text{app}}$ equal to zero.

Case	$\mathcal{A}_{13}\delta(0)/u_\tau(0)$	$\mathcal{A}_{11}\delta(0)/u_\tau(0)$	$\mathcal{A}_{22}\delta(0)/u_\tau(0)$	$\mathcal{A}_{33}\delta(0)/u_\tau(0)$
S45	0.735	0	0	0
AS45	0.735	-0.735	+1.47	-0.735

TABLE 1. Parameters for the two straining cases.

$A_{x^*}/\delta(0)$	$A_{z^*}/\delta(0)$	m_{x^*}	m_{y^*}	m_{z^*}	n_{x^*}	n_{y^*}	n_{z^*}
$8\pi/3$	$8\pi/3$	256	129	256	384	129	384

TABLE 2. Numerical parameters.

Solutions to (2.10) are obtained using a modified version of the spectral channel code of Kim *et al.* (1987). It expresses dependent variables as Fourier series in ξ_1 and ξ_3 , and via Chebychev polynomials in ξ_2 . No-slip conditions are enforced using the tau method (Lanczos 1956), and a mixed Crank–Nicolson/Runge–Kutta time-advance scheme is employed (Spalart, Moser & Rogers 1991). Further details of the solution procedure are given in the Appendix.

2.3. Cases

Two straining fields are considered here, defined by the components summarized in table 1. Both cases correspond to 3DBLs, in that the angle of sweep σ and therefore the skewing $\mathcal{A}_{13} = \mathcal{A}_{31}$ are non-zero. We choose $\sigma = 45^\circ$ and set \mathcal{A}_{13} to 0.735 $u_\tau(0)/\delta(0)$, the initial wall-friction-velocity to channel-half-width ratio. The rationale for these choices is given below. For now we note that the first case, denoted S45 ('S' to indicate non-zero skewing, '45' the angle of sweep), has no normal components, and thus supplies the effect of a mean crossflow with no streamwise pressure gradient (PG); the second strain, Case AS45, combines skewing with streamwise deceleration and wall-normal stretching to create the deformation imposed by an idealized 45° -swept wing (hence the notation AS45 – 'A' for adverse-pressure-gradient, 'S45' for $\sigma = 45^\circ$ skewing).

The numerical parameters used for both cases are listed in table 2, where A_{x^*} and A_{z^*} are the horizontal domain sizes in the principal-strain coordinates, and $(m_{x^*}, m_{y^*}, m_{z^*})$ and $(n_{x^*}, n_{y^*}, n_{z^*})$ are respectively the number of expansion coefficients and collocation (quadrature) points in the x^* -, y^* -, and z^* -directions. Even though the initial Reynolds number for these runs is the same as that used by Kim *et al.* (1987) for their two-dimensional study, $Re_\tau = u_\tau\delta/\nu \approx 180$, the three-dimensional nature of the present flows requires a larger computational expense (i.e. a square horizontal domain), due to the non-zero angle of sweep and the crossflow development. Aliasing (quadrature) errors are minimized by setting $n_{x^*} = 3m_{x^*}/2$ and $n_{z^*} = 3m_{z^*}/2$. (Total aliasing-error control is not possible, since assigning $n_{y^*} = 3m_{y^*}/2$ would compromise the no-slip boundary conditions.) Spectra and two-point correlations from Case AS45 at $\mathcal{A}_{13}t = 0.125$ are shown in figure 2, from locations near the wall and the centreline; Case S45 results are similar. The effect of the deformation, which for this case involves a compression in the x^* -direction, can be seen in the spectra by the shift of energy to higher wavenumbers, compared to the initial distribution. In the correlations the influence of $\mathcal{A}_{11}^* < 0$ is apparent from the reduction of the length of maximum streamwise separation (a measure of the largest structures that can be faithfully represented within the domain) from $0.5A_{x^*}^*(0)$ at $t = 0$ to about $0.39A_{x^*}^*$ at the time shown. Despite the strain-induced change of scale of the turbulence, the spectra and

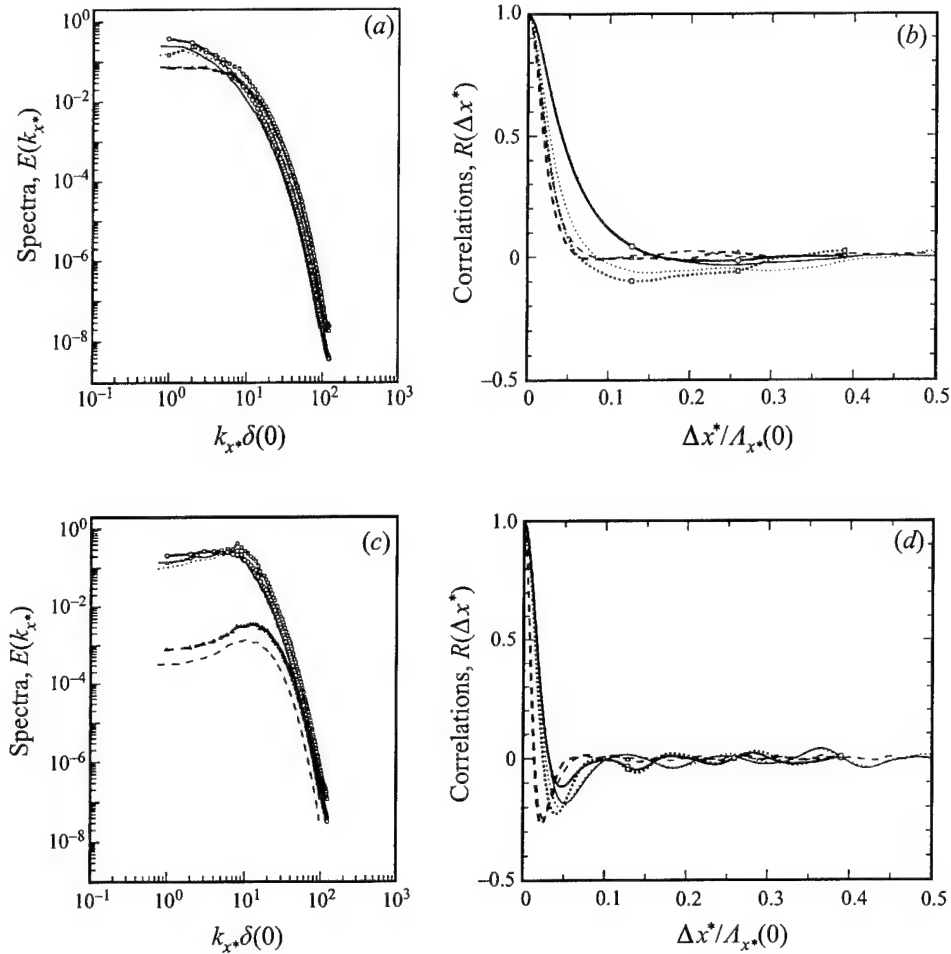


FIGURE 2. One-dimensional Fourier spectra and two-point correlations in principal-strain direction x^* for Case AS45: —, u^* component; - - -, v^* ; ·····, w^* . Curves with and without symbols respectively denote $A_{13}t = 0.125$ results and unstrained initial conditions at $A_{13}t = 0$. (a, b) near centreline, $y_w/\delta(0) = 0.805$; (c, d) near walls, $y_w/\delta(0) = 0.03$.

correlations reveal that the resolution and domain size are sufficient to capture both the smallest and largest spatial structures.

Multiple Case S45 and AS45 simulations were performed using the same strain parameters for statistically independent realizations of the two-dimensional Poiseuille initial conditions. These $\sigma = 45^\circ$ initial conditions were obtained by specifying that the bulk flow rates in x^* and z^* be equal and running the strained-channel code with no applied strain and the numerical parameters listed in table 2, until the statistics of the two-dimensional flow indicated a mature stationary state. At this point Case S45 and AS45 realizations were begun while the unstrained computation was continued until another statistically independent field for another pair of realizations was produced. The statistics presented below (denoted by an overbar) were gathered by averaging over planes parallel to the walls, over both halves of the channel, and over seven independent runs of each case.

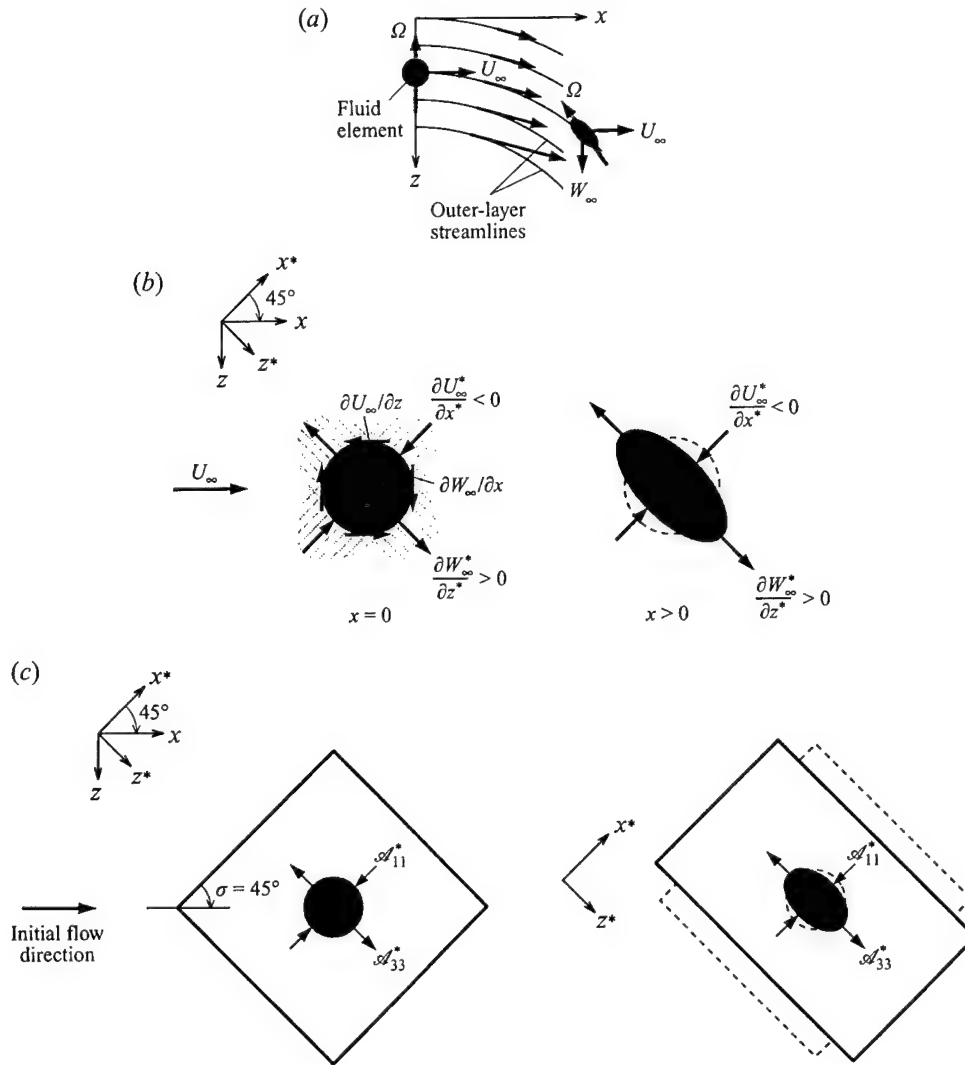


FIGURE 3. Plan view of three-dimensional wall layer subjected to pure-skewing strain. (a) Spatially developing flow. Outer-layer streamlines and isobars very nearly coincide. (b) Strain applied to fluid element of spatially developing flow and strained-channel DNS. (Cross-hatched regions represent angular distribution of normal strains.) (c) Initial and deformed domain of strained-channel DNS for Case S45.

3. Results

3.1. Pure-skewing strain: Case S45

In order to determine the influence of pure three-dimensionality unaccompanied by the complications of streamwise pressure gradients, we set $\mathcal{A}_{22}^* = 0$, $\mathcal{A}_{11}^* = -\mathcal{A}_{33}^* \neq 0$, and choose an angle of sweep $\sigma = 45^\circ$. With respect to the initial flow direction, the resulting strain field has only $\mathcal{A}_{13} = \mathcal{A}_{31}$ as non-zero components, so that it corresponds to an idealized mean pressure gradient that always acts at a right angle to the mean flow direction (figure 3). The channel turbulence thus experiences a deformation like that imposed along the centreline of Schwarz & Bradshaw's (1994)

curved wind tunnel. Unlike the curved-duct flow, for which the streamwise gradient $\partial P/\partial x$ can only be zero at one spanwise location, here the strain field is the same at every (x, z) point in the domain. (In the Schwarz & Bradshaw duct, along trajectories outside the centreline, the streamwise gradient through the bend is first adverse then favourable, and vice versa for paths closer to the centre of curvature; see their figure 2.) Another difference between the Schwarz & Bradshaw and present flows is in the magnitude of the skewing rate. The one used here, $\mathcal{A}_{13} = 0.735u_\tau(0)/\delta(0)$, is roughly twice as large, in terms of inflow u_τ and boundary-layer thickness, as the $\partial W/\partial x$ imposed in the curved-duct experiment. For these reasons (and also because of differences in Reynolds number, and downstream variation of the rate of skewing) we cannot expect the Schwarz & Bradshaw and Case S45 statistics to correspond. Nevertheless, the flows do share enough features that their comparative behaviour should be instructive.

3.1.1. Mean profiles and histories

The response of the mean velocity to the applied strain and in-plane wall motion (2.14) is illustrated in figure 4. These results validate the strained-channel methodology. A key characteristic of pressure-driven three-dimensional boundary layers can be seen, namely the sudden appearance of spanwise shear $\partial \bar{w}/\partial y$ (mean streamwise vorticity) in the outer layer, due to the \mathcal{A}_{13} -induced skewing of the mean spanwise vorticity. The straining of the flow structures, away from their natural shapes in the two-dimensional flow, is also reproduced (although the same mean-flow behaviour could be obtained simply by injecting streamwise vorticity with a y -dependent body force, such an injection is unrealistic; the straining is required to correctly deform the outer-layer structures). The absence of streamwise acceleration (i.e. $\mathcal{A}_{11} = \mathcal{A}_{22} = 0$) causes the 'thickness' of the flow to remain constant, such that the distance δ between the wall and centreline in figure 4(a) is the same at all times (cf. figure 15 below). The inviscid skewing mechanism is thus the only mean-straining effect present in the outer layer. As a consequence, the $\partial \bar{w}/\partial y$ variation above the location of maximum \bar{w} is inherited from the streamwise shear $\partial \bar{u}/\partial y$ of the initial flow. This explains the good agreement shown in figure 4(b) of the outer-layer hodograph with the straight solid lines, whose slopes are set by the Squire–Winter–Hawthorne (SWH) relationship, which assumes the mean velocity is governed solely by the effect of the skewing on the mean vorticity (Bradshaw 1987). For the present flow, using α to denote the angle through which the effective outer-layer mean velocity has turned due to the \mathcal{A}_{13} skewing, such that $\alpha = \arctan(\mathcal{A}_{13}t)$, the SWH prediction gives $u^\perp = u^\parallel \tan(2\alpha)$, where u^\perp and u^\parallel are respectively the velocity components orthogonal and parallel to the current effective flow direction of the applied irrotational mean. The requirement that the mean velocity vector (\bar{u}, \bar{w}) change direction across a 3DWL is manifested by the finite curvature of the hodograph, as it describes the velocity distribution across both inner and outer layers. If inviscid skewing were to control the crossflow over the entire layer, and there were no near-wall shear-driven effects, the hodograph would be completely straight, and everywhere (including the origin) have the negative slope given by the SWH angle 2α . The result would be a collateral, rather than three-dimensional, flow.

The inner-layer scaling of the mean-velocity magnitude is shown in figure 4(c) (the symbols are from Kim *et al.*'s 1987 simulation). Noticeable departures from the initial two-dimensional profile, and from the standard law of the wall, are found as a result of the skewing. The internal boundary layer associated with the rising magnitude of

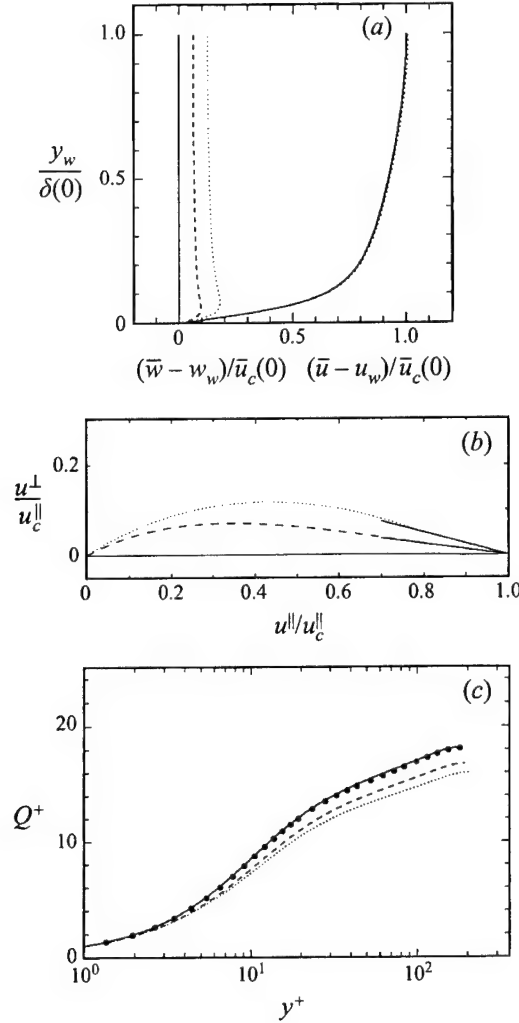


FIGURE 4. Mean velocity evolution for Case S45: —, $\mathcal{A}_{13}t = 0$ ($\alpha = 0^\circ$); - - -, $\mathcal{A}_{13}t = 0.0625$ ($\alpha = 3.6^\circ$); ·····, $\mathcal{A}_{13}t = 0.125$ ($\alpha = 7^\circ$). (a) Axes aligned with initial mean flow. (b) Hodograph, showing components (after wall velocities removed) parallel u^\parallel and normal u^\perp to instantaneous coordinates aligned with current direction of mean skewing (i.e. rotated away from principal-strain coordinates (x^*, z^*) by angle $\sigma + \alpha$), normalized by parallel component at centreline u_c^\parallel ; solid line segments denote SWH prediction. (c) Current wall-unit scaling; non-dimensional magnitude $Q^+ \equiv ((\bar{u} - u_w)^2 + (\bar{w} - u_w)^2)^{1/2} / u_\tau(t)$ and wall-normal coordinate $y^+ = y_w(0) \exp(\mathcal{A}_{22}t) u_\tau(t) / \nu$, where $u_\tau^2(t) = \nu[(\partial \bar{u} / \partial y)_w^2 + (\partial \bar{w} / \partial y)_w^2]^{1/2}$ is the current total wall-shear stress. Solid symbols are from two-dimensional $Re_\tau = 180$ channel of Kim *et al.* (1987).

the spanwise wall-shear stress has not propagated much higher than $y^+ \approx 10$ (cf. figures 4a and 4c).

The histories of the centreline-wall velocity differences $(\Delta \bar{u}_c, \Delta \bar{w}_c)$ responsible for the development of the inner layer are plotted in figure 5(a). The vertical lines in figure 5 indicate the times for which profiles are shown in other figures. These times, $\mathcal{A}_{13}t = 0, 0.0625$, and 0.125 , respectively correspond to skewing angles of $\alpha = 0^\circ, 3.6^\circ$, and 7° . The streamwise $\Delta \bar{u}_c$ and spanwise $\Delta \bar{w}_c$ components of the centreline-wall velocity difference are given by equation (2.14), which for the Case S45 strain field

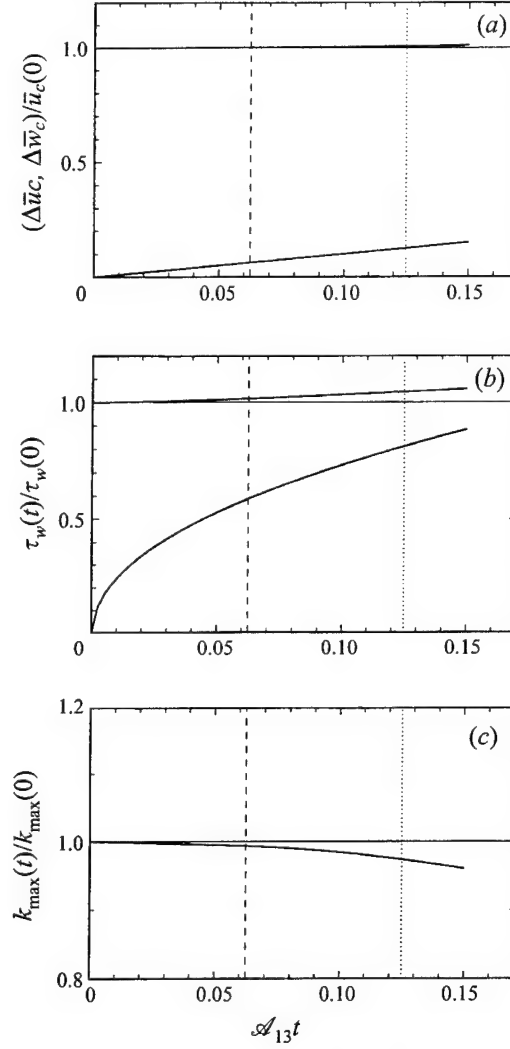


FIGURE 5. Histories of (a) mean centreline-wall velocity difference (equation (3.1)), (b) surface shear stress and (c) maximum turbulence kinetic energy for Case S45: upper curves, streamwise components ($\Delta \bar{u}_c = \bar{u}_c - u_w$ in (a), $(\tau_w)_x = \nu(\partial \bar{u}/\partial y)_w$ in (b)); lower curves, spanwise component ($\Delta \bar{w}_c = \bar{w}_c - w_w$ and $(\tau_w)_z = \nu(\partial \bar{w}/\partial y)_w$). Solid curve in (c) indicates maximum over all y_w locations of $k = \frac{1}{2}\bar{u}_i' u_i'$; (cf. figure 6b) (note expanded vertical scale). Vertical lines mark times for which mean profiles are shown in other figures.

are respectively

$$\frac{\bar{u}_c(t) - u_w(t)}{\bar{u}_c(0)} = \cosh(-\mathcal{A}_{13}t), \quad (3.1a)$$

$$\frac{\bar{w}_c(t) - w_w(t)}{\bar{u}_c(0)} = \sinh(-\mathcal{A}_{13}t). \quad (3.1b)$$

These dictate the evolution of the $y_w = \delta$ values of the figure 4(a) mean velocity profiles. The in-plane wall-velocity treatment (2.14) therefore closely approaches the desired nominally zero effective streamwise pressure gradient: (3.1a) yields $(\bar{u}_c -$

$u_w)/\bar{u}_c(0) = 1.006$ and 1.022 respectively at $\mathcal{A}_{13}t = 0.0625$ and 0.125 . The spanwise-component history (3.1b) produces nearly linear growth of the effective crossflow at the centreline for the times considered (figures 4a and 5a), and ensures that the hodograph is correctly closed at the surface (figure 4b). This in turn develops the appropriate mean shear near the wall. Another measure of the rotational mean-flow development is shown in figure 5(b), where the upper curve traces the history of the streamwise mean skin friction, and the lower curve reveals the growth of the spanwise component, which is rapid. In contrast to $\Delta\bar{u}_c$ and $\Delta\bar{w}_c$, which are functions only of $\mathcal{A}_{13}t$, the drag is affected by both the external forcing (applied strain) and the turbulence. In the Schwarz & Bradshaw experiment the total skin-friction coefficient C_f was observed to remain nearly constant through the bend, instead of increasing as in figure 5(b). However, since before entering the bend C_f was decaying with downstream distance, the levelling off in the curved section while the boundary-layer thickness kept increasing can perhaps be viewed as a milder form of the C_f increase seen here (furthermore, their perturbation was weaker).

The upward drift in time of the streamwise component of surface shear (figure 5b) might suggest that the turbulence near the wall has become more vigorous as the result of the applied skewing, but the histories of the turbulent stresses reveal the opposite. A stabilizing trend is apparent in figures 6(a) and 6(b), which respectively show a reduction with time of the profiles of streamwise Reynolds shear stress $-\bar{u}'v'$ and turbulence kinetic energy $k = \frac{1}{2}\bar{u}'u'_i = \frac{1}{2}q^2$. These reductions are more clearly quantified in the sub-plots in the upper-right corners of figures 6(a) and 6(b), which illustrate the amount the $\mathcal{A}_{13}t = 0.125$ profiles have changed from their initial values (the figure 6a inset shows the net change to $-\bar{u}'v'$; in figure 6(b) both k (solid symbols) and the vertical velocity variance $\bar{v}'v'$ (open symbols) are included). The decrease of k is also documented in figure 5(c), in terms of the history of k_{\max} , the largest value of k at each time. Figure 6(b) shows that as k decreases near the wall, the magnitude of the vertical velocity fluctuations $\bar{v}'v'$ becomes larger across the entire layer. The issue of the ultimate source of the near-wall reduction of k and inner- and outer-layer growth of $\bar{v}'v'$ will be addressed in the next subsection, where we consider the effect of the skewing on the various terms in the Reynolds-stress budgets. We shall find there that budget terms involving the pressure fluctuations play a crucial role in the evolution of the turbulence. Foreshadowing this discovery is the amplification of the pressure fluctuations themselves, whose root-mean-square values are found in figure 6(c).† Of particular significance is the instantaneous pressure-fluctuation increase caused by the impulsive application of the strain (compare the thin and thick solid curves,

† There is a subtlety associated with diagnosing the pressure field associated with the divergence-free velocity in the strained-channel flow: because the grid deforms in time, spatial and temporal derivatives do not commute, which introduces an extra term in the Poisson equation. The kinematic pressure p satisfies $p_{,ii} = -u_{j,i}^*u_{i,j}^* - 2u_{j,i}^*\mathcal{A}_{ij}^*$ (note the factor 2).

FIGURE 6. Profiles of (a) shear stress, (b) turbulence kinetic energy, and (c) root-mean-square pressure fluctuations for Case S45: —, $\mathcal{A}_{13}t = 0$ ($\alpha = 0^\circ$); - - -, $\mathcal{A}_{13}t = 0.0625$ ($\alpha = 3.6^\circ$); ·····, $\mathcal{A}_{13}t = 0.125$ ($\alpha = 7^\circ$) (data for $\mathcal{A}_{13}t = 0.0625$ not shown in (a) and (b) to clarify presentation). Lower, middle, and upper curves in (a) respectively correspond to spanwise Reynolds shear stress $-\bar{v}'w'$, streamwise Reynolds shear stress $-\bar{u}'v'$, and total shear stress $(\tau)_{\text{total}} = [(\nu(\partial\bar{u}/\partial y) - \bar{u}'v')^2 + (\nu(\partial\bar{w}/\partial y) - \bar{v}'w')^2]^{1/2}$. Subplots in (a) and (b) show change with respect to initial profile (in units of background plot) of $\mathcal{A}_{13}t = 0.125$ results, of (a) $-\bar{u}'v'$ and (b) k (solid symbols), $\bar{v}'v'$ (open symbols). Thick solid (—) curve in (c) is $\mathcal{A}_{13}t = 0$ value immediately after strain is applied (note expanded vertical scale).

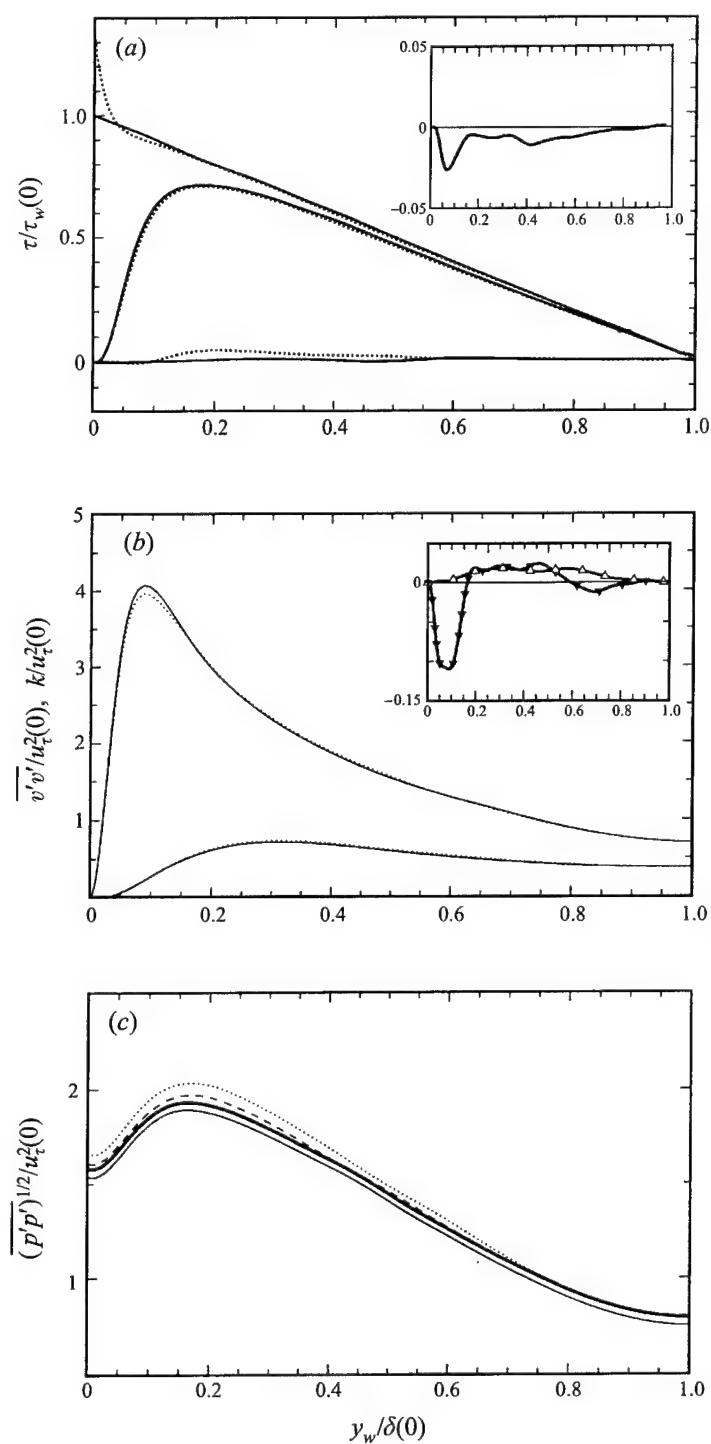


FIGURE 6. For caption see facing page.

which respectively illustrate the $\mathcal{A}_{13}t = 0$ profiles just before and just after the strain is applied). Because of the elliptic nature of an incompressible flow, the pressure-velocity correlations in the Reynolds-stress budgets exhibit step changes in time, and thus dominate the early flow history of the stresses. This will be demonstrated in §3.1.2.

While the trend is for k and $-\overline{u'v'}$ to both decrease, the $-\overline{v'w'}$ shear stress does the opposite, with the largest growth occurring near $y_w/\delta = 0.2$ (figure 6a). However, although this component grows, it does so at a rate too small to immediately offset the reduction in $-\overline{u'v'}$; the magnitude $\tau = (\overline{u'v'}^2 + \overline{v'w'}^2)^{1/2}$ of the Reynolds-shear stress 'vector' $(-\overline{u'v'}, -\overline{v'w'})$ also decreases in time. The decrease is very close to that observed for the total (turbulent plus viscous) shear stress magnitude $(\tau)_{\text{total}}$ (except immediately adjacent to the wall), shown in the upper curves in figure 6(a). The extent to which these pure-skewing-induced changes are the result of deep structural alterations to the Reynolds-stress tensor is revealed in figure 7(a). This plot presents the stress/energy ratio τ/q^2 (commonly given the symbol a_1 and referred to as the Reynolds-stress structure parameter), and shows it changes very little over most of the layer, with only a slight decrease of the maximum value. The implications of stress/energy-ratio reductions, a classical feature of perturbed 3DBLs, are twofold. From a fundamental point of view it implies that the extraction of kinetic energy from the mean by the turbulence has become less efficient. From a practical point of view it indicates an inaccuracy in turbulence models that assume a_1 is constant for all flows. The reduction seen in figure 7(a) is not large enough to pose a grave turbulence-modelling challenge; instead it demonstrates the degree to which the stress/energy ratio is (or rather is not) modified by a pure skewing strain. We shall see when we discuss Case AS45 that when the normal strain components are also non-zero the changes in a_1 are much larger.

Another indication of the effect of the mean skewing upon the turbulence structure is given by the ratio of the turbulent flux of turbulence kinetic energy to the turbulence kinetic energy itself, $\overline{v'(u'u' + v'v' + w'w')}/(\overline{u'u' + v'v' + w'w'})$. This ratio measures the velocity V_{q^2} with which $k = \frac{1}{2}q^2$ is transported by the turbulence either toward ($V_{q^2} < 0$) or away from ($V_{q^2} > 0$) the wall; it is plotted in figure 7(b). Unlike in the Schwarz & Bradshaw curved-duct experiment, where V_{q^2} was observed to decrease near the wall as the crossflow developed, and increase farther away, only minimal changes are produced by the Case S45 skewing. The source of this discrepancy is thought to be the off-centreline streamwise acceleration/deceleration, mentioned above, found in the duct flow (see also figure 18b below). The DNS results reveal that the impact of the pure skewing strain upon the turbulence structure is limited. Some aspects of modelling 3DWLs are therefore likely to be influenced less by mean three-dimensionality than by features unrelated to the introduction of mean crossflow.

An attribute of the pure-skewing flow that *will* expose many turbulence models—any that assume isotropic eddy viscosity—is the lack of agreement between the direction of the mean shear and Reynolds shear stress. Differences as large as 30° are observed, especially near the wall. This can be seen in figure 8. The sign change in the mean gradient angle $\gamma_g = \arctan[(\partial \bar{w}/\partial y)/(\partial \bar{u}/\partial y)]$ in figure 8(a) is a consequence of the sign change in $\partial \bar{w}/\partial y$ observed in figure 4(a). The modelling difficulty is in the finite time required for the spanwise shear to produce spanwise Reynolds stress $-\overline{v'w'}$. The slow growth of $-\overline{v'w'}$ is another classical feature of non-stationary 3DBLs (Schwarz & Bradshaw 1994). Because of it, the stress angle $\gamma'_t = \arctan[-\overline{v'w'}/-\overline{u'v'}]$ lags well behind γ_g . In fact, early on in the outer region the gradient and stress angles have opposite signs, and therefore rotate away from each other; it is only much later

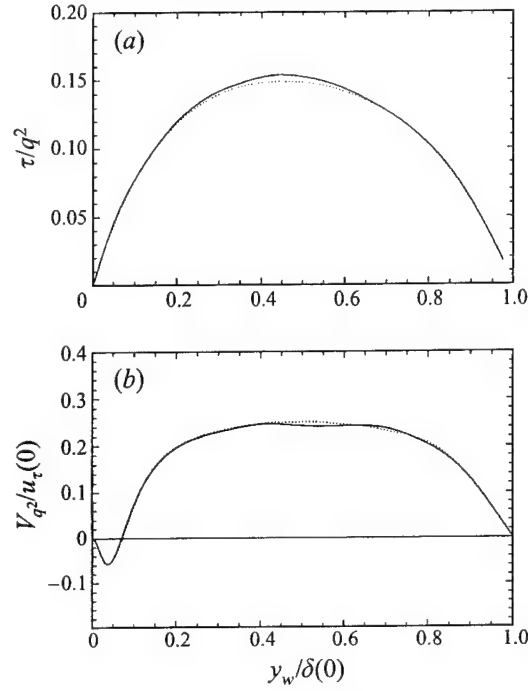


FIGURE 7. Profiles of (a) stress/energy ratio $a_1 = \tau/q^2$ and (b) turbulent transport velocity $V_{q^2} = \overline{v'u'_i u'_i}/q^2$ for Case S45: —, $\mathcal{A}_{13}t = 0$ ($\alpha = 0^\circ$); ·····, $\mathcal{A}_{13}t = 0.125$ ($\alpha = 7^\circ$) (data for $\mathcal{A}_{13}t = 0.0625$ not shown to clarify presentation). Reynolds-stress magnitude $\tau = (\overline{u'v'^2} + \overline{v'w'^2})^{1/2}$.

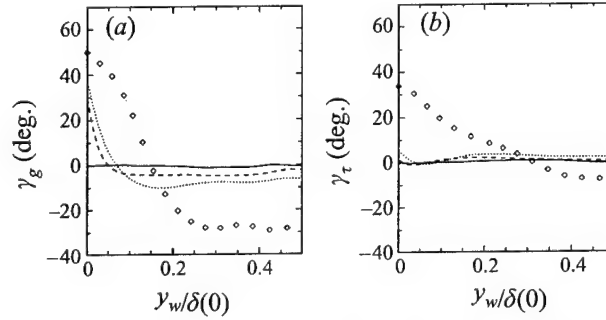


FIGURE 8. Direction of (a) mean shear γ_g and (b) Reynolds shear stress γ_τ for Case S45: —, $\mathcal{A}_{13}t = 0$ ($\alpha = 0^\circ$); - - -, $\mathcal{A}_{13}t = 0.0625$ ($\alpha = 3.6^\circ$); ·····, $\mathcal{A}_{13}t = 0.125$ ($\alpha = 7^\circ$); \diamond , $\mathcal{A}_{13}t = 0.60$ (single realization). Mean-shear angle $\gamma_g = \arctan[(\partial \bar{w}/\partial y)/(\partial \bar{u}/\partial y)]$; Reynolds-stress angle $\gamma_\tau = \arctan[-\overline{v'w'}/-\overline{u'v'}]$.

that γ_τ begins to follow (i.e. have the same sign but a smaller value than) γ_g in the outer region (compare the open symbols in figures 8(a) and 8(b), which show the variation of γ_g and γ_τ at $\mathcal{A}_{13}t = 0.60$). One of the primary goals of this project is to more fully understand the relationship between the mean shear ($\partial \bar{u}/\partial y, \partial \bar{w}/\partial y$) and the $(-\overline{u'v'}, -\overline{v'w'})$ stresses, and to ascertain the implications for modelling suddenly distorted 3DBLs. This will require consideration of the behaviour of the various terms in the Reynolds-stress budget equations, the subject to which we now turn.

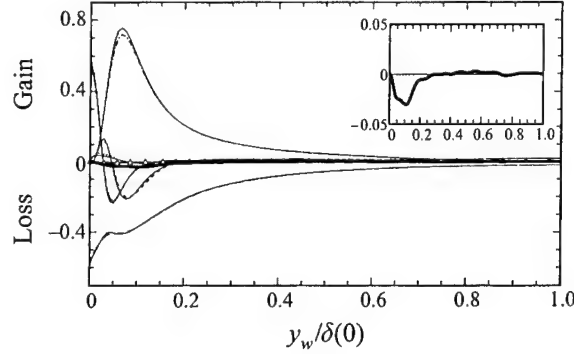


FIGURE 9. Terms in the budget of turbulence kinetic energy $k = 0.5\overline{u'_i u'_i}$ for Case S45: thin solid curves (—) denote terms at $\mathcal{A}_{13}t = 0$ (before strain); —·—, $P_k^s = \frac{1}{2}P_{ii}^s$ at $\mathcal{A}_{13}t = 0.125$; ———, $-\varepsilon_k = -\frac{1}{2}\varepsilon_{ii}$ at $\mathcal{A}_{13}t = 0.125$; - - -, $T_k = \frac{1}{2}T_{ii}$ at $\mathcal{A}_{13}t = 0.125$; —·—, $D_k = \frac{1}{2}D_{ii}$ at $\mathcal{A}_{13}t = 0.125$; ·····, $\Pi_k = \frac{1}{2}\Pi_{ii}$ at $\mathcal{A}_{13}t = 0.125$; \triangle , $P_k^{s'} = \frac{1}{2}P_{ii}^{s'}$ at $\mathcal{A}_{13}t = 0.125$; thick solid curve (—), sum of all terms ($\approx \partial k / \partial t$) at $\mathcal{A}_{13}t = 0.125$ (also shown in inset with expanded vertical scale). Shaded regions indicate change from unstrained initial-condition profiles. Curves normalized by U_{ref}^4/ν , where $U_{ref} = 0.73u_\tau(0)$.

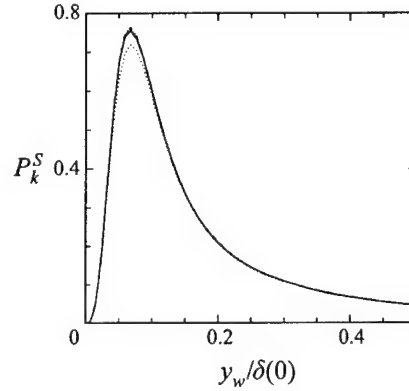


FIGURE 10. Mean-shear production $P_k^s = -\overline{u'v'} \partial \bar{u} / \partial y - \overline{v'w'} \partial \bar{w} / \partial y$ of turbulence kinetic energy for Case S45: —, P_k^s at $\mathcal{A}_{13}t = 0$; ·····, P_k^s at $\mathcal{A}_{13}t = 0.125$; —·—, product of $-\overline{u'v'}$ at $\mathcal{A}_{13}t = 0$ and $\partial \bar{u} / \partial y$ at $\mathcal{A}_{13}t = 0.125$. Normalization as in figure 9.

3.1.2. Reynolds-stress budgets

For the strained-channel flow, the non-dimensionalized transport equations for the Reynolds stresses reduce to

$$\frac{\partial \overline{u'_i u'_j}}{\partial \hat{t}} = P_{ij} + T_{ij} + D_{ij} + \Pi_{ij} - \varepsilon_{ij}, \quad (3.2)$$

where the effective material derivative $\partial / \partial \hat{t} = \partial / \partial t + \mathcal{A}_{22}y \partial / \partial y$ (see §2), and right-hand-side terms are the rates of (cf. Mansour, Kim & Moin 1988)

$$\text{production : } P_{ij} = -\overline{u'_i v'} \frac{\partial \bar{u}_j}{\partial y} - \overline{u'_j v'} \frac{\partial \bar{u}_i}{\partial y} - \overline{u'_i u'_\ell} \mathcal{A}_{j\ell} - \overline{u'_j u'_\ell} \mathcal{A}_{i\ell},$$

$$\text{dissipation : } -\varepsilon_{ij} = -\frac{2}{Re} \frac{\partial u'_i}{\partial x_\ell} \frac{\partial u'_j}{\partial x_\ell},$$

$$\text{turbulent transport : } T_{ij} = -\frac{\partial}{\partial y} \left(\overline{v' u_i' u_j'} \right),$$

$$\text{viscous diffusion : } D_{ij} = \frac{1}{Re} \frac{\partial^2}{\partial y^2} \left(\overline{u_i' u_j'} \right),$$

$$\text{velocity-pressure-gradient term : } \Pi_{ij} = - \left(\overline{u_i' \frac{\partial p'}{\partial x_j}} + \overline{u_j' \frac{\partial p'}{\partial x_i}} \right).$$

The Reynolds number Re is again based on the reference velocity U_{ref} and $\delta(0)$, the channel half-width of the unstrained initial condition. For Cases S45 and AS45, $Re = 130$ and U_{ref} is 0.73 times the initial friction velocity $u_\tau(0)$, such that $Re_\tau = u_\tau \delta / \nu = (u_\tau / U_{\text{ref}}) Re \exp(\mathcal{A}_{22} t)$ is initially ≈ 180 (as in Kim *et al.* 1987 and Mansour *et al.* 1988). The velocity u_i' and kinematic pressure p' in (3.2) have been scaled by U_{ref} , while the independent variable x_i is in units of $\delta(0)$. The Reynolds stresses $\overline{u_i' u_j'}$ are functions solely of time $t = \hat{t}$ and the wall-normal coordinate y , or equivalently the distance from the nearest wall, $y_w(t) = (1 - |y(0)|) \exp(\mathcal{A}_{22} t) = y_w(0) \exp(\mathcal{A}_{22} t)$.

Some modellers replace the velocity-pressure-gradient term in (3.2) by $\Pi_{ij} = \psi_{ij} + \phi_{ij}$, where (for this parallel flow) $\psi_{ij} = -(\partial \overline{p' u_i'} / \partial y) \delta_{2j} - (\partial \overline{p' u_j'} / \partial y) \delta_{2i}$ is the pressure-transport correlation (δ_{ij} is the Kronecker delta), and $\phi_{ij} = (\overline{p' (\partial u_i' / \partial x_j + \partial u_j' / \partial x_i)})$ is the pressure-strain term. We focus primarily upon the original velocity-pressure-gradient correlation Π_{ij} in this discussion.

On the other hand, a decomposition is applied to the production term, in order to distinguish between the direct effects of the irrotational applied strain \mathcal{A}_{ij} and those arising indirectly through changes to the rotational mean $\overline{\mathbf{u}}(y, t)$. We separate the total production rate P_{ij} into rotational (i.e. shear) and irrotational (applied-strain) components, $P_{ij} = P_{ij}^s + P_{ij}^{\mathcal{A}}$ respectively, where

$$P_{ij}^s = -\overline{u_i' v'} \frac{\partial \overline{u_j}}{\partial y} - \overline{u_j' v'} \frac{\partial \overline{u_i}}{\partial y}, \quad (3.3a)$$

$$P_{ij}^{\mathcal{A}} = -\overline{u_i' u_j'} \mathcal{A}_{j\ell} - \overline{u_j' u_i'} \mathcal{A}_{i\ell}. \quad (3.3b)$$

We begin by examining the budget of turbulence kinetic energy with the aim of determining the source of the reduction observed when the pure-skewing strain is applied (cf. figure 6b). The shaded regions in figure 9 indicate the amount each term changes during the time from $\mathcal{A}_{13} t = 0$ to 0.125, while the thick solid curve (both on the main plot and the expanded-scale inset) denotes the negative net $\partial k / \partial t$ given by the sum of all the right-hand-side terms† at $\mathcal{A}_{13} t = 0.125$. Also shown (the open symbols) is the ‘new’ applied-strain production $P_k^{\mathcal{A}} = -2\overline{u' w'} \mathcal{A}_{13}$; it is initially negligible (identically zero in the two-dimensional limit), and is still very small at $\mathcal{A}_{13} t = 0.125$, since by this time the applied strain has yet to produce an appreciable $-\overline{u' w'}$ stress. Although $P_k^{\mathcal{A}}$ contributes slightly to the kinetic energy decrease, the major source of the reduction is the change incurred by the mean-shear production $P_k^s = -\overline{u' v'} \partial \overline{u} / \partial y - \overline{v' w'} \partial \overline{w} / \partial y$. Most of the P_k^s decrease can in turn be traced to a reduction in the streamwise Reynolds shear stress $-\overline{u' v'}$, as figure 10 illustrates. The \mathcal{A}_{13} -induced decrease of the shear production is affected more by changes to the

† Strictly speaking, the right-hand-side sum is only approximately equal to $\partial k / \partial t$, since it includes any errors due to spatial discretization and incomplete statistical convergence. But for all budget data presented herein these factors are small enough that in the discussion to follow the approximation can be taken as an identity.

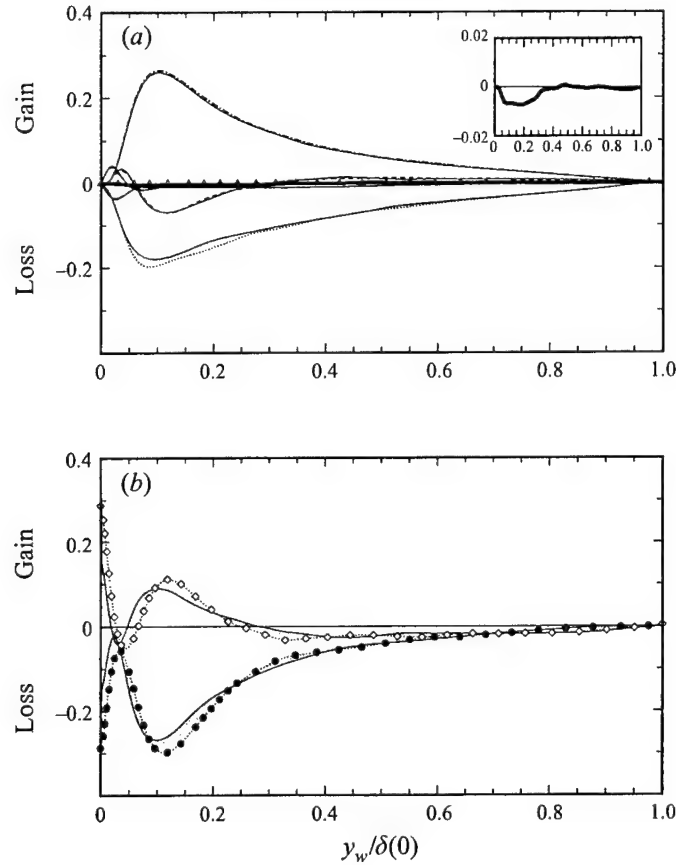


FIGURE 11. Terms in the budget of streamwise Reynolds shear stress $-\overline{u'v'}$ for Case S45: thin-solid curves (—) in (a) and (b) denote terms at $\mathcal{A}_{13}t = 0$ (before strain); — · —, $-P_{12}^s$ at $\mathcal{A}_{13}t = 0.125$; — — —, $+\varepsilon_{12}$ at $\mathcal{A}_{13}t = 0.125$; - - - -, $-T_{12}$ at $\mathcal{A}_{13}t = 0.125$; — · · —, $-D_{12}$ at $\mathcal{A}_{13}t = 0.125$; · · · · ·, $-\Pi_{12}$ at $\mathcal{A}_{13}t = 0.125$; Δ , $-P_{12}^s$ at $\mathcal{A}_{13}t = 0.125$; thick solid curve (—), sum of all terms ($\approx -\partial \overline{u'v'}/\partial t$) at $\mathcal{A}_{13}t = 0.125$ (also shown in inset with expanded vertical scale). Part (b) symbols: \bullet , pressure-strain correlation $-\phi_{12}$ at $\mathcal{A}_{13}t = 0.125$; \diamond , pressure-transport term $-\psi_{12}$ at $\mathcal{A}_{13}t = 0.125$. Shaded regions in (a) and (b) indicate change from unstrained initial-condition profiles. Normalization as in figure 9.

$-\overline{u'v'}$ Reynolds stress than to the $\partial \bar{u}/\partial y$ profile—since the initial P_k^s (the solid curve in figure 10) is nearly the same as the hypothetical production (the chain-double-dot curve) defined by the product of the mean shear $\partial \bar{u}/\partial y$ at $\mathcal{A}_{13}t = 0.125$ and the initial value of $-\overline{u'v'}$.

This result leads us to consider the $-\overline{u'v'}$ budget, whose terms are plotted in figure 11. The shaded regions again indicate the amount each term has changed with respect to its initial profile. Here the primary reason why $-\partial \overline{u'v'}/\partial t$ is negative (see the thick solid curve inset on the upper right-hand side of the figure) is the increase in amplitude of the velocity–pressure-gradient correlation Π_{12} (dotted curve). The rapid temporal variation of Π_{12} is accompanied by even larger changes to the pressure–strain ϕ_{12} and pressure–transport ψ_{12} terms, of which it is the sum (figure 11b). This implies that for this flow the velocity–pressure-gradient correlation, since it represents the imbalance of two larger terms, might be easier to model than each of ψ_{12} and ϕ_{12} .

The outer-layer increase in $-\overline{u'v'}$ production, $-P_{12}^s = \overline{v'v'} \partial \bar{u}/\partial y$, (barely) visible in

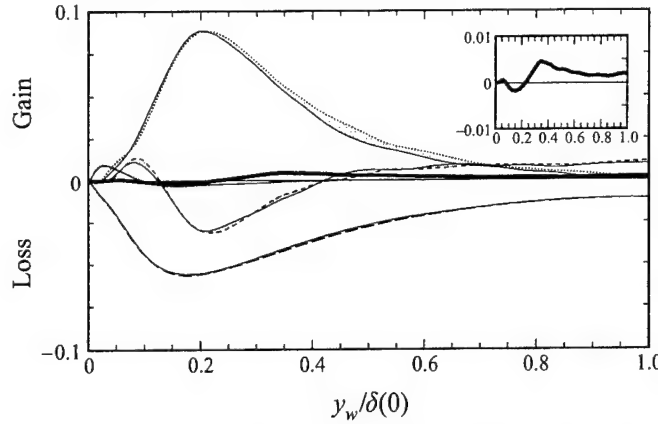
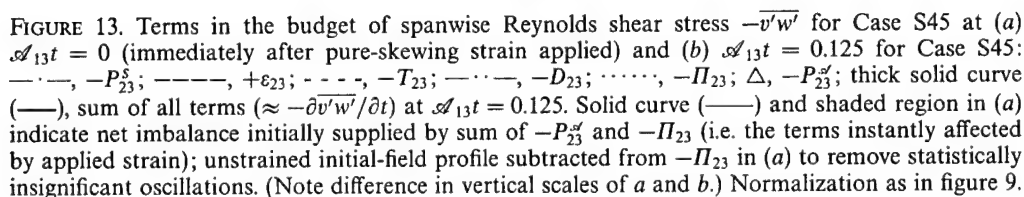


FIGURE 12. Terms in the budget of vertical-velocity variance $\overline{v'v'}$ for Case S45: thin solid curves (—) denote terms at $\mathcal{A}_{13}t = 0$ (before strain); — — —, $-\varepsilon_{22}$ at $\mathcal{A}_{13}t = 0.125$; - · - ·, T_{22} at $\mathcal{A}_{13}t = 0.125$; — · — ·, D_{22} at $\mathcal{A}_{13}t = 0.125$; · · · · ·, Π_{22} at $\mathcal{A}_{13}t = 0.125$; thick solid curve (—), sum of all terms ($\approx \partial \overline{v'v'}/\partial t$) at $\mathcal{A}_{13}t = 0.125$ (also shown in inset with expanded vertical scale). Shaded regions indicate change from unstrained initial-condition profiles. Normalization as in figure 9.

figure 11 is due in large part to amplification of Π_{22} , and the $\partial \overline{v'v'}/\partial t > 0$ it causes in this region (figure 12)—although changes to the dissipation ε_{22} and especially the turbulence transport T_{22} are not negligible. We conclude that the most apparent changes to the Reynolds-stress tensor crucially depend on the velocity–pressure-gradient correlation; the near-wall stabilization of the turbulence demonstrated in figure 5 can thus be attributed to the interaction of the pressure and velocity fluctuations overwhelming the influence of the extra-strain production introduced by the mean spanwise shear.

The Π_{ij} term also accounts for the slow growth of the spanwise Reynolds shear stress $-\overline{v'w'}$ (and its unexpected sign in the outer region, opposite to that of $\partial \overline{w}/\partial y$), and the resulting large difference documented in figure 8 between the direction of the mean gradient ($\partial \overline{u}/\partial y, \partial \overline{w}/\partial y$) and that of the shear stress ($-\overline{u'v'}, -\overline{v'w'}$). Evidence is presented in figure 13, which shows how the $-\overline{v'w'}$ budget is affected by the \mathcal{A}_{13} skewing. Two terms respond immediately to the impulsively applied strain: the applied-strain production $P_{23}^{\mathcal{A}}$ and the velocity–pressure-gradient correlation Π_{23} . The other terms in (3.2) react over finite time. These two quantities therefore alter the balance of the $-\overline{v'w'}$ transport equation the moment the strain is applied; they adjust from being either exactly zero ($P_{23}^{\mathcal{A}}$) or approximately so (Π_{23} , to the extent that the initial-condition statistics are converged and purely two-dimensional) to the initial \mathcal{A}_{13} -induced values illustrated in figure 13(a). The open-symbol curve denotes the new explicit production of $-\overline{v'w'}$, $-P_{23}^{\mathcal{A}} = \overline{u'v'}\mathcal{A}_{13}$, while the dotted curve shows the increase of $-\Pi_{23}$ due solely to the initial ‘turning on’ of the applied strain. (To clarify the presentation, the $-\Pi_{23}$ increase is measured with respect to its unstrained initial value, since the latter is not identically zero, and contains statistically insignificant but noticeable oscillations when viewed on the scale used for figure 13a.) The shaded region in figure 13(a) represents the sum of these two ‘initial pulse’ terms. We see that the initial (impulsive) effect of the strain is to create positive $-\overline{v'w'}$ everywhere except near the wall, where the trend is $-\partial \overline{v'w'}/\partial y < 0$. This tendency is exactly opposite to that associated with mean-shear production $-P_{23}^s$ (see the chain-dot curve in figure 13b) defined by the spanwise-shear profile (cf. figure 4a). This explains why initially



3.2. Swept-wing strain: Case AS45

Three-dimensionality rarely occurs in isolation, since pressure gradients that introduce a mean crossflow usually also accelerate or decelerate the boundary layer. Classic examples include flows upstream of wing-body junctions, over swept airfoils, and within the curved passages of turbomachinery—each of which in addition to being subject to a pure-skewing outer-layer deformation also experiences mean stretching or compression in the streamwise and wall-normal directions (van den Berg *et al.* 1975; Bradshaw & Pontikos 1985; Anderson & Eaton 1989; Ölçmen & Simpson 1995). In the past it has been difficult to differentiate between behaviour driven by the off-diagonal and the normal components of the irrotational deformation. The

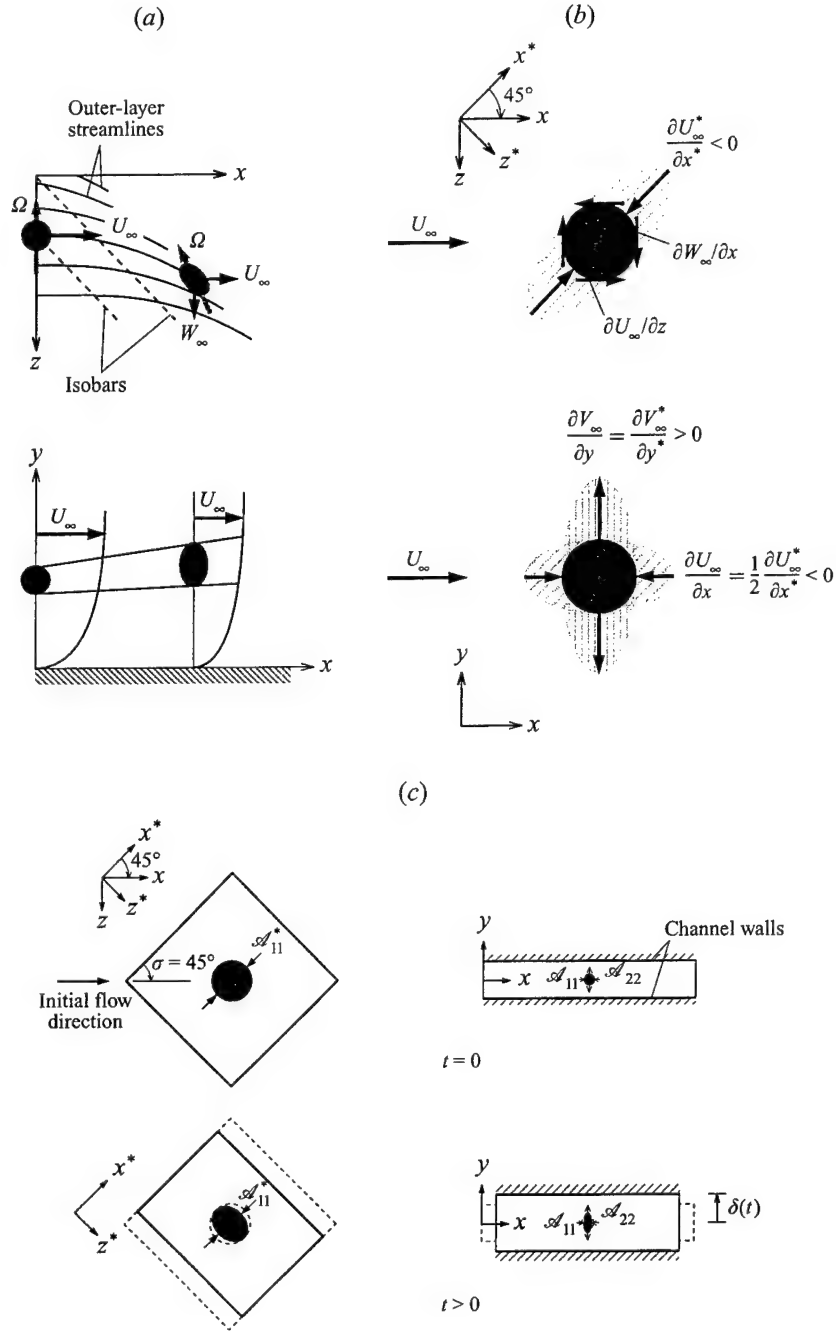


FIGURE 14. Plan and side views of three-dimensional boundary layer subjected to combined pure-skewing and APG strain. (a) Spatially developing flow: 45° infinite-swept wing ('port-side' version). (b) Strain applied to fluid element at $x = 0$ of spatially developing flow and at $t = 0$ of strained channel DNS. (Cross-hatched regions represent angular distribution of normal strains.) (c) Initial and deformed domain of strained-channel DNS for Case AS45.

DNS data presented in this section, from Case AS45, address this difficulty. By subjecting wall-bounded turbulence to the most general strain allowed by (2.1)–and thereby combining the effects of spanwise and streamwise mean pressure gradients–and comparing the results to those from the pure-skewing simulation, we expect to obtain significant insight into the physics of non-stationary 3DBLs.

We choose strain-field parameters that correspond to a time-developing counterpart of the infinite-swept-wing experiments of van den Berg *et al.* (1975) and Bradshaw & Pontikos (1985). Consequently, the principal-strain components are defined as $\mathcal{A}_{11}^* = -\mathcal{A}_{22}^* = -1.47u_\tau(0)/\delta(0)$ and $\mathcal{A}_{33}^* = 0$. Rather than the 35° angle of sweep used in the experiments, for Case AS45 σ is set to 45° . As a result, we apply the spanwise skewing, streamwise and spanwise deceleration, and wall-normal stretching appropriate for a 45° swept-wing: $\mathcal{A}_{13} = -\mathcal{A}_{11} = -\mathcal{A}_{33} = 0.5\mathcal{A}_{22}^* > 0$ (see table 1 and figure 14). The strain rate for this case is about an order of magnitude larger than that imposed in the van den Berg *et al.* and Bradshaw & Pontikos experiments (measured in terms of the friction velocity and boundary-layer thickness at the inlet of their curved diffuser), where here $\mathcal{A}_{13} = 0.735$ of the initial u_τ/δ . Note that the magnitude of skewing \mathcal{A}_{13} is the same for Case AS45 as it was for Case S45. (While the computational expense required to consider the experimental strain rate for the same range of $A_{13}t$ would have been unrealistically high, the early stages of one realization from a simulation with strain rate approximately equal to the van den Berg *et al.* and Bradshaw & Pontikos values will also be briefly discussed.) The ratio of mean-distortion to turbulence timescales will thus be significantly different in the strained-channel and experimental flows. Because of these factors, we only anticipate qualitative agreement.

3.2.1. Mean profiles and histories

The development of the Case AS45 mean crossflow is compared to that for the non-APG strain in figures 15(a) and 15(b). (Contrast the curves without and with symbols.) The total strain for the last time shown, $\mathcal{A}_{13}t = 0.125$, is similar to the equivalent total strain ($\mathcal{A}_{13}t \approx 0.15$) imposed in the Bradshaw & Pontikos experiment. While both DNS flows experience mean spanwise shear $\partial \bar{w}/\partial y$ in the outer layer as a result of the skewing, the distorting effect of the APG is also apparent for Case AS45, in the increase with time of the distance between the channel walls, which duplicates the thickening of the layer caused by the mean streamwise deceleration. In other words, $\partial \bar{w}/\partial y$ is distributed over a wider and wider region as time passes. The agreement with the SWH prediction (the solid lines in figure 15b) is not diminished by the presence of the APG strain. The streamwise deceleration $\mathcal{A}_{11} < 0$ is responsible for the leftward shift of the hodograph as the difference between the mean streamwise velocities of the flow and the wall is driven toward zero, under the influence of the in-plane wall motion prescribed by equation (2.14). For Case AS45, the streamwise and spanwise components of the centreline–wall velocity differences invoked by (2.14) are

$$\frac{\bar{u}_c(t) - u_w(t)}{\bar{u}_c(0)} = \frac{1}{2}(1 + \exp(-2\mathcal{A}_{13}t)), \quad (3.4a)$$

$$\frac{\bar{w}_c(t) - w_w(t)}{\bar{u}_c(0)} = \frac{1}{2}(1 - \exp(-2\mathcal{A}_{13}t)). \quad (3.4b)$$

As indicated in figure 16(a) (a graphical presentation of (3.4)), the wall motion thus combines a bulk streamwise deceleration (upper solid curve) with a growing crossflow

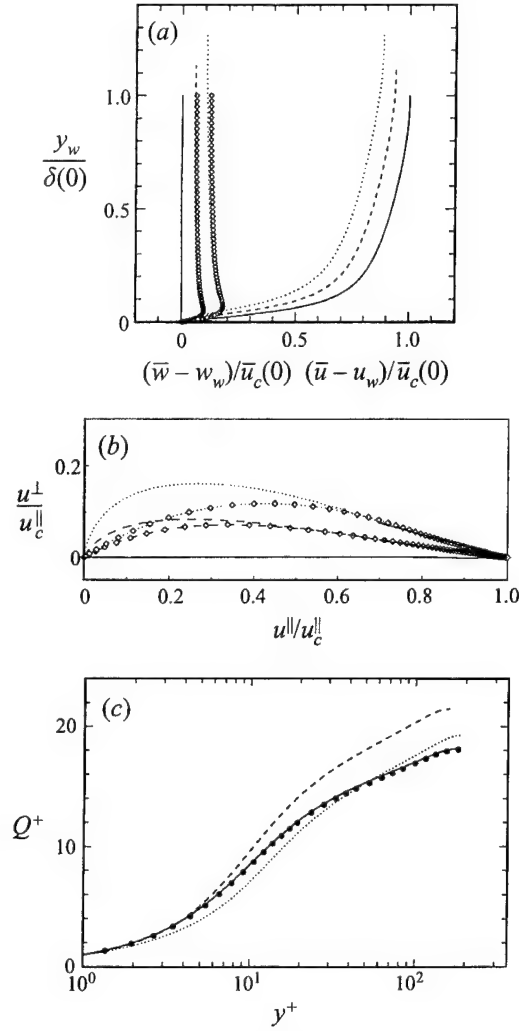


FIGURE 15. Mean velocity evolution for Case AS45 (coordinates and normalization as in figure 4): —, $\mathcal{A}_{13}t = 0$ ($\alpha = 0^\circ$) (and SWH prediction in *b*); - - -, $\mathcal{A}_{13}t = 0.0625$ ($\alpha = 3.6^\circ$); ·····, $\mathcal{A}_{13}t = 0.125$ ($\alpha = 7^\circ$); ●, two-dimensional $Re_\tau = 180$ channel of Kim *et al.* (1987). Open symbols in (a) and (b) are $\mathcal{A}_{13}t = 0.0625$ and 0.125 results from Case S45.

(lower solid curve). The strategy of coupling the in-plane wall motion and outer-layer strain described in §2 produces the desired mean flow behaviour.

The effect of the mean deceleration can be seen in the local minima in the total-shear-stress profile plotted in figure 17(a), and even more directly in the streamwise skin-friction history given by the upper thin solid curve in figure 16(b). As one would expect for a flow with negative \mathcal{A}_{11} , the surface shear exhibits a rapid decrease of the streamwise component. (The open symbols in figure 16 again represent the Case S45 results.) At $\mathcal{A}_{13}t = 0.125$, the latest time for which flow statistics are examined, the streamwise skin friction has fallen to 7.5% of its initial value, before becoming zero near $\mathcal{A}_{13}t = 0.15$ (and entering a ‘pseudo-separation’ regime, in the sense that the skin-friction reversal is not accompanied by strong flow away from the wall as it is in the spatial case). Despite undergoing such a large reduction, the mean streamwise

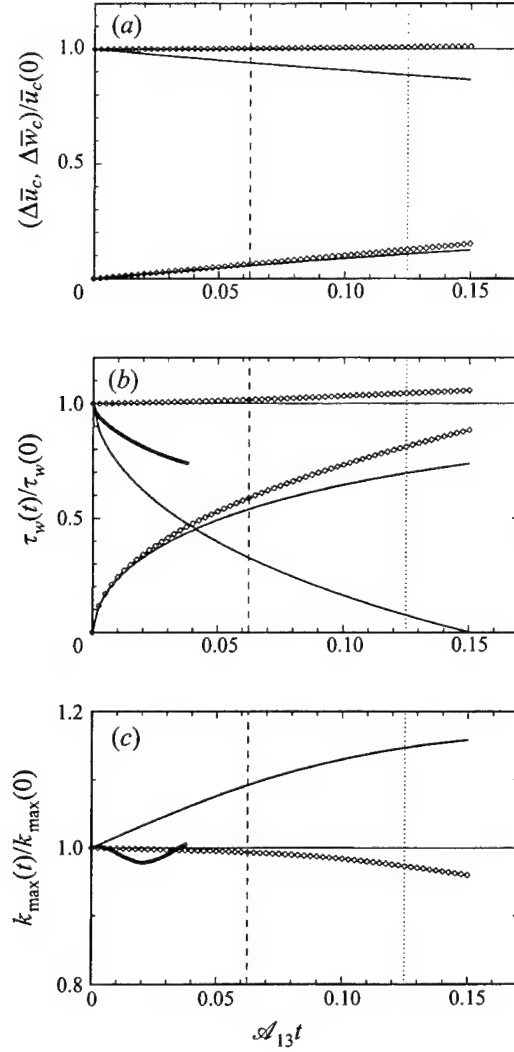


FIGURE 16. Histories of (a) mean centreline-wall velocity difference (equation (3.4)), (b) surface shear stress and (c) maximum turbulence kinetic energy for Case AS45: upper curves, streamwise components ($\Delta \bar{u}_c = \bar{u}_c - u_w$ in (a), $(\tau_w)_x = \nu(\partial \bar{u}/\partial y)_w$ in (b)); lower curves, spanwise component ($\Delta \bar{w}_c = \bar{w}_c - w_w$ and $(\tau_w)_z = \nu(\partial \bar{w}/\partial y)_w$). Thin solid curve in (c) indicates maximum over all y_w locations of $k = \frac{1}{2} \overline{u_i' u_i'}$ (cf. figure 17b); thick solid curves in (b) and (c) are from a single realization with $\mathcal{A}_{13} = -\mathcal{A}_{11} = -\mathcal{A}_{33} = 0.5\mathcal{A}_{22} = 0.12u_\tau(0)/\delta(0)$ (i.e. each component 16% of that used for Case AS45) (note expanded vertical scale in c). Vertical lines mark times for which mean profiles are shown in other figures. Open symbols are from Case S45.

shear at the wall $(\partial \bar{u}/\partial y)_w$ at $\mathcal{A}_{13}t = 0.125$ remains 18 times the size of the applied skewing strain \mathcal{A}_{13} . This suggests that in the near-wall region any unphysical effects due to the strain-induced deformation of the no-slip walls are less important at $\mathcal{A}_{13}t = 0.125$ than are features associated with the streamwise and spanwise shear.

By the time $(\partial \bar{u}/\partial y)_w$ changes sign at $\mathcal{A}_{13} \approx 0.15$, the mean flow has decelerated to the point where $(\bar{u}_c - \bar{u}_c(0))/\bar{u}_c(0) \approx 0.85$, and the effective pressure coefficient, $(C_p)_{\text{eff}} \equiv 1 - (\bar{u}_c/\bar{u}_c(t))^2$ is less than 0.3. Separation usually occurs when $(C_p)_{\text{eff}}$ is between 0.45 and 0.50 (e.g. Alving & Fernholz 1995; Spalart & Coleman 1997). The

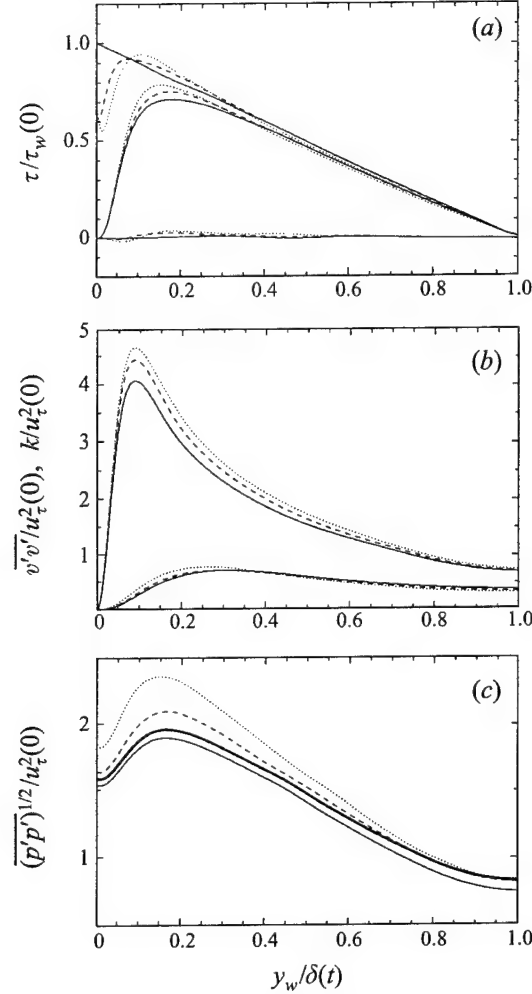


FIGURE 17. Profiles of (a) shear stress, (b) turbulence kinetic energy, and (c) root-mean-square pressure fluctuations for Case AS45: —, $\mathcal{A}_{13}t = 0$ ($\alpha = 0^\circ$); - - -, $\mathcal{A}_{13}t = 0.0625$ ($\alpha = 3.6^\circ$); ·····, $\mathcal{A}_{13}t = 0.125$ ($\alpha = 7^\circ$). Lower, middle, and upper curves in (a) respectively correspond to spanwise Reynolds shear stress $-v'w'$, streamwise Reynolds shear stress $-u'v'$, and total shear stress $(\tau)_{\text{total}} = [(v(\partial \bar{u}/\partial y) - u'v')^2 + (v(\partial \bar{w}/\partial y) - v'w')^2]^{1/2}$. Thick solid (—) curve in (c) is $\mathcal{A}_{13}t = 0$ value immediately after strain is applied (note expanded vertical scale).

lower-than-usual $(C_p)_{\text{eff}}$ at separation may be influenced by the step-function strain history. It is more strongly affected by the magnitude of the applied strain: when another infinite-swept-wing strain is used, one with \mathcal{A}_{13} ($= |\mathcal{A}_{11}| = \frac{1}{2} \mathcal{A}_{22} = |\mathcal{A}_{33}|$) approximately the same fraction of $u_\tau(0)/\delta(0)$ as in the van den Berg *et al.* and Bradshaw & Pontikos experiments (such that each component is 16% of its Case AS45 value), the streamwise wall-shear history shown by the thick-solid curve in figure 16(b) results. Although it has been stopped before the streamwise wall shear τ_w becomes negative, this run shows that the time at which it will do so is well past the $\mathcal{A}_{13}t = 0.15$ (and therefore significantly greater than the $(C_p)_{\text{eff}} \approx 0.3$) found for Case AS45. The separation point is not fixed solely by the magnitude of the pressure coefficient.

Whereas the effect of the swept-wing strain field is stabilizing near the wall (in the sense that it diminishes $\partial \bar{u}/\partial y$ and therefore the production), farther away the

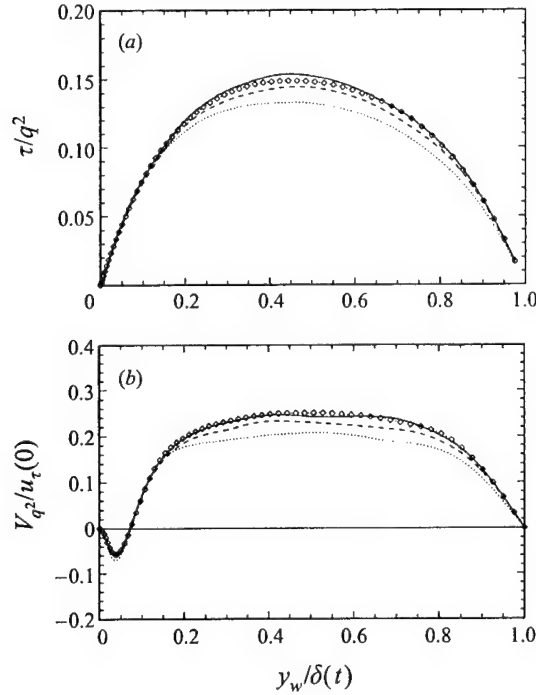


FIGURE 18. Profiles of (a) stress/energy ratio $a_1 = \tau/q^2$ and (b) turbulent transport velocity $V_q = \overline{v'u'_i u'_i}/q^2$ for Case AS45: —, $\mathcal{A}_{13}t = 0$ ($\alpha = 0^\circ$); - - -, $\mathcal{A}_{13}t = 0.0625$ ($\alpha = 3.6^\circ$); ·····, $\mathcal{A}_{13}t = 0.125$ ($\alpha = 7^\circ$). Open symbols in (a) and (b) are $\mathcal{A}_{13}t = 0.125$ results from Case S45.

opposite is true. Figure 16(c) shows that the maximum turbulence kinetic energy k_{\max} increases monotonically in time, with non-zero initial slope. This positive $\partial k_{\max}/\partial t$ at $t = 0$ is another symptom of the relatively large Case AS45 strain rate; for the run with \mathcal{A}_{13} chosen to approximate the experiments, the peak k initially decreases (cf. the thick solid curve in figure 16(c) with figure 7(g) of Bradshaw & Pontikos 1985). The Case AS45 strain is responsible for an increase in turbulence activity not just at the location of largest k , but across the entire channel: the kinetic-energy profiles in figure 17(b) show that k increases at every y_w . (Using the time-dependent channel half-width $\delta(t)$ to non-dimensionalize the wall-normal coordinate in figure 17(b) has made the outward shift of the location of maximum turbulence kinetic energy, typical of APG layers, less obvious; replacing $\delta(t)$ with the constant initial value $\delta(0)$ produces the expected behaviour, at least its initial stage; cf. figure 15a.) The wall-normal fluctuations $\overline{v'v'}$, on the other hand, increase their peak value while becoming less intense near the centreline (figure 17b). The pressure disturbances, like k , also uniformly increase for $0 \leq y_w \leq \delta(t)$ (figure 17c), to levels significantly larger than those found for Case S45. The impulsive change to the initial pressure field observed just after the strain is applied is also more pronounced for the swept-wing strain (compare the thick solid curves in figures 17c and 6c). In spite of the near-wall reduction in $\partial \bar{u}/\partial y$ revealed in figure 16(b), the streamwise Reynolds stress $-\overline{u'v'}$ experiences rapid growth for $y_w \leq 0.3\delta(t)$, where $-\partial \overline{u'v'}/\partial t > 0$. At larger distances from the wall $-\overline{u'v'}$ decreases slightly over time. An explanation for the behaviour of the k , $\overline{v'v'}$, and $-\overline{u'v'}$ statistics (and of the spanwise stress $-\overline{v'w'}$) presented in figure 17 is deferred until the next subsection, where we examine the Reynolds-stress budgets.

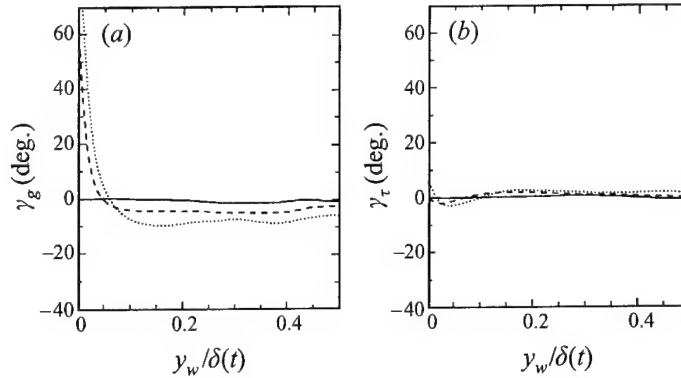


FIGURE 19. Direction of (a) mean shear γ_g and (b) Reynolds shear stress γ_τ for Case AS45: —, $\mathcal{A}_{13}t = 0$ ($\alpha = 0^\circ$); - - -, $\mathcal{A}_{13}t = 0.0625$ ($\alpha = 3.6^\circ$); ·····, $\mathcal{A}_{13}t = 0.125$ ($\alpha = 7^\circ$).

One can obtain insight into the relative significance of the various strain components by comparing the evolution of the stress/energy ratio a_1 and the turbulent transport velocity V_{q^2} for Case AS45 with those for Case S45. Both quantities are reduced in the outer layer to well below their initial levels by the swept-wing strain; a_1 and V_{q^2} reductions of the same magnitude were also found in the outer layer of the Bradshaw & Pontikos flow. Figure 18 also shows that the deformation containing normal-strain components (i.e. the one corresponding to an adverse streamwise pressure gradient) produces a much greater decrease than when the mean skewing acts alone (the open symbols in figure 18 represent pure-skewing results at $\mathcal{A}_{13}t = 0.125$, which corresponds to the dotted-profile Case AS45 data.) This implies that the strain created by an adverse pressure gradient has a greater influence on the development of the turbulence in a three-dimensional boundary layer than the spanwise shear does. Because of its wide-ranging practical consequences (e.g. with regard to turbulence-model development), we consider this finding to be one of the most significant results of this study.

It would be a mistake, however, to assume that all 3DBL features are controlled by the APG strains: another noteworthy characteristic of the swept-wing strain flow is illustrated in figure 19, concerning the early evolution of the spanwise Reynolds shear stress $-\overline{v'w'}$. The closely similar behaviour of the mean-gradient and shear-stress angles, γ_g and γ_τ , observed for Cases S45 and AS45 (cf. figures 8 and 19) points to the lack of dependence of $-\partial \overline{v'w'}/\partial t$ on the mean normal-strain components. In other words, the misalignment between $(\partial \overline{u}/\partial y, \partial \overline{w}/\partial y)$ and $(-\overline{u'v'}, -\overline{v'w'})$ is not affected by the mean deformation induced by the APG. The quantities that are responsible, and their insensitivity to the streamwise pressure gradient, are topics of the next subsection.

3.2.2. Reynolds-stress budgets

As in §3.1.2, we begin with the turbulence kinetic energy k . The profiles in figure 20 reveal the origin of the increase observed in figure 17(b). Whereas the initial impact of the pure-skewing strain was negligible (cf. figure 9), for the swept-wing case the applied-strain production $P_k^{\mathcal{A}}$ (open symbols in figure 20a) instantly provides a substantial source of energy to the turbulence. (The thick solid curve in figure 20(a) represents the sum of $P_k^{\mathcal{A}}$ and the initial impulsive change to Π_k (the shaded region) caused by the immediate alteration of the pressure field produced by the applied strain;

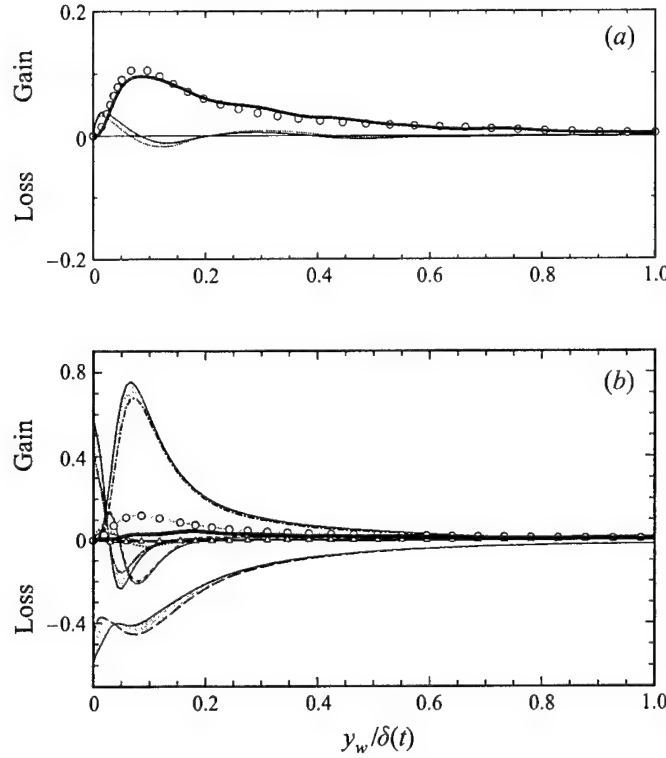


FIGURE 20. Terms in the budget of turbulence kinetic energy $k = 0.5\overline{u'_i u'_i}$ at (a) $\mathcal{A}_{13}t = 0$ and (b) $\mathcal{A}_{13}t = 0.125$ for Case AS45. Quantities in (a) are those instantly affected by applied strain: —, $\Pi_k = \frac{1}{2}\Pi_{ii}$ for unstrained initial field; ·····, Π_k just after strain applied; ○, $-\overline{u'u'}\mathcal{A}_{11} - \overline{v'v'}\mathcal{A}_{22} - \overline{w'w'}\mathcal{A}_{33}$ (i.e. non-zero terms of applied-strain production $P_k^s = \frac{1}{2}P_{ii}^s$) at $\mathcal{A}_{13}t = 0$; —, sum of all terms ($\approx \partial k/\partial t$) immediately after strain applied. Quantities in (b) reveal changes after finite time: thin solid curves (—) denote terms at $\mathcal{A}_{13}t = 0$ (before strain); —, P_k^s at $\mathcal{A}_{13}t = 0.125$; —, $-\varepsilon_k$ at $\mathcal{A}_{13}t = 0.125$; ---, T_k at $\mathcal{A}_{13}t = 0.125$; -·-·-, D_k at $\mathcal{A}_{13}t = 0.125$; ·····, Π_k at $\mathcal{A}_{13}t = 0.125$; △, $-2\overline{u'w'}\mathcal{A}_{13}$ at $\mathcal{A}_{13}t = 0.125$; ○, $-\overline{u'u'}\mathcal{A}_{11} - \overline{v'v'}\mathcal{A}_{22} - \overline{w'w'}\mathcal{A}_{33}$ at $\mathcal{A}_{13}t = 0.125$; thick solid curve (—), sum of all terms ($\approx \partial k/\partial t$) at $\mathcal{A}_{13}t = 0.125$. Shaded regions indicate change from unstrained initial-condition profiles. Normalization as in figure 9. (Note difference in vertical scales of a and b.)

the Π_k change is much smaller than the initial P_k^s .) The turbulence becomes more energetic for Case AS45 than for Case S45 because of the normal-strain components in the swept-wing field; since $P_k^s = -2\overline{u'w'}\mathcal{A}_{13} - \overline{u'u'}\mathcal{A}_{11} - \overline{v'v'}\mathcal{A}_{22} - \overline{w'w'}\mathcal{A}_{33}$ (and the normal Reynolds stresses of the two-dimensional initial field are non-zero), the irrotational strain creates and maintains a production term that is of the order of 15–20% of the initial shear production P_k^s . The open circles in figure 20 denote the fraction of P_k^s defined by the streamwise \mathcal{A}_{11} , wall-normal \mathcal{A}_{22} , and spanwise \mathcal{A}_{33} components while the open triangles correspond to that due to \mathcal{A}_{13} . (This convention will also be used for the other Reynolds stresses, with circles and triangles used to distinguish between applied-strain production P_{ij}^s associated with the normal and off-diagonal components, respectively.) The Case AS45 strain has a distinct implicit or indirect effect on the budget for k , since it leads to pronounced changes of all the terms present in the unstrained field (see the shaded regions in figure 20b). For example, the large structural alteration illustrated above by the turbulent transport velocity V_{q^2} (figure 18b) appears in figure 20 as the difference between the initial and $\mathcal{A}_{13}t = 0.125$ (short-

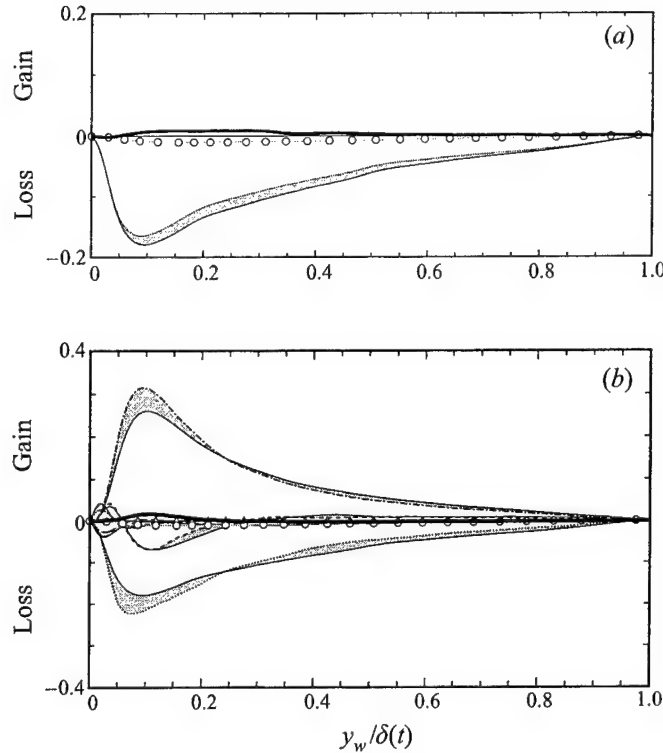


FIGURE 21. Terms in the budget of streamwise Reynolds shear stress $-\overline{u'v'}$ at (a) $\mathcal{A}_{13}t = 0$ and (b) $\mathcal{A}_{13}t = 0.125$ for Case AS45. Quantities in (a) are those instantly affected by applied strain: —, $-\Pi_{12}$ for unstrained initial field; ·····, $-\Pi_{12}$ just after strain applied; ○, $u'v'(\mathcal{A}_{11} + \mathcal{A}_{22})$ (i.e. non-zero terms of applied-strain production $-P_{12}^{\mathcal{A}}$) at $\mathcal{A}_{13}t = 0$; —, sum of all terms ($\approx -\partial\overline{u'v'}/\partial t$) immediately after strain applied. Quantities in (b) reveal changes after finite time: thin solid curves (—) denote terms at $\mathcal{A}_{13}t = 0$ (before strain); —·—, $-P_{12}^s$ at $\mathcal{A}_{13}t = 0.125$; ———, $+\varepsilon_{12}$ at $\mathcal{A}_{13}t = 0.125$; - - -, $-T_{12}$ at $\mathcal{A}_{13}t = 0.125$; —·—, $-D_{12}$ at $\mathcal{A}_{13}t = 0.125$; ·····, $-\Pi_{12}$ at $\mathcal{A}_{13}t = 0.125$; △, $v'w'\mathcal{A}_{13}$ at $\mathcal{A}_{13}t = 0.125$; ○, $u'v'(\mathcal{A}_{11} + \mathcal{A}_{22})$ at $\mathcal{A}_{13}t = 0.125$; thick solid curve (—), sum of all terms ($\approx -\partial\overline{u'v'}/\partial t$) at $\mathcal{A}_{13}t = 0.125$. Shaded regions indicate change from unstrained initial-condition profiles. Normalization as in figure 9. (Note difference in vertical scales of a and b.)

dashed) turbulent transport curves T_k ; changes to the shear production, dissipation, viscous diffusion, and velocity–pressure-gradient terms are even larger. Nevertheless, the explicit contribution of $P_k^{\mathcal{A}}$ is larger still. It leads to positive $\partial k/\partial t$ at every y_w location, and thus accounts for the uniform increase of the k profiles found in figure 17(b), and the rising history in figure 16(c). In the sense of being able to directly supply energy to the turbulence, the APG-induced strains (diagonal components) therefore have a more profound influence on the flow than the \mathcal{A}_{13} skewing does.

The explanation is less straightforward for the $-\overline{u'v'}$ budget, whose terms are shown in figure 21. Instead of being mostly the result of the applied-strain production, the sign of the initial $-\partial\overline{u'v'}/\partial t$ pulse (the thick solid curve in figure 21a) is now determined by an immediate increase of $-\Pi_{12}$ (the shaded region) due to the initial step change of the pressure field as it responds to the application of the strain. The figure 21(b) results indicate that the same tendency, for $-\partial\overline{u'v'}/\partial t$ and $-P_{12}^{\mathcal{A}}$ to be of opposite sign, is also found after finite time ($\mathcal{A}_{13}t = 0.125$). The indirect effect of the strain is thus more important in the development of $-\overline{u'v'}$ than are either of

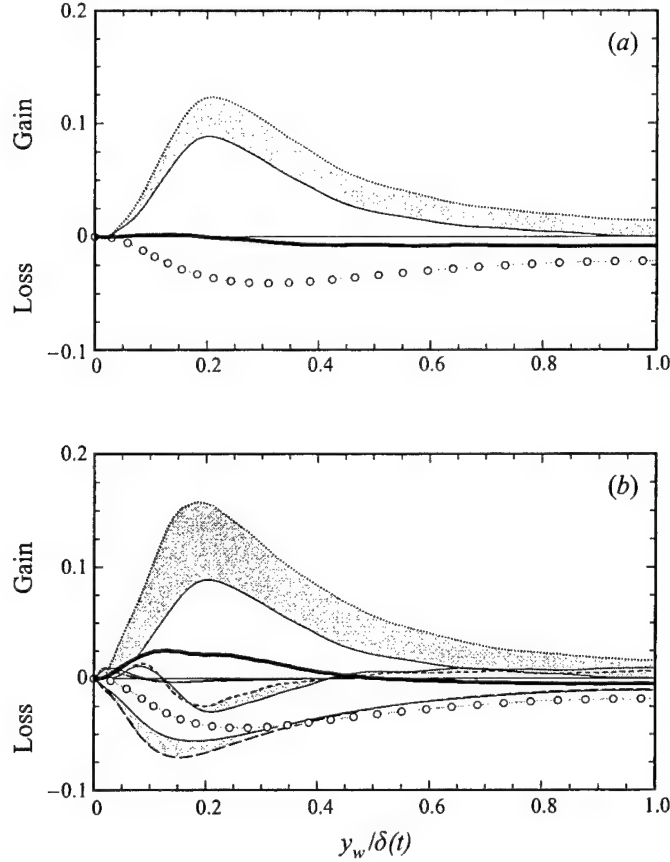
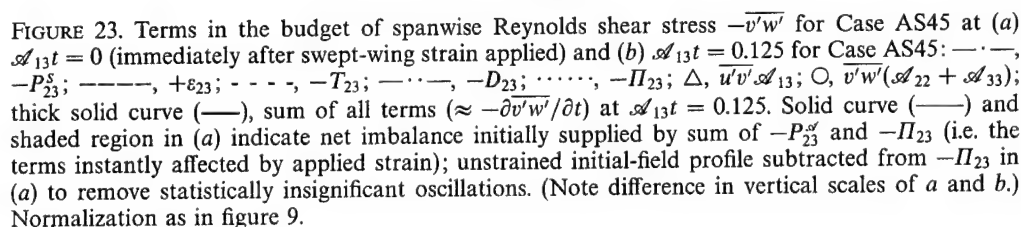


FIGURE 22. Terms in the budget of vertical-velocity variance $\overline{v'v'}$ at (a) $\mathcal{A}_{13}t = 0$ and (b) $\mathcal{A}_{13}t = 0.125$ for Case AS45: Quantities in (a) are those instantly affected by applied strain: —, velocity–pressure-gradient correlation Π_{22} for unstrained initial field; ·····, Π_{22} just after strain applied; ○, $P_{22}^s = -2\overline{v'v'}\mathcal{A}_{22}$ at $\mathcal{A}_{13}t = 0$; —, sum of all terms ($\approx \partial\overline{v'v'}/\partial t$) immediately after strain applied. Quantities in (b) reveal changes after finite time: thin solid curves (—) denote terms at $\mathcal{A}_{13}t = 0$ (before strain); ———, $-\varepsilon_{22}$ at $\mathcal{A}_{13}t = 0.125$; - - -, T_{22} at $\mathcal{A}_{13}t = 0.125$; —·—·—, D_{22} at $\mathcal{A}_{13}t = 0.125$; ·····, Π_{22} at $\mathcal{A}_{13}t = 0.125$; ○, P_{22}^s at $\mathcal{A}_{13}t = 0.125$; thick solid curve (—), sum of all terms ($\approx \partial\overline{v'v'}/\partial t$) at $\mathcal{A}_{13}t = 0.125$. Shaded regions indicate change from unstrained initial-condition profiles. Normalization as in figure 9.

the normal or off-diagonal contributions to the applied-strain production $-P_{12}^s$. The positive $-\partial\overline{u'v'}/\partial t$ found at $\mathcal{A}_{13}t = 0.125$ is primarily due to the imbalance between two large changes: an increase in the shear production $-P_{12}^s$, and a decrease in the velocity–pressure-gradient correlation $-\Pi_{12}$, with the former slightly larger than the latter. (Note that in the outer layer, both the initial-impulse and $\mathcal{A}_{13}t = 0.125$ values of $-\Pi_{12}$ represent a source of $-\overline{u'v'}$, while below $y_w = 0.3\delta(t)$ this term also begins as a source but eventually acts to reduce the $-\overline{u'v'}$ stress.) The amplification of the shear production $-P_{12}^s = \overline{v'v'}\partial\overline{u}/\partial y$ is itself a symptom of a significant change to Π_{22} , another of the velocity–pressure-gradient components. The growth of $-P_{12}^s$ is caused by growth of the vertical-velocity variance $\overline{v'v'}$. (Recall that figure 16 indicates a $\partial\overline{u}/\partial y$ decrease in the immediate vicinity of the wall.) Figure 22 shows that the $\overline{v'v'}$ increase is primarily the result of strain-induced alterations to Π_{22} . Once again the initial impulsive change to the velocity–pressure-gradient correlation acts to instantly



offset the applied-strain production, with the Π_{22} increase roughly balancing the negative P_{22}' first applied to the flow (figure 22a); at later times, Π_{22} overwhelms the explicit production, causing the net positive $\partial \bar{v}'v'/\partial t$ observed in figure 22(b), which in turn leads to the $-\bar{u}'v'$ and k growth evident in the above statistics. This behaviour is absent from Case S45. Neither the explicit $\bar{v}'v'$ production $P_{22}' = -2\bar{v}'v'\mathcal{A}_{22}$ (which here represents a sink, since $\mathcal{A}_{22} > 0$) nor the Π_{22} ‘kickback’ is present when the skewing deformation acts alone (cf. figure 12). An APG is needed to thicken the layer (or a favourable one needed to thin it) for this Π_{22} -versus- P_{22}' imbalance to occur.

Our last result concerns the $-\overline{v'w'}$ budget, presented in figure 23. It reveals yet another 'tug-of-war' (partial cancellation) between the implicit effects embodied by the velocity-pressure-gradient term ($-\Pi_{23}$) and explicit new production supplied by mean flow gradients, in this case by both the spanwise shear ($\overline{v'v'} \partial \bar{w}/\partial y$) and the applied strain ($\overline{u'v'} \mathcal{A}_{13} + \overline{v'w'} [\mathcal{A}_{22} + \mathcal{A}_{33}]$). Immediately after the strain is applied, the impact of the swept-wing deformation is nearly identical to that of the pure-skewing strain. This is because $-\overline{v'w'}$ is zero for a two-dimensional flow,[†] so that $-P_{23}^{\mathcal{A}}$ is initially the

† The extent to which this infinite-ensemble-average idealization is realized by the initial fields is revealed by the solid curves in figures 8(b) and 19(b).

same for the two cases, and because the normal-strain components have a negligible effect on the initial $-\Pi_{23}$ jump created by the impulsive distortion. The latter can be inferred by comparing the dotted curves in figures 13(a) and 23(a), which respectively indicate the impulsive initial changes of $-\Pi_{23}$ for Cases S45 and AS45; they are indistinguishable. The budgets are also qualitatively similar even after the turbulence has been subjected to the two strain fields for a finite time, with the $-P_{23}^s$ and $-P_{23}^{\omega}$ production, the $-\Pi_{23}$ correlation, and net $-\partial \overline{v'w'}/\partial t$ each in approximately the same proportion, regardless of whether or not the normal-strain components are active (cf. figures 13b and 23b). In the light of this similarity, it is no surprise that the shear-stress angle γ_τ profiles in figures 8(b) and 19(b) agree so well. Once again we notice that the magnitude of the net $-\partial \overline{v'w'}/\partial t$ is given by the difference of much larger terms.

The $-\overline{v'w'}$ budgets for Cases AS45 and S45 have at least two significant implications. The first is simply that this component of shear stress is primarily affected by the \mathcal{A}_{13} skewing (either directly or indirectly) and the mean spanwise shear that the skewing generates; in 3DBLs of practical interest, $-\overline{v'w'}$ (and the lag between the mean-shear and shear-stress angles γ_g and γ_τ) is therefore likely to be relatively insensitive to the normal-strain components introduced by adverse pressure gradients. A second, broader, implication of the budget analysis is the need to capture the effect of each of the velocity-pressure-gradient terms in turbulence models used to predict the development of suddenly distorted three-dimensional boundary layers.

4. Summary and concluding remarks

Time-developing strained-channel flow has been simulated as an idealization of pressure-driven three-dimensional turbulent boundary layers. DNS results are used to investigate questions regarding the physics and modelling of three-dimensional wall layers that arise from sudden mean-flow perturbations. This approach has the advantage of capturing the essential features of perturbed 3DBLs with a turbulent flow whose statistics depend only on time and one spatial dimension. Several of the difficult-to-model characteristics found in the spatial case are observed and quantified. These include the lag between the mean shear and Reynolds shear stress, the modification of the relationship between the components of the Reynolds stress tensor, and the controlling influence of the pressure-velocity correlation terms in the Reynolds-stress budgets.

Two strain fields were considered, with and without the effect of streamwise deceleration, but both including the same mean skewing components. The flow histories reveal that the impact of the APG on the outer-layer structure of the turbulence is more profound than that of the mean three-dimensionality. The stress/energy ratio a_1 experiences a much larger decrease when the APG strain is present. Although the strain rate used here is larger than that imposed in 3DBL experiments in which the stress/energy ratio decrease was attributed to mean crossflow (e.g. van den Berg *et al.* 1975; Bradshaw & Pontikos 1985; Schwarz & Bradshaw 1994), the dominance of the APG over the skewing deformation appears to be a fairly general result. Gleyzes *et al.* (1993) found that the same conclusion holds in the boundary layer over a finite swept wing, while Webster *et al.* (1996) have more recently discovered that the APG overwhelms the influence of the skewing in their experimental study of the three-dimensional boundary layer over a swept bump. While significant structural changes effected solely by spanwise shear are well-documented for purely shear-driven 3DBLs (e.g. Driver & Hebbbar 1987; Moin *et al.* 1990; Jung *et al.* 1992; Le *et al.* 1999), it appears that $\partial \overline{w}/\partial y$ -induced changes in the outer layer are modest.

Nearer to the wall the story is different. Here the effect of the spanwise shear is crucial, for both the shear- and pressure-driven cases. This can be inferred for example by the common near-wall kinetic energy reduction observed in the shear-driven three-dimensional channel flows (Moin *et al.* 1990; Coleman *et al.* 1996a; and Le *et al.* 1999), the strained channel (Case S45 and the low-strain-rate version of Case AS45) discussed above, and the infinite-swept-wing experiment of Bradshaw & Pontikos (1985). It is significant that the pure-skewing Case S45 results demonstrate the stabilizing behaviour associated with conversion of a two-dimensional stationary boundary layer to a non-stationary one by addition of shear-generated mean three-dimensionality. The similarity of the near-wall dynamics of shear- and pressure-driven 3DBLs becomes even more apparent when the Reynolds-stress budgets for the pure-skewing and spanwise-moving-wall channel flows are compared (see figures 3 and 4 of Le *et al.* 1999).

In addition to producing the above general conclusions, the DNS results can be used in a quantitative manner to test and develop specific Reynolds-averaged closures. Data files containing the drag histories, mean and variance profiles, and Reynolds-stress budgets presented here are available from the authors for this purpose. To aid in this endeavour, the channel-flow solver of Wilcox (1998) has been modified to accommodate the strained-channel geometry and will be supplied upon request (Fortran and C versions are available). In addition to this code, which should be useful to modellers interested in testing their schemes against the DNS statistics, benchmark data have also been prepared by applying the strains to the laminar channel flow; these will allow rapid validation of the moving-wall boundary conditions and straining terms needed for the conversion of conventional- to strained-channel solvers.

This work was sponsored by the Office of Naval Research (Grant No. N00014-94-1-0016), Dr L. P. Purtell program officer. It was done in collaboration with Dr A.-T. Le. Computer resources have been supplied by the NAS program at NASA-Ames Research Center, the San Diego Supercomputer Center NPACI program, and the DOD Major Shared Resource Center. The C version of the strained-channel model-test program was converted from Fortran by Mr Khaled Nefti. At various stages of this study we have benefited from insightful comments and suggestions made by Professor P. Bradshaw.

Appendix. Numerical procedures

The deforming coordinate system (2.9a) results in momentum and continuity equations that are very similar to those governing conventional Poiseuille flow. Because of this similarity, we are able to benefit from previous code development and testing, and construct an accurate and efficient solver by making straight-forward alterations to a well-established algorithm.

The conversion begins by recasting (2.10) into the (v, ω_y) formulation employed by Kim *et al.* For the present flow we write

$$\frac{\partial}{\partial t} \widehat{\nabla}^2 v^* = \widehat{h}_v + \frac{1}{Re} \widehat{\nabla}^2 (\widehat{\nabla}^2 v^*), \quad (\text{A } 1a)$$

$$\frac{\partial \widehat{g}}{\partial t} = \widehat{h}_g + \frac{1}{Re} \widehat{\nabla}^2 \widehat{g}, \quad (\text{A } 1b)$$

$$\widehat{f} + \mathcal{B}_{22} \frac{\partial v^*}{\partial \xi_2} = 0, \quad (\text{A } 1c)$$

where $\hat{g} = \hat{\omega}_2$ is the wall-normal component of vorticity, $\hat{\omega}_i = \epsilon_{ijk} \mathcal{B}_{nj} \partial u_k^* / \partial \xi_n$, and

$$\hat{\nabla}^2(\cdot) = \mathcal{B}_{11}^2 \frac{\partial^2(\cdot)}{\partial \xi_1 \partial \xi_1} + \mathcal{B}_{22}^2 \frac{\partial^2(\cdot)}{\partial \xi_2 \partial \xi_2} + \mathcal{B}_{33}^2 \frac{\partial^2(\cdot)}{\partial \xi_3 \partial \xi_3},$$

with

$$\hat{f} = \mathcal{B}_{11} \frac{\partial u^*}{\partial \xi_1} + \mathcal{B}_{33} \frac{\partial w^*}{\partial \xi_3}, \quad \hat{g} = \mathcal{B}_{33} \frac{\partial u^*}{\partial \xi_3} - \mathcal{B}_{11} \frac{\partial w^*}{\partial \xi_1}, \quad (\text{A } 1d)$$

$$\begin{aligned} \hat{h}_v = & -\mathcal{B}_{22} \frac{\partial}{\partial \xi_2} \left(\mathcal{B}_{11} \frac{\partial \hat{H}_1}{\partial \xi_1} + \mathcal{B}_{33} \frac{\partial \hat{H}_3}{\partial \xi_3} \right) + \mathcal{B}_{11}^2 \frac{\partial^2 \hat{H}_2}{\partial \xi_1 \partial \xi_1} + \mathcal{B}_{33}^2 \frac{\partial^2 \hat{H}_2}{\partial \xi_3 \partial \xi_3} \\ & + \mathcal{B}_{22} \frac{\partial}{\partial \xi_2} \left(\mathcal{B}_{11} \mathcal{A}_{11}^* \frac{\partial u^*}{\partial \xi_1} + \mathcal{B}_{33} \mathcal{A}_{33}^* \frac{\partial w^*}{\partial \xi_3} \right) \\ & - 2\mathcal{B}_{11}^2 \mathcal{A}_{11}^* \frac{\partial^2 v^*}{\partial \xi_1 \partial \xi_1} - \mathcal{B}_{22}^2 \mathcal{A}_{22}^* \frac{\partial^2 v^*}{\partial \xi_2 \partial \xi_2} - 2\mathcal{B}_{33}^2 \mathcal{A}_{33}^* \frac{\partial^2 v^*}{\partial \xi_3 \partial \xi_3}, \end{aligned} \quad (\text{A } 1e)$$

$$\hat{h}_g = \mathcal{B}_{33} \frac{\partial \hat{H}_1}{\partial \xi_3} - \mathcal{B}_{11} \frac{\partial \hat{H}_3}{\partial \xi_1} - \mathcal{B}_{33} \mathcal{A}_{33}^* \frac{\partial u^*}{\partial \xi_3} + \mathcal{B}_{11} \mathcal{A}_{11}^* \frac{\partial w^*}{\partial \xi_1}, \quad (\text{A } 1f)$$

and

$$\hat{H}_i = -\frac{\partial \bar{p}}{\partial x_i} \Big|_{\text{app}} + \epsilon_{ijk} u_j^* \hat{\omega}_k - u_j^* \mathcal{A}_{ij}^*. \quad (\text{A } 1g)$$

Equation (A 1) is equivalent to Kim *et al.*'s equations (3)–(5), except for the new terms involving the applied strain \mathcal{A}_{ij}^* , and the time-dependent metric $\mathcal{B}_{ij}(\hat{t}) = \exp(-\mathcal{A}_{ij}^* \hat{t})$ multiplying each spatial derivative.

We can utilize the Kim *et al.* algorithm simply by replacing their dependent variables $\nabla^2 v$ and g with $\hat{\nabla}^2 v^*$ and \hat{g} , with the understanding that their time and spatial derivatives $\partial(\cdot)/\partial t$ and $\partial(\cdot)/\partial x_i$ now correspond respectively to $\partial(\cdot)/\partial \hat{t}$ and $\mathcal{B}_{ji} \partial(\cdot)/\partial \xi_j$, and $\nabla^2(\cdot) \leftarrow \hat{\nabla}^2(\cdot)$, $h_v \leftarrow \hat{h}_v$, $h_g \leftarrow \hat{h}_g$, and $H_i \leftarrow \hat{H}_i$. Actual coding changes therefore involve multiplying all spatial derivatives by the appropriate explicit time-dependent function $\mathcal{B}_{ij}(\hat{t})$ (with attention paid to the elapsed time, and an appropriate distinction between spatial derivatives associated with 'previous', 'current', and 'upcoming' timesteps), and adding the \mathcal{A}_{ij}^* terms to h_v , h_g , and the convective term H_i . The latter requires modification of the CFL number definition, as in Blaisdell, Mansour & Reynolds (1991).

The other major change is to the wall-boundary conditions, to allow the non-zero in-plane motion u_w^* prescribed by (2.14). This requires monitoring the initial and current mean centreline velocity, and saving the initial values during stops and restarts of the code.

All other characteristics of the solution procedure are identical to those detailed in Kim *et al.* (1987).

REFERENCES

- ALVING, A. E. & FERNHOLZ, H. H. 1995 Mean-velocity scaling in and around a mild, turbulent separation bubble. *Phys. Fluids* **7**, 1956–1969.
- ANDERSON, S. D. & EATON, J. K. 1989 Reynolds stress development in pressure-driven three-dimensional turbulent boundary layers. *J. Fluid Mech.* **202**, 263–294.

- BERG, B. VAN DEN, ELSENAAR, A., LINDHOUT, J. P. F. & WESSELING, P. 1975 Measurements in an incompressible three-dimensional turbulent boundary layer, under infinite swept-wing conditions, and comparison with theory. *J. Fluid Mech.* **70**, 127–148.
- BERG, B. VAN DEN, HUMPHREYS, D. A., KRAUSE, E. & LINDHOUT, J. P. F. 1988 *Three-Dimensional Turbulent Boundary Layers—Calculations and Experiments*. Notes on Numerical Fluid Mechanics, vol. 19. Vieweg & Sohn.
- BLAISDELL, G. A., MANSOUR, N. N. & REYNOLDS, W. C. 1991 Numerical simulation of compressible homogeneous turbulence. *Dept. of Mech. Engng, Stanford University, Thermosciences Div. Rep. TF-50*.
- BRADSHAW, P. 1987 Turbulent secondary flows. *Ann. Rev. Fluid Mech.* **19**, 53–74.
- BRADSHAW, P. & PONTIKOS, N. S. 1985 Measurements in the turbulent boundary layer on an ‘infinite’ swept wing. *J. Fluid Mech.* **159**, 105–130.
- COLEMAN, G. N. 1999 Similarity statistics from a direct numerical simulation of the neutrally stratified planetary boundary layer. *J. Atmos. Sci.* **56**, 891–900.
- COLEMAN, G. N., FERZIGER, J. H. & SPALART, P. R. 1990 A numerical study of the turbulent Ekman layer. *J. Fluid Mech.* **213**, 313–348.
- COLEMAN, G. N., KIM, J. & LE, A.-T. 1996a A numerical study of three-dimensional wall-bounded flows. *Intl J. Heat Fluid Flow* **17**, 333–342.
- COLEMAN, G. N., KIM, J. & SPALART, P. R. 1996b Direct numerical simulation of strained three-dimensional wall-bounded flows. *Expl Thermal Fluid Sci.* **13**, 239–251.
- COLEMAN, G. N., KIM, J. & SPALART, P. R. 1997 Direct numerical simulation of decelerated wall-bounded shear flows. *Eleventh Symp. on Turbulent Shear Flows*, Grenoble, France, September 8–10, 1997.
- DRIVER, D. M. & HEBBAR, S. K. 1987 Experimental study of a three-dimensional, shear-driven, turbulent boundary layer. *AIAA J.* **25**, 35–42.
- DRIVER, D. M. & HEBBAR, S. K. 1991 Three-dimensional turbulent boundary layer flow over a spinning cylinder. *NASA Tech. Memo.* 102240.
- EATON, J. K. 1995 Effects of mean flow three dimensionality on turbulent boundary-layer structure. *AIAA J.* **33**, 2020–2025.
- FERNHOLZ, H. H. & VAGT, J.-D. 1981 Turbulence measurements in an adverse-pressure-gradient three-dimensional turbulent boundary layer along a circular cylinder. *J. Fluid Mech.* **111**, 233–269.
- FURUYA, Y., NAKAMURA, I. & KAWACHI, H. 1966 The experiment on the skewed boundary layer on a rotating body. *Bull. Japan Soc. Mech. Engng* **9**, 702–710.
- FLACK, K. A. & JOHNSTON, J. P. 1993 Near-wall investigation of three-dimensional turbulent boundary layers. *Dept. of Mech. Engng, Stanford University, Thermosciences Div. Rep. MD-63*.
- GLEYZES, C., MACIEL, Y., COUSTEIX, J., GOODEN, J. H. M., REINDERS, W., BERG, B. VAN DEN 1993 Three-dimensional turbulent flow around the Garteur swept wing. In *Ninth Symp. on Turbulent Shear Flows*, Kyoto, Japan, August 16–18, 1993.
- HAWTHORNE, W. R. 1951 Secondary circulation in fluid flow. *Proc. R. Soc. Lond. A* **206**, 374–387.
- HAWTHORNE, W. R. 1954 The secondary flow about struts and airfoils. *J. Aeronaut. Sci.* **21**, 588–608.
- HOWARD, R. J. A. & SANDHAM, N. D. 1996 Simulation and modelling of the skew response of turbulent channel flow to spanwise flow deformation. In *Second ERCOFTAC Workshop on Direct and Large-Eddy Simulation*, Grenoble, France, September 14–18, 1996.
- JOHNSTON, J. P. & FLACK, K. A. 1996 Review of advances in three-dimensional turbulent boundary layers with emphasis on the wall-layer regions. *Trans. ASME: J. Fluids Engng* **118**, 219–232.
- JUNG, W. J., MANGIAVACCHI, N. & AKHAVAN, R. 1992 Suppression of turbulence in wall-bounded flows by high-frequency spanwise oscillations. *Phys. Fluids A* **4**, 1605–1607.
- KANG, H. S., CHOI, H. & YOO, J. Y. 1998 On the modification of the near-wall coherent structure in a three-dimensional turbulent boundary layer on a free rotating disk. *Phys. Fluids* **10**, 2315–2322.
- KIESOW, R. Q. & PLESNIAK, M. W. 1999 Modification of near-wall structure in a three-dimensional turbulent boundary layer. In *First Symp. on Turbulence and Shear Flow Phenomena*, University of California, Santa Barbara, USA, September 13–15, 1999.
- KIM, J., MOIN, P. & MOSER, R. 1987 Turbulence statistics in fully developed channel flow at low Reynolds number. *J. Fluid Mech.* **177**, 133–166.
- LAADHARI, F., SKANDAJI, L. & MOREL, R. 1994 Turbulence reduction in a boundary layer by a local spanwise oscillating surface. *Phys. Fluids* **6**, 3218–3220.

- LANCZOS, C. 1956 *Applied Analysis*. Prentice-Hall.
- LE, A.-T. 1999 A numerical study of three-dimensional boundary layers. PhD thesis, University of California, Los Angeles.
- LE, A.-T., COLEMAN, G. N. & KIM, J. 1999 Near-wall turbulence structures in three-dimensional boundary layers. In *First Symp. on Turbulence and Shear Flow Phenomena, University of California, Santa Barbara, USA, September 13–15, 1999*.
- LEE, M. J. & REYNOLDS, W. C. 1985 Numerical experiments on the structure of homogeneous turbulence. *Dept. of Mech. Engng, Stanford University, Thermosciences Div. Rep. TF-24*.
- LITTEL, H. S. & EATON, J. K. 1994 Turbulence characteristics of the boundary layer on a rotating disk. *J. Fluid Mech.* **266**, 175–207.
- LOHMANN, R. P. 1976 The response of a developed turbulent boundary layer to local transverse surface motion. *Trans. ASME: J. Fluids Engng* **98**, 354–363.
- MANSOUR, N. N., KIM, J. & MOIN, P. 1988 Reynolds-stress and dissipation-rate budgets in a turbulent channel flow. *J. Fluid Mech.* **194**, 15–44.
- MOIN, P., SHIH, T.-H., DRIVER, D. M. & MANSOUR, N. N. 1990 Direct numerical simulation of a three-dimensional turbulent boundary layer. *Phys. Fluids A* **2**, 1846–1853.
- NAGANO, Y., TAGAWA, M. & TSUJI, T. 1991 Effects of adverse pressure gradients on mean flows and turbulence statistics in a boundary layer. In *Eighth Symp. on Turbulent Shear Flows, Munich, Germany, September 9–11, 1991*.
- ÖLÇMEN, S. M. & SIMPSON, R. L. 1995 An experimental study of a three-dimensional pressure-driven turbulent boundary layer. *J. Fluid Mech.* **290**, 225–262.
- PIERCE, F. J. & DUERSON, S. H. JR. 1975 Reynolds stress tensors in an end-wall three-dimensional channel boundary layer. *Trans. ASME: J. Fluids Engng* **97**, 618–620.
- ROGALLO, R. S. 1981 Numerical experiments in homogeneous turbulence. *NASA Tech. Memo.* 81315. Available from NASA Scientific & Technical Information (help@sti.nasa.gov).
- ROGERS, M. M. 2000 The evolution of strained turbulent plane wakes. *J. Fluid Mech.* (accepted).
- SCHWARZ, W. R. & BRADSHAW, P. 1994 Turbulence structural changes for a three-dimensional turbulent boundary layer in a 30° bend. *J. Fluid Mech.* **272**, 183–209.
- SENDSTAD, O. & MOIN, P. 1992 The near wall mechanics of three-dimensional turbulent boundary layers. *Dept. of Mech. Engng, Stanford University, Thermosciences Div. Rep. TF-57*.
- SMITS, A. J. & WOOD, D. H. 1985 The response of turbulent boundary layers to sudden perturbations. *Ann. Rev. Fluid Mech.* **17**, 321–358.
- SPALART, P. R. 1989 Theoretical and numerical study of a three-dimensional turbulent boundary layer. *J. Fluid Mech.* **205**, 319–340.
- SPALART, P. R. & COLEMAN, G. N. 1997 Numerical study of a separation bubble with heat transfer. *Eur. J. Mech. B/Fluids* **16**, 169–189.
- SPALART, P. R., MOSER, R. D. & ROGERS, M. M. 1991 Spectral methods for the Navier–Stokes equations with one infinite and two periodic directions. *J. Comput. Phys.* **96**, 297–324.
- SPALART, P. R. & WATMUFF, J. H. 1993 Experimental and numerical study of a turbulent boundary layer with pressure gradients. *J. Fluid Mech.* **249**, 337–371.
- SQUIRE, H. B. & WINTER, K. G. 1951 The secondary flow in a cascade of airfoils in a nonuniform stream. *J. Aeronaut. Sci.* **18**, 271–277.
- WEBSTER, D. R., DEGRAFF, D. B. & EATON, J. K. 1996 Turbulence characteristics of a boundary layer over a swept bump. *J. Fluid Mech.* **323**, 1–22.
- WILCOX, D. C. 1998 *Turbulence Modeling for CFD*. DCW Industries (www.dcwindustries.com).
- WU, X. & SQUIRES, K. D. 1997 Large eddy simulation of an equilibrium three-dimensional turbulent boundary layer. *AIAA J.* **35**, 67–74.

Near-wall turbulence structures in three-dimensional boundary layers

Anh-Tuan Le ^{*}, Gary N. Coleman ¹, John Kim

Department of Mechanical and Aerospace Engineering, UCLA, Los Angeles, CA 90095-1597, USA

Abstract

We examine the structure of near-wall turbulence in three-dimensional boundary layers (3DBLs), which we approximate by applying an impulsive spanwise motion to the lower wall of a turbulent channel flow. Direct numerical simulation (DNS) data are analysed using probability density functions (PDFs), conditional-averaged quadrant analysis about Reynolds-stress-producing events, and visualization of vortices with the λ_2 -criterion. The evidence suggests that mean three-dimensionality breaks up the symmetry and alignment of near-wall structures, disrupting their self-sustaining mechanisms, and thereby causing a reduction in the turbulence kinetic energy (TKE). © 2000 Begell House Inc. Published by Elsevier Science Inc. All rights reserved.

1. Introduction

In a three-dimensional boundary layer (3DBL) the mean flow direction changes with distance from the wall, and the turbulent stresses are not aligned with the mean shear. In many cases, the result is a decrease in TKE and Reynolds shear stress compared to an equivalent two-dimensional boundary layer (2DBL). Although 3DBLs exist in which these statistics increase (see listing in Johnston and Flack, 1996), the flowfields in those cases also contain adverse pressure gradients (not a 3D effect), which are known to increase the TKE in the outer regions of the boundary layer. In practice (for example, for the flow over a swept wing) the adverse pressure gradient can dominate over the 3D effects (Coleman et al., 1997). Even in such flows, however, three-dimensionality serves to damp the turbulence in the near-wall region. Moreover, the ratio of the turbulent shear stress to the TKE is generally found to decrease relative to 2DBLs, signifying a reduction in the effectiveness of the turbulence in extracting kinetic energy from the mean flow.

The mechanism by which the turbulence quantities discussed above are altered has been a subject of much debate. For example, Anderson and Eaton (1989) suggested that the spanwise flow reduces the strength of quasi-streamwise vortices having the opposite sign of streamwise vorticity to the mean spanwise flow, reducing the mixing that occurs between vortices of opposite signs. Shizawa and Eaton (1990) found that artificially-generated vortices of either sign embedded into the boundary layer decay faster than they would in a 2DBL, but vortices whose near-wall spanwise velocity is in the same direction as the crossflow produce weakened ejections. Littel

and Eaton (1994) found that the crossflow inhibits strong *sweeps* from vortices having near-wall spanwise velocity in the same direction as the crossflow, while it inhibits strong *ejections* from vortices having spanwise velocity in the opposite direction. Kang et al. (1998) concluded that the asymmetries in the conditional averages of Littel and Eaton (1994) are only caused by non-Reynolds-stress-producing events. Sendstad and Moin (1992) advanced four mechanisms by which the spanwise crossflow affects particle trajectories in the vortical structures, each important at different times, which serve to generate lower Reynolds stress and break up the near-wall streaks. Their findings are, in general, consistent with those of Littel and Eaton. However, the mechanisms described by Sendstad and Moin assume that near-wall vortices are aligned horizontally in the 2D flow, act as independent units on the surrounding fluid, and respond in a 2D manner to the spanwise shear. More recent studies of coherent structures in 2DBLs, both experimental and numerical, indicate that near-wall turbulence structures generally have a finite inclination to the wall, and interact in a cooperative manner to perpetuate turbulence (e.g., Jeong et al., 1997; Tomkins et al., 1998).

In earlier work (Coleman et al., 1996) we found that applying mean spanwise shear $\partial W/\partial y$ anywhere in the near-wall region of an initially 2D flow reduces the mean streamwise skin friction, with the greatest reduction occurring when $\partial W/\partial y$ is applied between approximately $y^+ = 5$ and 15 (where y^+ is the wall-normal distance in wall units). While this finding has significant practical implications (indicating, for example, where drag-reduction control schemes should focus), it does not give a detailed picture of the manner in which mean three-dimensionality modifies near-wall structures in practice. The objective of the present study is to obtain additional insight into the behavior of the near-wall structures that are responsible for the observed changes in 3DBL turbulence, by employing a combination of statistical and visualization techniques. The results may lead to improvements in turbulence models and suggest new methods for turbulence control.

^{*} Corresponding author. Fax: +1-310-206-4830.

E-mail address: anhtuan@seas.ucla.edu (A.-T. Le).

¹ Present address: School of Engineering Sciences, University of Southampton, Highfield, Southampton SO17 1BJ, UK.

2. Approach

All solutions are obtained using DNS. Probability density functions (PDFs) of velocity and vorticity are used to analyse the data. We also employ the conditional-averaged quadrant analysis introduced by Kang et al. (1998). Vortical structures within the flowfields are visualized using the λ_2 -criterion of Jeong and Hussain (1995), whereby vortices are associated with negative values of λ_2 , defined as the second largest eigenvalue of the tensor $S_{ik}S_{kj} + \Omega_{ik}\Omega_{kj}$, where $S_{ij} = (u_{i,j} + u_{j,i})/2$ and $\Omega_{ij} = (u_{i,j} - u_{j,i})/2$ are the strain and rotation tensors, respectively. Here the subscripts (i, j, k) may have values $(1, 2, 3)$ which correspond respectively to the streamwise, wall-normal, and spanwise directions, such that $(x_1, x_2, x_3) = (x, y, z)$ and $(u_1, u_2, u_3) = (u, v, w)$.

Our discussion will focus on results obtained by the time-evolving 3DBL generated from an impulsive spanwise-moving wall in a fully developed turbulent channel flow. In the interest of demonstrating the generality of the underlying physics, we will also discuss statistical results from numerical experiments on the Ekman layer, a statistically stationary 3DBL.

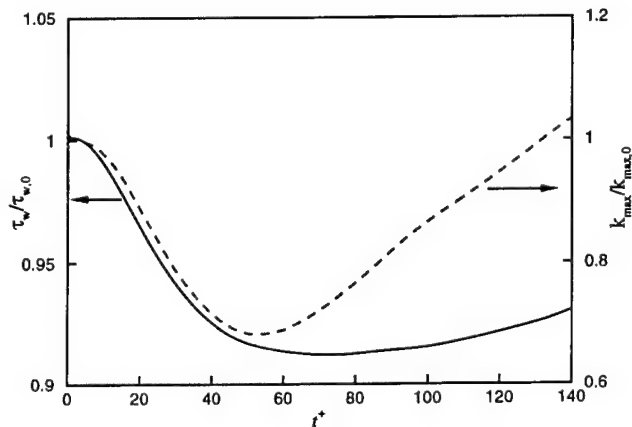


Fig. 1. History of streamwise wall shear and maximum TKE, normalized by value at initial condition, in channel with spanwise moving wall: — τ_w ; --- k_{\max} .

3. Results

The initial fields, at $Re_\tau = 180$, are similar to that of Kim et al. (1987), except that a wider domain with greater streamwise grid resolution is used to accommodate the realignment of the mean flow caused by the moving wall. The results of simulations started from five independent initial fields are averaged into the statistics shown here, three of which have the domain size $4\pi \times 2 \times 8\pi/3$ with $256 \times 129 \times 256$ grid points in the streamwise, wall-normal, and spanwise directions, respectively, and two of which have the domain size $8\pi \times 2 \times 16\pi/3$ with $512 \times 129 \times 512$ grid points. Here, the domain size is normalized by the channel half-height.

Starting from a statistically steady 2D state, the wall is set in motion in the spanwise direction at time $t^+ = 0.0$ with velocity $W_s^+ = -8.5$, generating a spanwise mean shear with positive streamwise vorticity which diffuses from the wall into the flowfield (we use a '+' superscript throughout to indicate scaling with respect to wall units of the initial unperturbed flow). Reynolds stress, TKE, and the stress-energy ratio initially decrease, then recover (see Coleman et al., 1996). A corresponding reduction in streamwise wall shear is observed with a similar time scale (Fig. 1). For the sake of discussion, we refer to the time interval when the TKE and streamwise wall shear are decreasing ($t^+ < 60$) as the *reduction* period, with *early reduction* indicating the period when the rate of decrease is accelerating ($t^+ < 20$), and *late reduction* when the decrease is slowing down ($20 < t^+ < 60$). The period during which the drag and peak TKE increase with time from their minima ($t^+ > 60$) is denoted as the *recovery* period.

As we are mainly interested in the mechanisms that reduce turbulence intensity and drag, the present analysis focuses on changes in the flowfield during the reduction period. Throughout this period, the Reynolds stress and mean shear are not aligned, as illustrated in Fig. 2, which shows the development of the lag angle $\lambda = \gamma_s - \gamma_\tau$, where γ_s and γ_τ respectively represent the angles of the mean velocity gradient and turbulent shear stresses in the x - z plane reference frame

$$\gamma_s \equiv \arctan \left(\frac{\partial W / \partial y}{\partial U / \partial y} \right), \quad \gamma_\tau \equiv \arctan \left(\frac{\overline{v'w'}}{\overline{u'v'}} \right).$$

The lag angle decreases in time as the turbulence adjusts to the mean shear. During recovery, the wall-normal variation in the shear angles diminishes and turbulence-mean lag becomes

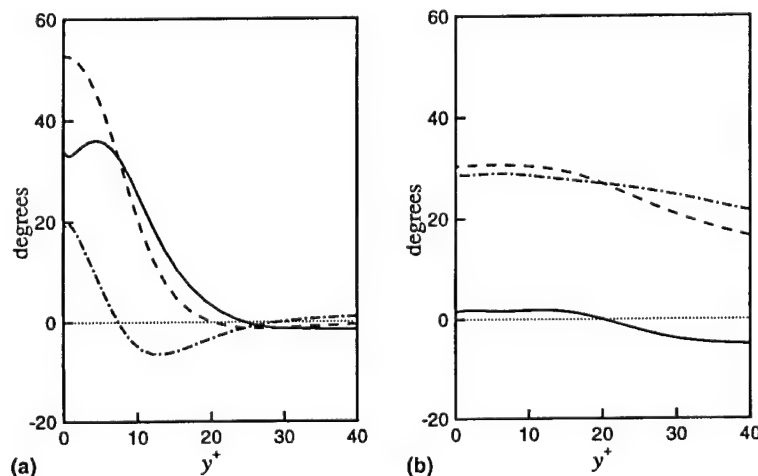


Fig. 2. Shear angles in channel with spanwise moving wall: --- γ_s , mean shear angle; - · - γ_τ , turbulent shear angle; — λ , lag angle: (a) $t^+ = 13.5$; (b) $t^+ = 135$.

negligible; the flow in the near-wall region therefore becomes *collateral* – i.e., effectively 2D (Fig. 2(b)).

3.1. PDF analysis

Previous research indicated that 3DBLs exhibit asymmetries between the flow induced by vortices having the same and opposite signs of vorticity as the spanwise shear layer (henceforth referred to as *positive* and *negative* vortices, respectively). Assertions have also been made that the sweeps and ejections from near-wall vortices are affected in different ways by the three-dimensionality. We seek to verify these findings by examining the PDFs of the velocity field in the 3D channel flow.

Fig. 3 shows a weighted joint PDF of u' and v' in the 3D channel at $y^+ = 10$, a location where sweeps and ejections are initially similar in strength. The distribution is weighted by $u'v'$, which reveals how each velocity component contributes to the $-\overline{u'v'}$ shear stress. The most important changes to the total Reynolds shear stress early in the flow history are experienced by the streamwise component $-\overline{u'v'}$, since the spanwise fluctuating velocity is slow to respond to the mean spanwise shear. This is demonstrated in Fig. 3(a) and (b), where the u' and v' distributions in the channel coordinates (those aligned with the initial 2D flow) are essentially the same as those that have been aligned with the Reynolds-stress angle γ_r , implying that the spanwise contribution is insignificant at these times. Later, as the turbulence adjusts to the spanwise perturbation, the

spanwise component becomes more significant, which is manifest in the difference between the distributions in the channel frame of reference and that aligned with γ_r (Fig. 3(c)). These figures show that ejections (events that produce Reynolds shear stress in the second quadrant, or Q2) are affected most significantly by reductions in strong negative u' , while sweeps (fourth-quadrant, or Q4, events) are affected by reductions in both u' and v' . Sendstad and Moin (1992) studied a similar time-developing 3D channel flow in which the spanwise shear was created by an impulsive constant pressure gradient. In their DNS study, the effective wall velocity increases linearly from zero, rather than being a step function as in the present case. Nevertheless, much of the behavior of the two flows is similar. They attributed the changes in the fluctuating velocity distribution to modification by the spanwise shear of the trajectories of fluid about streamwise vortices.

To determine the dependence of $-\overline{u'v'}$ on the sign of the streamwise vortex, we condition the weighted joint PDF of u' and v' above with the sign of streamwise vorticity. Fig. 4 reveals that ejections associated with negative ω'_x are reduced to a much greater extent than the sweeps, while the sweeps associated with positive ω'_x are reduced to a much greater degree than ejections. This is consistent with the findings of Sendstad and Moin (1992) and those of Littel and Eaton's rotating disk study (1994), suggesting that the mechanisms affecting the turbulence are the same in both time-evolving and stationary 3DBLs.

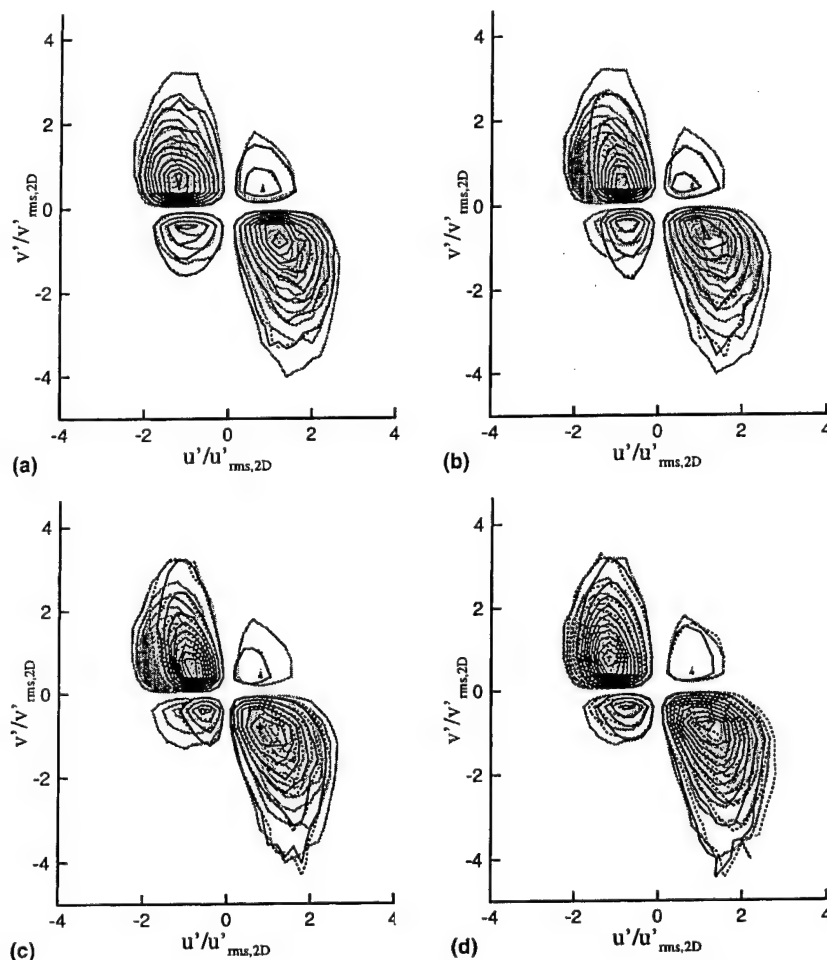


Fig. 3. Weighted joint PDF of u' and v' in channel with spanwise moving wall at $y^+ = 10$: — 3D distribution; 3D, aligned with Reynolds-stress angle γ_r ; shaded lines denote initial-condition contours: (a) $t^+ = 13.5$; (b) $t^+ = 27$; (c) $t^+ = 54$; (d) $t^+ = 135$.

The joint PDF of streamwise and spanwise vorticity also produces some revealing results. Fig. 5 shows the distribution of vorticity at $y^+ = 10$ at various times for the 3D flow. Unlike

the Reynolds shear stress, for which the contour shapes are similar regardless of the frame of reference, the major axis of the vorticity distribution rotates as the flow develops.

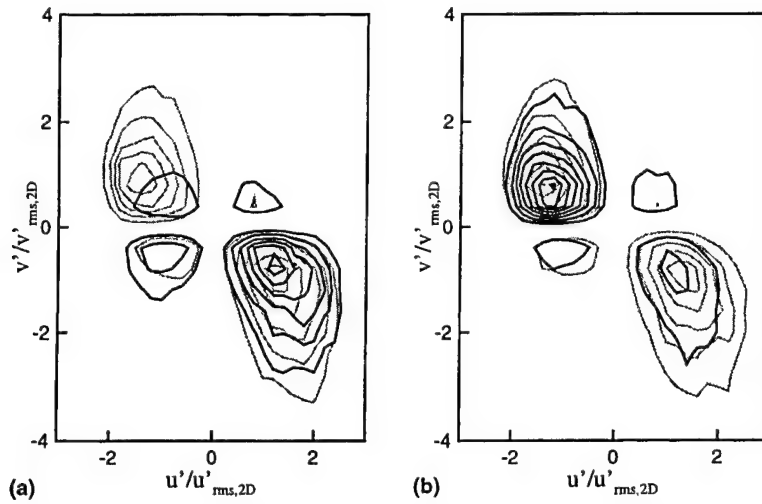


Fig. 4. Weighted joint PDF of u' and v' in channel with spanwise moving wall at $y^+ = 10$ and $t^+ = 13.5$, conditioned on ω'_x ; shaded lines denote initial-condition contours: (a) $\omega'_x < 0$; (b) $\omega'_x > 0$.

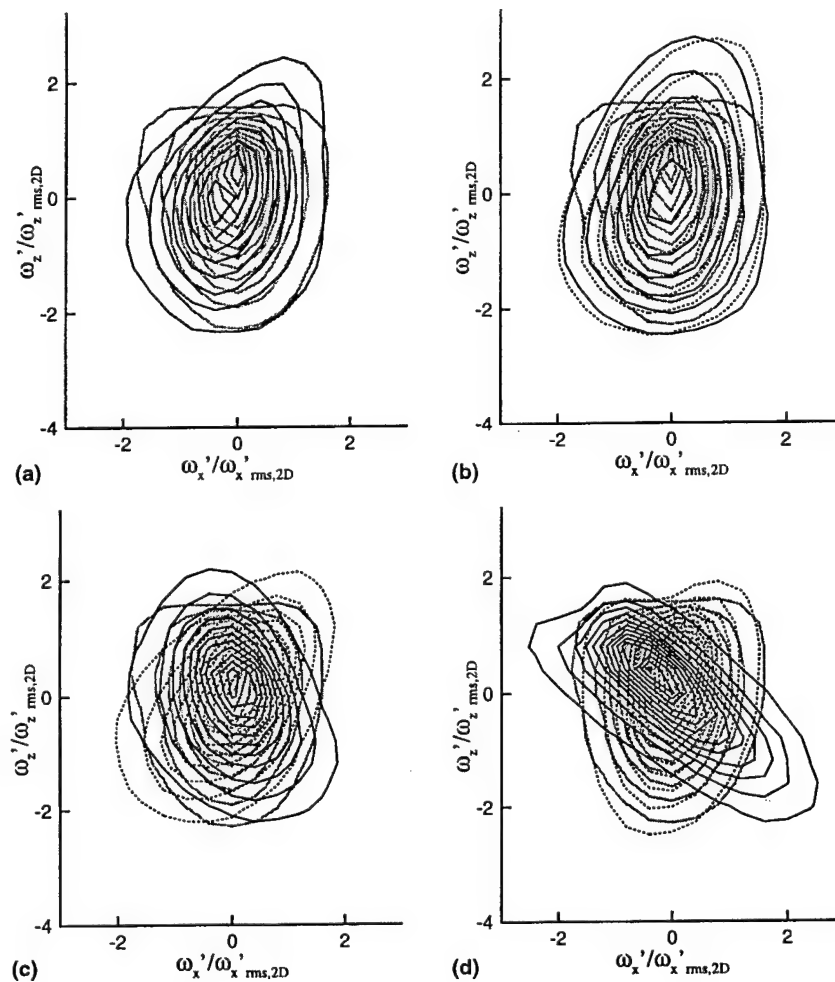


Fig. 5. Joint PDF of ω'_x and ω'_z in channel with spanwise moving wall at $y^+ = 10$: — 3D distribution, 3D distribution aligned with turbulence intensity angle γ_1 ; shaded lines denote initial 2D value: (a) $t^+ = 13.5$; (b) $t^+ = 27$; (c) $t^+ = 54$; (d) $t^+ = 135$.

Experience indicates that this rotation is well defined by the *turbulence intensity angle*, γ_1 , namely, the orientation of the principal axis of the planar turbulence shear stresses in the x - z plane. This angle is defined as

$$\gamma_1 = \frac{1}{2} \arctan \left(\frac{2\overline{u'w'}}{\overline{u'^2} - \overline{w'^2}} \right).$$

In Fig. 5, the dotted lines denote the vorticity distribution in the frame of reference aligned with γ_1 . Since the γ_1 reference frame accounts for the bulk turning of the vorticity field caused by the moving wall, changes in the shapes of the dotted-curve distribution can be interpreted as evidence of structural modifications of the turbulence.

With the introduction of three-dimensionality, the vorticity magnitude at $y^+ = 10$ increases until $t^+ = 27$, after which it slowly decreases (Coleman et al., 1996). An interesting asymmetry appears in the ω'_z distribution, where positive ω'_z associated with positive ω'_x is increased, while positive ω'_z associated with negative ω'_x is decreased. Note that ω'_x itself does not exhibit appreciable asymmetry. The lack of asymmetry is shown in Fig. 6, where the PDF of ω'_x in the frame of reference aligned with γ_1 remains generally symmetric throughout the flow history. This suggests that the vortical structures, which initially are essentially streamwise at this wall-normal location, are not strongly asymmetric in the 3D flow; rather the shear layers or streaks generated by the vortices are affected differently depending on the sign of the vortex. The asymmetry in the spanwise vorticity decreases as the flow recovers.

The contours of u' in the y - z plane shown in Fig. 7 provide a clue to the source of increased spanwise vorticity near the wall. As the wall moves in the spanwise direction, it carries along the fluid next to it, straining the near-wall streaks and causing them to become layered in the wall-normal direction. The resulting velocity gradients, most pronounced at the interface between positive and negative u' , represent an increase in spanwise vorticity, ω'_z . It is this layering that increases dissipation during the reduction period, signified by the enstrophy increase observed by Coleman et al. (1996), which contributes to the turbulence kinetic energy reduction. Note that the

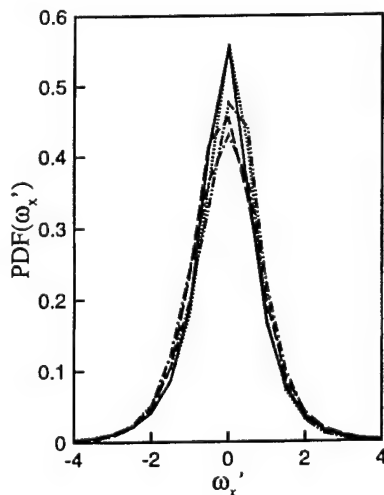


Fig. 6. PDF of streamwise vorticity at $y^+ = 10$ in channel with spanwise moving wall, reference frame aligned with turbulence intensity angle γ_1 : — $t^+ = 0$, --- $t^+ = 13.5$, - · - · - $t^+ = 27$, - - - $t^+ = 54$, $t^+ = 135$.

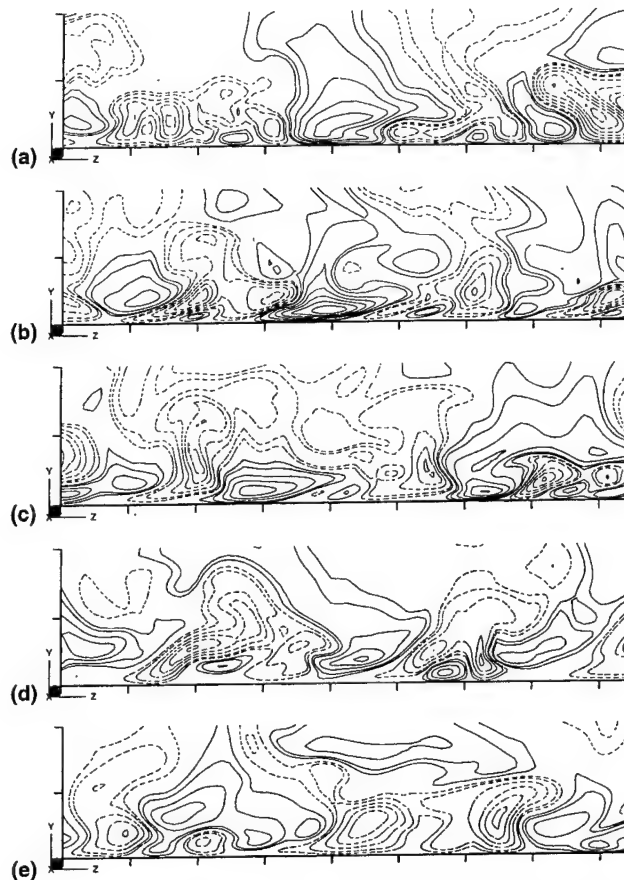


Fig. 7. Contours of u' in y - z plane of channel with a spanwise-moving wall: — $u' > 0$, --- $u' < 0$; tickmarks on z -axis represent 50 wall units: (a) initial 2D flow; (b) $t^+ = 13.5$; (c) $t^+ = 27$; (d) $t^+ = 54$; (e) $t^+ = 135$.

layering decreases as the turbulence recovers toward a new 2D state.

We offer an explanation for the ω'_z asymmetry using the schematic diagram in Fig. 8. In a 2DBL, a near-wall streamwise vortex generates a high-speed streak by sweeping high-speed fluid toward the wall and a low-speed streak by ejecting low-speed fluid away from the wall. In the y - z cross-section shown, a positive vortex (one having $\omega'_x > 0$ at its core) has the high-speed streak on the right and the low-speed streak on the left, and vice versa for a negative vortex. In the 3D flow generated by a spanwise-moving wall, the lower part of the streaks move in the spanwise direction, so that the streaks become layered as in Fig. 7. For the positive vortex, the high-speed streak is pulled under the low-speed streak, forming a vertical interface having positive ω'_z , and lessening the probability of an interface with negative ω'_z . Thus, positive ω'_z associated with positive ω'_x is increased, while negative ω'_z associated with positive ω'_x is decreased. A similar effect occurs with the negative vortex, strengthening negative ω'_z associated with negative ω'_x , etc. However, since high- and low-speed streaks have different distributions near the wall (high-speed streaks are stronger near the wall, and have wider spanwise extents due to the 'splatting' effect) the near-wall layering associated with the negative vortex is likely to generate a different, perhaps weaker, vertical interface. Thus, the increases in vorticity that occur in the first and third quadrants of the vorticity PDF (in Fig. 5) are not identical. This mechanism is similar to that observed by Dhanak and Si (1999) in their 2D model of a near-wall vortex in the presence of wall oscillations, wherein the oscillations promote the mixing of high- and low-speed streaks.

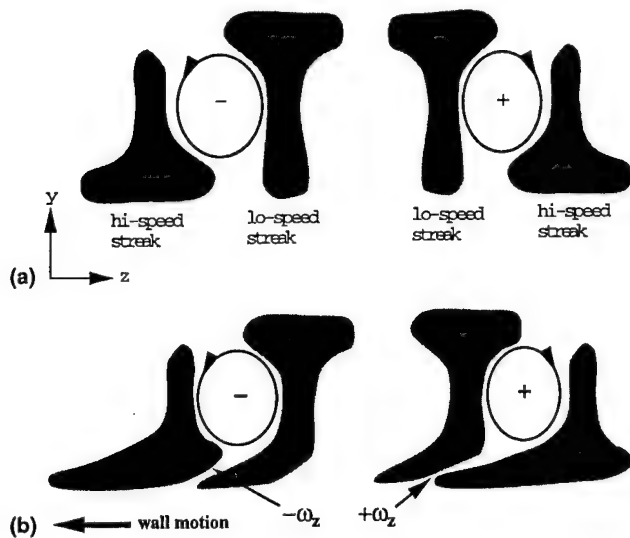


Fig. 8. Schematic of redistribution of vorticity due to streak deformation due to a spanwise-moving wall: (a) initial 2D flow; (b) 3D flow.

3.2. Conditional-averaged quadrant analysis

To isolate the important near-wall structures we examine events that are characteristic of vortical motions. Kang et al. (1998) investigated the velocity fields about strong sweeps and ejections in their rotating disk experiment by averaging about locations containing high Reynolds shear stress, then performing a quadrant analysis on the conditional-averaged quantities. Here we apply the same procedure to the 3D channel flow.

Fig. 9 illustrates the distribution of the Reynolds shear stress about strong sweeps and ejections at $y^+ = 10$ in the 3D channel, *strong* indicating events for which $-u'v' > 2u'_{rms}v'_{rms}$, with *sweeps* having $v' < 0$ and *ejections* having $v' > 0$. Here, the frame of reference is aligned with the Reynolds stress angle γ_r . The center peak in each plot, depicting a strong sweep or ejection, is flanked by two secondary peaks generated by the opposite event. Because near-wall Reynolds shear stress is for the most part associated with near-wall vortical motion, Kang et al. (1998) postulated that these peaks represent the signature of a pair of streamwise vortices that generate the strong Rey-

nolds-stress-producing event. The center peak in each plot contains the combined effect of both vortices, while the secondary peaks contain the effect of an *individual* vortex. Therefore, asymmetries in the Reynolds shear stress production by the vortices can be discerned by comparing the secondary peaks. In Fig. 9(a) the left secondary peak represents the sweep of a *negative* vortex (counter-clockwise with respect to Fig. 9) while the right secondary peak represents the sweep of a *positive* one. Both are dominated by Q4 events. Conversely, in Fig. 9(b) the vortices are positive on the left and negative on the right, and the secondary peaks, dominated by Q2 events, represent ejections from the vortices. Note that at $y^+ = 10$ the Q4 events are more pronounced than the Q2 events in both 2D and 3D flows (the Q4 peaks are more prominent than the Q2 peaks these figures). As z^+ increases, the correlations between structures decrease, and the value of the total conditional average approaches unity, i.e., the average becomes $\overline{u'v'}$ (not conditional). The components from all the quadrants then sum to unity.

In contrast to the roughly symmetric secondary peaks in the initial 2D field (shown as shaded lines), the 3D flow contains significant asymmetries in z of both Q2 and Q4 events at $t^+ = 13.5$, resulting in an asymmetric total stress. Specifically, positive vortices generate both stronger sweeps and ejections, or at least are more effective at generating Reynolds shear stress, than negative vortices. In addition, relative to the plane-averaged $\overline{u'v'}$ at this time, which is decreasing from the 2D level (Fig. 3), strong Q2 and Q4 events are actually stronger than those in the 2D flow, with the strongest events being associated with positive vortices. This suggests that, though there are fewer Reynolds-stress-producing events to contribute to the overall $-\overline{u'v'}$, a greater percentage of the events that do occur generate strong Reynolds shear stress. The positive mean spanwise shear apparently reinforces the effectiveness of positive vortices in generating strong Reynolds shear stress, as previously observed by Anderson and Eaton (1989). Visualization of the 3D flow (discussed below) suggests that this asymmetry in Reynolds shear stress generation is a consequence of the deformation of vortical structures.

Although some asymmetry in Q1 and Q3 events are discernible in Fig. 9, the asymmetry in the total Reynolds shear stress is dominated by the behavior of Q2 and Q4 events. This is in contrast to the findings of Kang et al. (1998), who found that the asymmetries in the total Reynolds-stress are only due to Q1 and Q3 events. However, their measurements were

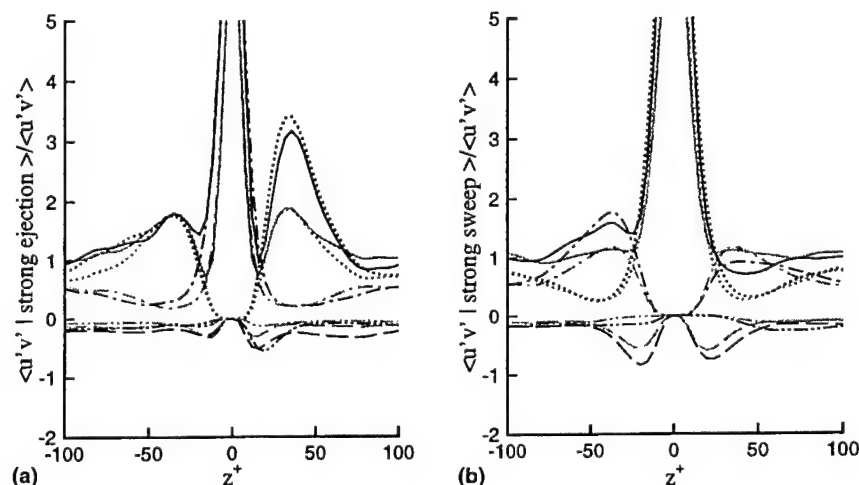


Fig. 9. Conditional average of $u'v'$ at $y^+ = 10$ in channel with spanwise moving wall, $t^+ = 13.5$: — total $\langle u'v' \rangle$; --- Q1; - · - · - Q2; · · · · · Q3; · · · · · Q4; shaded lines denote initial-condition contours: (a) strong ejection; (b) strong sweep.

taken at $y^+ \approx 90$, much further away from the wall than in the results plotted in Fig. 9. The 3DBL in their rotating disk experiment is also statistically stationary, rather than time-evolving as in the present study. For more direct comparisons we perform the same quadrant analysis on the Ekman layer of Coleman (1999), also a statistically stationary 3DBL with a similar spanwise mean velocity profile (Reynolds number for this flow is $Re \equiv U_\infty D/\nu = 1000$, where U_∞ is the magnitude of the freestream velocity, and $D^2 = \nu/\Omega$, with Ω being the rate of rotation about the wall-normal axis). Fig. 10 reveals that at $y^+ = 10$ the Reynolds shear stress possesses the asymmetries observed in the channel with a spanwise moving wall, while Fig. 11 shows only a slight asymmetry at $y^+ = 89$, which is still characterized by differences in the Q2 and Q4 peaks. Thus, the asymmetries observed in the total Reynolds shear stress (Figs. 9–11) come from Reynolds-stress-producing quadrants. Moreover, at the larger wall-normal distance, Reynolds shear stress is not typically associated with quasi-streamwise vortices, which exhibit the asymmetric behavior we observe, but with, for instance, the heads of hairpin vortices, which may respond differently to mean three-dimensionality.

3.3. Visualization

Finally, we visualize the vortical structures in the channel flow using isosurfaces of λ_2 . Fig. 12 shows an example for the 2D case. The vortices are oriented roughly in the streamwise direction, and arranged in an overlapping manner. Jeong et al. (1997), who performed a conditional average on the λ_2 distribution in a channel flow, described the alignment of the near-wall vortices as the alternating positive–negative pattern presented schematically in Fig. 16(a). Such clustering of vortical structures allows them to reinforce each other's induced flowfields, giving rise to streaks whose lengths are many times longer than the vortices themselves. Fig. 13, in which ω'_y contours represent the streak boundaries at $y^+ = 5$, clearly demonstrates this characteristic. Jeong et al. (1997) also showed that the average near-wall vortex is not aligned with the x -axis, but is slightly rotated in the x - z plane as shown in Fig. 16(a), and inclined in the wall-normal direction, so that the downstream head of the vortex is further away from the wall than the tail.

Fig. 14 displays the effect of the spanwise shear upon the vortical structures at $t^+ = 13.5$. Although the vortical struc-

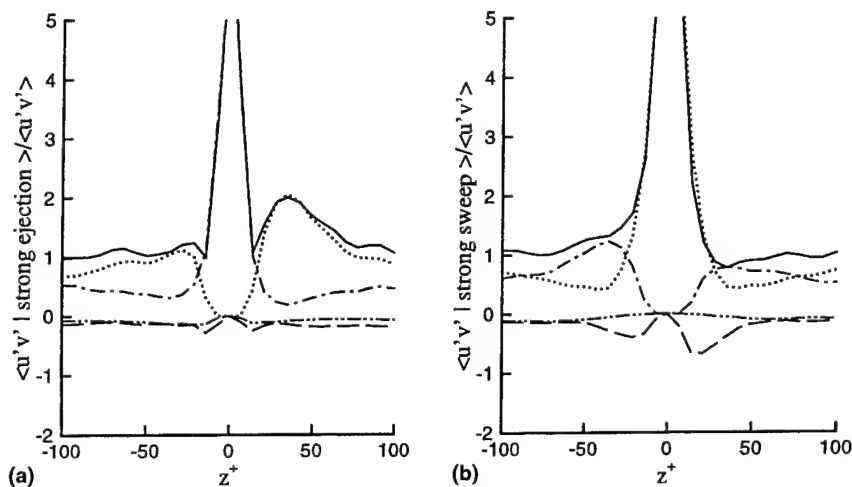


Fig. 10. Conditional average of $u'v'$ in Ekman layer at $y^+ = 10$; symbols same as in Fig. 9: (a) strong ejection; (b) strong sweep.

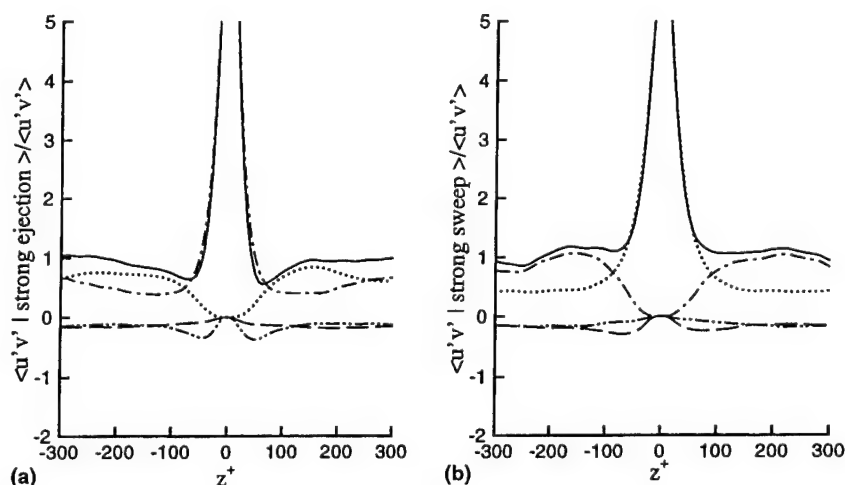


Fig. 11. Conditional average of $u'v'$ in Ekman layer at $y^+ = 89$; symbols same as in Fig. 9: (a) strong ejection; (b) strong sweep.

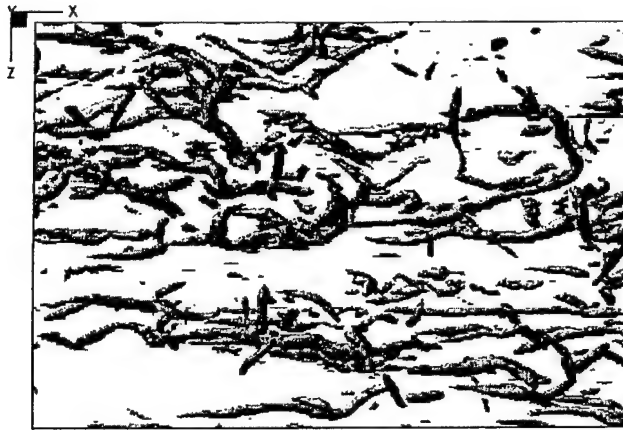


Fig. 12. Vortices in initial 2D channel ($t^+ = 0$): isosurfaces of $\lambda_2 = -0.012$, scaled with wall units.

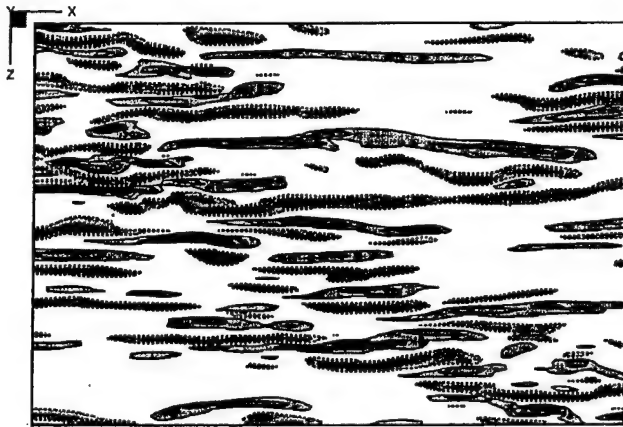


Fig. 13. Wall-normal vorticity in 2D channel ($t^+ = 0$) at $y^+ = 5$: — $\omega'_y > (\omega'_{y,0})_{rms}$; $\omega'_y < -(\omega'_{y,0})_{rms}$, where $(\omega'_{y,0})_{rms} \equiv (\overline{\omega'_y \omega'_y})^{1/2}$ in initial 2D flow; contour levels incremented by $(\omega'_{y,0})_{rms}$.

tures are not diminished to an appreciable degree at this time, the tails of the vortices, which are closer to the wall, move with the wall in the spanwise direction, while the heads retain their 2D orientation. This results in a change in the shapes of the vortices. Notice that many of the vortices in Fig. 14 appear to have more curvature than those in Fig. 12, and that the streaks shown in Fig. 15 appear to be breaking up into shorter structures that exhibit some degree of realignment in the new mean shear direction.

Based on the statistical and visualization results, we offer Fig. 16 as a model of the changes in vortical structures in a 3DBL. In contrast to the relatively symmetric structures shown in Fig. 16(a), positive vortices are now 'J-shaped', and negative vortices 'S-shaped'. Because the induced velocity on the concave side of a vortex line is greater than on the convex side, positive vortices create weaker sweeps than ejections, and negative vortices have weaker ejections than sweeps, resulting in the asymmetries observed in the velocity PDFs. Moreover, because the single-curvature of a positive vortex tends to focus its ejections more than the double-curvature of a negative vortex reinforces its sweeps, the Reynolds shear stress generated by positive vortices is stronger than that of negative vortices, which is manifest in the asymmetric distribution in the conditional-averaged quadrant analysis (Fig. 9). Another effect of the spanwise shear is to rotate the vortices away from their cooperative, overlapping alignment, resulting in the break-up of the nearwall streaks, as seen in Fig. 15.



Fig. 14. Vortices in channel with spanwise moving wall at $t^+ = 13.5$: symbols same as in Fig. 12. Wall motion is in negative z -direction.



Fig. 15. Wall-normal vorticity in channel with spanwise-moving wall at $y^+ = 5$ and $t^+ = 13.5$: symbols same as in Fig. 13. Wall motion is in negative z -direction.

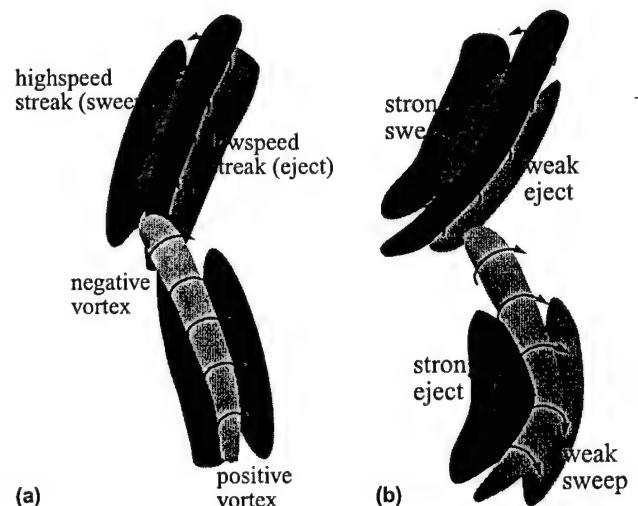


Fig. 16. Schematic of near-wall turbulence structures in (a) 2DBL and (b) 3DBL.

In the case of the 3D channel, the TKE, Reynolds shear stress and drag eventually recover as the near-wall structures realign themselves in the direction of the mean shear. Symmetry is restored in the Reynolds stress production, and the stress-strain lag angle returns to zero. In 3DBLs where mean three-dimensionality is maintained in a stationary state (such as the Ekman layer or the flow over a rotating disk), the lag angle remains finite and the efficiency of the flow in generating turbulence is generally reduced, as implied by the decrease in the stress/energy ratio often observed in these flows.

4. Summary and conclusions

DNS of a channel with a spanwise-moving wall has been used to examine the effects of mean three-dimensionality on near-wall turbulence structures that lead to reduced turbulence intensity and drag. PDFs and conditional-averaged quadrant analysis reveal that the three-dimensionality affects positive and negative vortices in different ways, thus destroying the spanwise symmetry of the turbulence structures. Visualizations show that the asymmetries arise due to temporary changes in the shapes of the vortical structures, and the reduction in streak size and strength are due to the alignment of the vortices being altered. The mean spanwise shear also increases the TKE dissipation by causing wall-normal layering of the streaks. These effects reduce the ability of the mean velocity gradient to sustain the turbulence, resulting in the reductions in TKE and drag characteristic of 3DBLs.

Acknowledgements

This work is supported by the Office of Naval Research (Grant No. N-00014-94-1-0016). Computing resources are provided by NASA-Ames Research Center and the National Partnership for Advanced Computational Infrastructure at the San Diego Supercomputer Center.

References

- Anderson, S.C., Eaton, J.K., 1989. Reynolds stress development in a pressure driven three-dimensional turbulent boundary layer. *Journal of Fluid Mechanics* 202, 263–294.
- Coleman, G.N., 1999. Similarity statistics from a direct numerical simulation of the neutrally stratified planetary boundary layer. *Journal of Atmospheric Sciences* 56, 891–900.
- Coleman, G.N., Kim, J., Le, A.-T., 1996. A numerical study of three-dimensional wall-bounded flows. *International Journal of Heat and Fluid Flow* 17, 333–342.
- Coleman, G.N., Kim, J., Spalart, P.R., 1997. Direct numerical simulation of decelerated wall-bounded shear flows. In: *Proceedings of the 11th Turbulent Shear Flows Conference*, Grenoble, France.
- Dhanak, M.R., Si, C., 1999. On reduction of turbulent wall friction through spanwise wall oscillations. *Journal of Fluid Mechanics* 383, 175–195.
- Jeong, J., Hussain, F., 1995. On the identification of a vortex. *Journal of Fluid Mechanics* 285, 69–94.
- Jeong, J., Hussain, F., Schoppa, W., Kim, J., 1997. Coherent structures near the wall in a turbulent channel flow. *Journal of Fluid Mechanics* 332, 185–214.
- Johnston, J.P., Flack, K.A., 1996. Review – advances in three-dimensional turbulent boundary layers with emphasis on the wall-layer regions. *Journal of Fluids Engineering* 118, 219–232.
- Kang, S.K., Choi, H., Yoo, J.Y., 1998. On the modification of the near-wall coherent structure in a three-dimensional turbulent boundary layer on a free rotating disk. *Physics of Fluids* 10, 2315–2322.
- Kim, J., Moin, P., Moser, R., 1987. Turbulence statistics in fully developed channel flow at low Reynolds number. *Journal of Fluid Mechanics* 177, 133–166.
- Littel, H.S., Eaton, J.K., 1994. Turbulence characteristics of the boundary layer on a rotating disk. *Journal of Fluid Mechanics* 266, 175–207.
- Sendstad, O., Moin, P., 1992. The near wall mechanics of 3D turbulent boundary layers. Report No. TF-57, Thermosciences Div., Dept. Mech. Engr., Stanford University, Stanford, CA.
- Shizawa, T., Eaton, J.K., 1990. Interaction of an embedded longitudinal vortex with an attached, 3D turbulent boundary layer. Report No. TF-56, Thermosciences Div., Dept. Mech. Engr., Stanford University, Stanford, CA.
- Tomkins, C.D., Adrian, R.J., Balachandar, S., 1998. The structure of vortex packets in wall turbulence. In: *Proceedings of the 29th Fluid Dynamics Conference*, Albuquerque, NM.

On the effects of nonequilibrium on the subgrid-scale stresses

Ugo Piomelli

Department of Mechanical Engineering, University of Maryland, College Park, Maryland 20742

Gary N. Coleman and John Kim

Department of Mechanical and Aerospace Engineering, University of California, Los Angeles, California 90095-1597

(Received 17 December 1996; accepted 17 April 1997)

An *a priori* study of the subgrid-scale (SGS) stresses and dissipation in two nonequilibrium, wall-bounded flows is carried out. The velocity fields were computed by direct simulations of two- and three-dimensional boundary layers obtained, respectively, by a sudden change in the Reynolds number and by an impulsive motion in the spanwise direction of the lower wall of a plane channel in fully developed turbulent flow conditions. Several realizations of the transient period of the flow were examined. The SGS stresses react to the imposition of the secondary shear more rapidly than the large-scale ones, and return to equilibrium before the resolved stresses do. In general, the subgrid scales are less sensitive than the large ones to the near-wall and nonequilibrium effects. Scale-similar and dynamic models appear well-suited to reproduce the correlation between resolved Reynolds stress production and events with significant production of SGS energy. © 1997 American Institute of Physics. [S1070-6631(97)01208-7]

I. INTRODUCTION

Large-eddy simulations (LES) of the Navier–Stokes equations are based on the assumption that the small, subgrid scales of motion are more universal than the large, energy-carrying ones, less affected by the boundary conditions, and, therefore, easier to model. Since in LES only the largest structures are computed, coarser grids can be used than in direct simulations, and higher Reynolds number flows can be studied at a fraction of the expense. Moreover, the modeling of the small scales in principle is simpler than the modeling of all the scales of motions required by Reynolds-averaged (RANS) calculations, and, therefore, better accuracy can be achieved, especially in three-dimensional flows for which most turbulence models (especially two-equation models) are known to be inadequate.

Since the small scales tend to be more homogeneous and isotropic than the large ones, simple models should be able to describe their physics fairly accurately. Furthermore, since the subgrid-scale (SGS) stresses are a small fraction of the total stresses, modeling errors should not affect the overall accuracy of the results as much as in the Reynolds-averaged turbulence modeling approach. For these reasons, most subgrid scale models in use presently are eddy-viscosity models that relate the subgrid-scale stresses, τ_{ij} , to the large-scale strain-rate tensor \bar{S}_{ij} . The eddy viscosity is given by the product of a length scale, ℓ , and a velocity scale, q_{sgs} . Since the most active unresolved scales are those closest to the cutoff, the natural length scale in LES modeling is the filter width, which is representative of the size of the smallest resolved structure in the flow, and is typically proportional to the grid size. The velocity scale is usually taken to be the square root of the trace of the SGS stress tensor, $q_{sgs}^2 = \tau_{kk}$. To determine q_{sgs}^2 in most cases the equilibrium assumption is exploited to obtain an algebraic model for the eddy viscosity.¹

The Smagorinsky model can be derived² based on the

observation that the small scales of motion have shorter time scales than the large, energy-carrying eddies; for this reason, it can be assumed that they adjust more rapidly than the large scales to perturbations, and recover equilibrium nearly instantaneously. Under this assumption, the transport equation for q_{sgs}^2 reduces to $-\tau_{ij}\bar{S}_{ij} = \epsilon_v$, where $-\tau_{ij}\bar{S}_{ij}$ is the production, and ϵ_v the viscous dissipation, of SGS energy. The negative of the production term, $\epsilon_{sgs} = \tau_{ij}\bar{S}_{ij}$, is often referred to as the “SGS dissipation,” since it also represents the dissipation of resolved energy by the SGS stresses. This balance, together with the definition of the eddy viscosity, can be used to obtain the velocity scale.

The equilibrium assumption implies inertial range dynamics: energy is generated at the large-scale level and transmitted to smaller and smaller scales, where the viscous dissipation takes place. Very little testing of the applicability of this assumption to the small scales of turbulence is available. It is well known that in most flows of interest the large scales are not in equilibrium: Smith and Yakhot³ studied the short-time behavior of the eddy viscosity in the Reynolds-averaged framework, and found that $\mathcal{K}-\epsilon$ models do not predict the correct response of the eddy viscosity if homogeneous isotropic turbulence is suddenly subjected to a perturbation (system rotation or shear, for instance). They conjecture that SGS models will suffer from the same shortcomings unless a short-time correction is applied. The fact that the Smagorinsky SGS model, applied to the study of homogeneous turbulence suddenly subjected to shear (Bardina *et al.*⁴) gave results in good agreement with the theory of Smith and Yakhot,³ however, indicates that the small scales tend to equilibrium faster than the large ones, and thus satisfy the equilibrium assumption better than the large scales do. This suggests that, at least in this flow, as long as the correct nonequilibrium response of the large scales is captured, the overall development may be predicted with satisfactory accuracy even by equilibrium-based SGS models. In more

complex flows, in which extra strains, backscatter, intermittency, and other phenomena play a role, it is not known whether the small scales would still be represented adequately by equilibrium-based subgrid-scale models.

The purpose of this paper is to study the physical behavior of the subgrid scales of motion in situations of strong perturbation from equilibrium by *a priori* testing. Two cases will be studied: The first is a fully developed plane channel flow in which the viscosity is suddenly decreased to accelerate the flow, which reaches equilibrium at a higher Reynolds number; the second, a three-dimensional, shear-driven boundary layer,⁵ obtained by moving the lower wall of a fully developed plane channel flow in the spanwise direction. Both flows are initially equilibrium flows that approach another equilibrium state, and thus allow comparison of the response of both large and subgrid scales to the perturbation, and their return to equilibrium.

Furthermore, the performance of several models will be compared. The models chosen are the Smagorinsky model,¹ the dynamic eddy-viscosity model,^{6,7} and two scale-similar models.^{8,9} Both the Smagorinsky and the dynamic model are eddy-viscosity models; the model coefficient in the former is set *a priori*, while in the latter it is adjusted according to the energy content of the simulation. Thus the dynamic model should be able to adjust more rapidly than the Smagorinsky model to the perturbations. Scale-similar models use the smallest resolved scales to parametrize the unresolved ones. They are based on the hypothesis that the most important interactions between resolved and unresolved scales occur between the eddies closest to the cutoff wave number. This dependence on the model on the smallest resolved scales will also be shown to have beneficial effects for the prediction of the response of the SGS stresses to perturbations.

In the next section the governing equations and the mathematical approach will be presented. The results of the *a priori* test will be presented in Sec. III. Some conclusions will be drawn in the last section.

II. PROBLEM FORMULATION

A. Governing equations

In LES dependent flow variables are divided into a grid-scale (GS) part and a subgrid-scale (SGS) part by the filtering operation

$$\bar{f}(\mathbf{x}) = \int_D f(\mathbf{x}') G(\mathbf{x}, \mathbf{x}') d\mathbf{x}', \quad (1)$$

where D is the computational domain, and G is the filter function. The application of this operation to the continuity and Navier–Stokes equations yields the equations that govern the evolution of the large, energy-carrying scales of motion:

$$\frac{\partial \bar{u}_i}{\partial t} + \frac{\partial}{\partial x_j} (\bar{u}_i \bar{u}_j) = -\frac{1}{\rho} \frac{\partial \bar{p}}{\partial x_i} - \frac{\partial \tau_{ij}}{\partial x_j} + \nu \frac{\partial^2 \bar{u}_i}{\partial x_j \partial x_j}, \quad (2)$$

$$\frac{\partial \bar{u}_i}{\partial x_i} = 0, \quad (3)$$

where x (or x_1) is the streamwise direction, y (or x_2) the wall-normal direction, and z (or x_3) the spanwise direction; u , v , and w (or u_1 , u_2 , and u_3) are the velocity components in the coordinate directions. The effect of the small scales appears in the SGS stress term, $\tau_{ij} = \overline{u_i u_j} - \bar{u}_i \bar{u}_j$, which must be modeled.

B. Subgrid-scale stress models

In the past, two main types of models have been used to parametrize the SGS stresses: eddy viscosity and scale-similar models. Eddy-viscosity models represent the anisotropic part of the SGS stress tensor as

$$\tau_{ij} - \frac{\delta_{ij}}{3} \tau_{kk} = -2\nu_T \bar{S}_{ij}, \quad (4)$$

where ν_T is the eddy viscosity and \bar{S}_{ij} is the large-scale strain rate tensor

$$\bar{S}_{ij} = \frac{1}{2} \left(\frac{\partial \bar{u}_i}{\partial x_j} + \frac{\partial \bar{u}_j}{\partial x_i} \right). \quad (5)$$

The assumption that $-\tau_{ij} \bar{S}_{ij} = \epsilon_v$, where

$$\epsilon_v = \left(\frac{\partial \bar{u}_i}{\partial x_j} \frac{\partial \bar{u}_i}{\partial x_j} - \frac{\partial \bar{u}_i}{\partial x_j} \frac{\partial \bar{u}_j}{\partial x_i} \right), \quad (6)$$

allows the eddy viscosity to be written as¹

$$\nu_T = (C_S \Delta)^2 |\bar{S}|, \quad (7)$$

where $|\bar{S}| = (2 \bar{S}_{ij} \bar{S}_{ij})^{1/2}$, Δ is the (grid-scale) filter width, and the Smagorinsky constant, C_S , can be determined by integrating the vorticity spectrum function over all the unresolved wave numbers.² In practice, the value of the constant is substantially reduced in the presence of shear, and van Driest¹⁰ damping is used to account for near-wall effects; the eddy viscosity thus becomes

$$\nu_T = [C_S \Delta (1 - e^{-y^+/25})]^2 |\bar{S}|, \quad (8)$$

where $y^+ = y_w u_\tau / \nu$, y_w is the distance from the wall, and $C_S \approx 0.065 - 0.1$.

Recently, dynamic models have been introduced that adjust the coefficient locally and instantaneously from the energy content of the smallest resolved scales.⁶ These are generally Smagorinsky-like models in which the coefficient C is determined based on the energy content of the smallest resolved scales of motion. In this work, the plane-averaged formulation,⁷ which has been applied successfully to the simulation of transitional and turbulent plane channel flows^{6,11} will be used, in which the SGS stresses are given by (4), with $\nu_T = C \Delta^2 |\bar{S}|$, and

$$C = -\frac{1}{2} \frac{\langle \mathcal{L}_{ij} M_{ij} \rangle}{\langle M_{mn} M_{mn} \rangle}, \quad (9)$$

where $\langle \cdot \rangle$ denotes an average taken over planes parallel to the wall, $\mathcal{L}_{ij} = \widehat{u_i u_j} - \hat{u}_i \hat{u}_j$ are the resolved turbulent stresses, $M_{ij} = \Delta^2 |\hat{S}| \hat{S}_{ij} - \Delta^2 |\bar{S}| \bar{S}_{ij}$, and a hat denotes the application of a filter with width $\hat{\Delta} = 2\Delta$.

Scale similar models also use the energy content of the smallest resolved scales of motion to predict the behavior of the SGS stresses. In this work, two such models will be tested, the one originally developed by Bardina *et al.*:⁸

$$\tau_{ij} = \overline{\overline{u_i u_j}} - \overline{\overline{u_i}} \overline{\overline{u_j}} \quad (10)$$

and the one recently proposed by Liu *et al.*:⁹

$$\tau_{ij} = C_L \mathcal{L}_{ij}; \quad (11)$$

Liu *et al.*⁹ recommended a value $C_L = 0.45$. The coefficient can also be adjusted dynamically.

C. A priori tests

In *a priori* tests the resolved velocity fields obtained from direct simulations of the Navier–Stokes equations are filtered explicitly according to (1) to yield the exact SGS quantities of interest. Two filter functions are considered in this study: the sharp cutoff filter in Fourier space and the box (or tophat) filter in physical space. The sharp cutoff filter is best defined in Fourier space as:

$$g(k) = \int_D G(x') e^{-ikx'} dx' = \begin{cases} 1, & \text{if } k \leq \pi/\Delta, \\ 0, & \text{otherwise,} \end{cases} \quad (12)$$

while the box (or top hat) filter is

$$G(x) = \begin{cases} 1/\Delta, & \text{if } |x| \leq \Delta/2, \\ 0, & \text{otherwise.} \end{cases} \quad (13)$$

Three DNS databases were used in this work: the first is the DNS of a two-dimensional plane channel flow at $Re_\tau = 180$ (based on friction velocity u_τ and channel half-width δ), computed using a pseudo-spectral code with $128 \times 97 \times 128$ grid points and a computational domain of $4\pi\delta \times 2\delta \times 4\pi\delta/3$. The results of this calculation were shown by Piomelli *et al.*¹² to be in good agreement with the direct numerical simulations (DNS) of Kim *et al.*¹³ The accelerating channel case was computed using the same pseudo-spectral code; the flow was started from a steady-state field at $Re_\tau = 150$ (based on the initial friction velocity $u_{\tau,0}$ and viscosity ν_0); the Reynolds number was then suddenly increased, and a new equilibrium state was reached at $Re_\tau = 225$ at $tu_{\tau,0}/\delta \approx 1.2$.

The shear-driven three-dimensional boundary layer velocity fields were obtained from the calculations by Coleman *et al.*⁵ using the spectral code of Kim *et al.*¹³ The computational domain was $4\pi\delta \times 2\delta \times 8\pi\delta/3$ in the streamwise (x_1 or x), wall-normal (x_2 or y), and spanwise (x_3 or z) directions, respectively, and $256 \times 129 \times 256$ grid points were used. An impulsive spanwise motion, with magnitude equal to 47% of the initial mean centerline velocity, was applied to the lower wall of a fully developed plane channel flow; the initial condition was obtained from the calculation at Reynolds number $Re_\tau = 180$. The flow was allowed to develop until a collateral state (one in which the new direction of the mean velocity is the same at each y) was reached. Notice that, since periodic boundary conditions were used, the boundary layer due to the spanwise motion of the wall grows in time rather than in space.

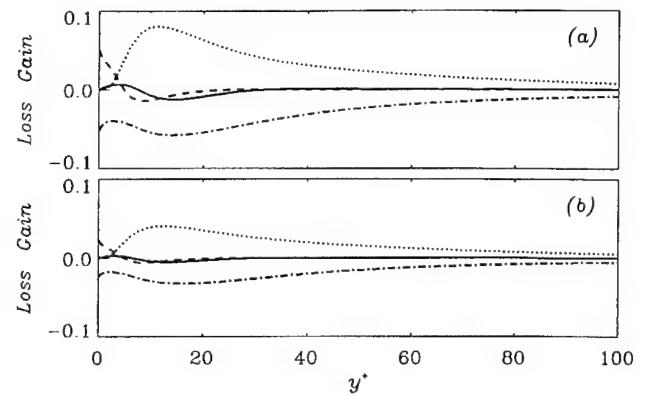


FIG. 1. Terms in the SGS kinetic budget in the two-dimensional plane channel flow, $Re_\tau = 180$, normalized by u_τ and ν . Tophat filter. \cdots , production; $---$, viscous dissipation; $---$, viscous diffusion; $---$, remaining terms. (a) $\Delta_i = 4\Delta x_i$; (b) $\Delta_i = 2\Delta x_i$.

The exact GS and SGS fields were obtained by filtering the DNS data over the streamwise and spanwise homogeneous directions using different filter types and sizes. A typical test performed using the Fourier cutoff filter employs a filter width $\Delta_i = 4\Delta x_i$ (for $i = 1$ and 3); for the box filter widths $\Delta_i = 2\Delta x_i$ and $\Delta_i = 4\Delta x_i$ were used. With these values, the ratio of SGS to total fluctuating energy was 15%–25%, a range representative of actual LES calculations. No significant difference was observed between the results for the two filters.

All the data shown in the following were averaged over several realizations of the flow fields in question, as well as over planes parallel to the wall. Since the expense required to generate ensembles of data in this type of unsteady flows is significant, the sample size in some cases is insufficient to obtain fully converged results. However, the purpose of the *a priori* test is only to supply physical insight into the phenomena that affect the subgrid scales and identify the trends; for this purpose, the sample size is adequate.

Two normalizations will be used: one in which all quantities are made dimensionless using the initial friction velocity $u_{\tau,0}$ and molecular viscosity ν_0 . In the other the time-dependent values of the friction velocity u_τ and viscosity ν are used. Quantities made dimensionless by the latter normalizations will be denoted by a prime.

III. RESULTS AND DISCUSSION

A. Plane channel flow

In Fig. 1 the terms in the budget of the SGS kinetic energy $\mathcal{K}_{sgs} = \tau_{kk}/2$ are shown for the two-dimensional plane channel flow as a function of y^+ . The assumption that production and dissipation of SGS energy are in balance holds well outside the viscous sublayer ($y^+ > 30$), and only very near the wall are nonlocal effects important. This is consistent with the finding that, in the core of the flow, dynamic eddy-viscosity models yield a value for the model coefficient close to that obtained using the equilibrium assumption and a Kolmogorov form of the spectrum.¹¹ It should also be pointed out that in the budget for the total

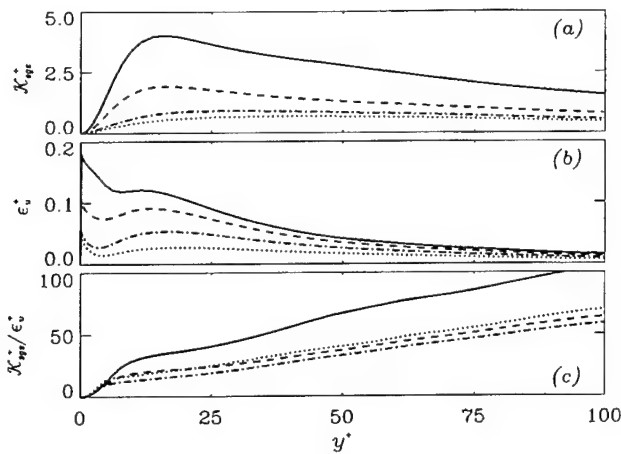


FIG. 2. SGS kinetic energy, viscous dissipation, and eddy turnover time in the two-dimensional plane channel flow, $Re_\tau = 180$, normalized by u_τ and ν . Fourier cutoff filter. —, $\Delta_i \rightarrow \infty$; ---, $\Delta_i = 8\Delta x_i$; - · - · -, $\Delta_i = 4\Delta x_i$; · · · · ·, $\Delta_i = 2\Delta x_i$. (a) SGS kinetic energy; (b) viscous dissipation; (c) $\mathcal{K}_{sgs}^+/\epsilon_v^+$.

kinetic energy, at this Reynolds number, production and dissipation are not in balance near the wall, where the various diffusion terms are significant;¹⁴ in the outer region the turbulent transport term is not negligible. Only at much higher Reynolds number does behavior like that observed here for the SGS energy become apparent. This point further supports the equilibrium assumption for the small scales.

When homogeneous turbulence is suddenly subjected to mean shear, its short-time response is characterized by a lag between the imposition of the strain and the increase in turbulent kinetic energy due to the increased production. Smith and Yakhot³ accounted for the lag, within the framework of $\mathcal{K}-\epsilon$ models, by introducing an exponential correction to the eddy viscosity, which includes a time constant, the eddy turnover time $\tau \sim \mathcal{K}/\epsilon$. In the context of LES, in which the SGS model only represents the scales smaller than the filter width, a relevant eddy turnover time must be defined in terms of SGS quantities only, and could depend on the filter width. In Fig. 2 such an eddy turnover time, defined in terms of \mathcal{K}_{sgs} and ϵ_v is shown as a function of distance from the wall for the two-dimensional channel; the Fourier cutoff filter was used. The plane-averaged values ($\Delta_i \rightarrow \infty$) are equivalent to long-time averages and thus represent the eddy turnover time relevant to $\mathcal{K}-\epsilon$ models. Both SGS energy and viscous dissipation decrease as the filter width is decreased; the SGS turnover time is, however, fairly independent of the filter width, and, except very near the wall, is equal to about 50%–60% of the Reynolds-averaged turnover time. While the subgrid scales can be expected to react more rapidly than the largest scales of motion, their response to a perturbation is not instantaneous. Accounting for this adjustment time could improve significantly the accuracy of SGS stress models.

B. Accelerating channel flow

In the accelerating channel flow the perturbation that disrupts the equilibrium state consists of a sudden increase of

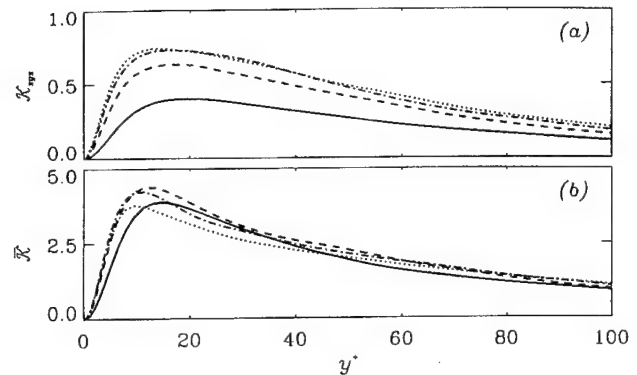


FIG. 3. SGS and large-scale energy, normalized by $u_{\tau,0}$. Accelerating channel flow, top hat filter, $\Delta_i = 2\Delta x_i$. —, $tu_{\tau,0}/\delta = 0.06$; ---, $tu_{\tau,0}/\delta = 0.32$; - · - · -, $tu_{\tau,0}/\delta = 0.52$; · · · · ·, $tu_{\tau,0}/\delta = 0.70$. (a) SGS energy; (b) large-scale energy.

the Reynolds number. Consequently, one would expect the high-wave-number region of the velocity spectra to fill up, and the small scales should be affected more than the large ones by the perturbation.

In Fig. 3 large-scale and SGS kinetic energy profiles are shown at various times during the transient. While the maximum total kinetic energy, $\mathcal{K} + \mathcal{K}_{sgs}$ increases only by 25%, the subgrid-scale energy increases by more than a factor of 2. Similarly, the production of SGS energy (not shown) increases roughly by a factor of 3 during the transient, while the production of large-scale energy at the last time examined ($tu_{\tau,0}/\delta = 0.58$) is only 30% higher than before the perturbation was applied.

If the time-dependent value of the friction velocity is used to normalize the data instead of the initial one, a different trend is observed: the SGS turbulent kinetic energy (Fig. 4) quickly reaches a new equilibrium value (roughly at $tu_{\tau,0}/\delta \approx 0.3$) and is thereafter nearly independent of time, while the large-scale quantity requires a much longer time to reach a new equilibrium state. This is another strong indication that the small scales tend to adapt to the perturbation much faster than the large scales do, since the former react to

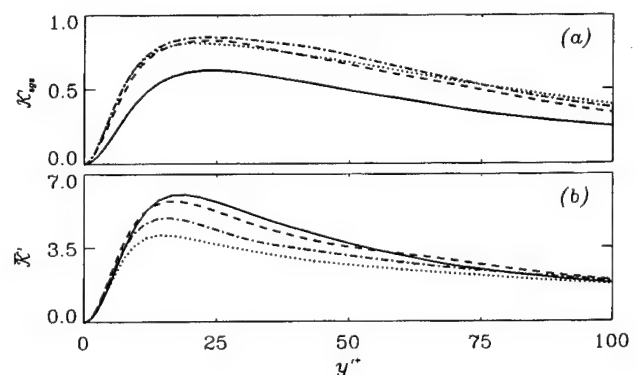


FIG. 4. SGS and large-scale energy normalized by u_τ . Accelerating channel flow, top hat filter, $\Delta_i = 2\Delta x_i$. —, $tu_{\tau,0}/\delta = 0.06$; ---, $tu_{\tau,0}/\delta = 0.32$; - · - · -, $tu_{\tau,0}/\delta = 0.52$; · · · · ·, $tu_{\tau,0}/\delta = 0.70$. (a) SGS energy; (b) large-scale energy.

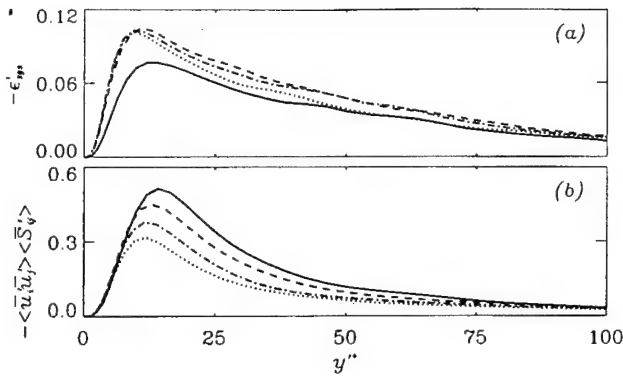


FIG. 5. Production of SGS and large-scale energy, normalized by u_τ and ν . Accelerating channel flow, tophat filter, $\Delta_f = 2\Delta x_i$. —, $tu_{\tau,0}/\delta = 0.06$; ---, $tu_{\tau,0}/\delta = 0.32$; - · - · -, $tu_{\tau,0}/\delta = 0.52$; · · · ·, $tu_{\tau,0}/\delta = 0.70$. (a) Production of SGS energy; (b) production of large-scale energy.

the “current state” (represented by the time-dependent velocity scale u_τ) fairly rapidly, whereas the large scales adapt more slowly. The production of SGS and large-scale energy also exhibit a similar trend (Fig. 5).

One of the main purposes of SGS models is to dissipate the correct overall amount of energy from the resolved scales. The total energy drain is the negative of the integral, over the wall-normal direction, of the (time- and plane-averaged) production of SGS energy. The time development of this quantity, together with the integral of the large-scale production, is shown in Fig. 6(b); in Fig. 6(a) the integral of the large-scale and SGS energy is shown. Under the time-dependent normalization (u_τ and ν) the subgrid-scale production and energy do not vary as much as when they are normalized by the initial u_τ and ν , indicating that they are better described by the local state of the turbulence; by contrast, the large-scale quantities vary less when normalized by the initial friction velocity and viscosity.

In Fig. 7 profiles of $-\epsilon_{sgs}$ are compared with those ob-

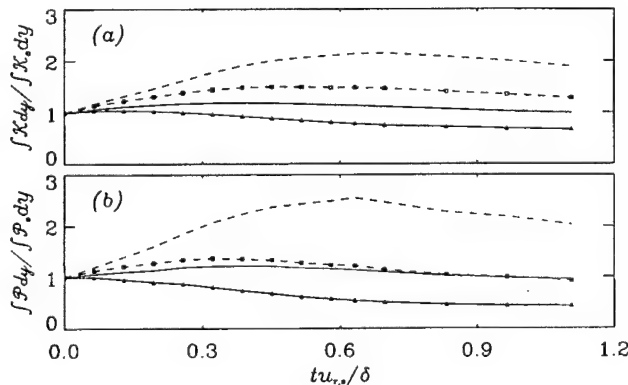


FIG. 6. Time development of the integral of the large-scale and SGS quantities normalized by their initial values. Accelerating channel flow. Tophat filter, $\Delta_f = 2\Delta x_i$. Lines without symbols: quantities normalized by $u_{\tau,0}$ and ν_0 ; lines with symbols: quantities normalized by u_τ and ν . (a) —, Large-scale energy; ---, SGS energy. (b) —, Production of large-scale energy; ---, production of SGS energy.

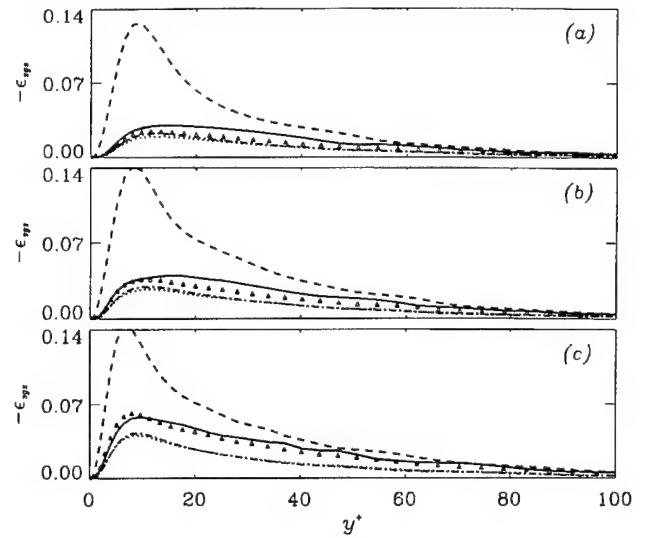


FIG. 7. Wall-normal distribution of the exact and modeled production of SGS energy, normalized by $u_{\tau,0}$ and ν_0 . Accelerating channel flow. Tophat filter, $\Delta_f = 2\Delta x_i$. Δ Exact; —, dynamic eddy viscosity model;^{6,7} ---, Smagorinsky model¹ [Eq. (8)]; - · - · -, scale similar model;⁹ · · · ·, scale similar model.⁸ (a) $tu_{\tau,0}/\delta = 0$; (b) $tu_{\tau,0}/\delta = 0.13$; (c) $tu_{\tau,0}/\delta = 0.32$.

tained from several models. The Smagorinsky model not only provides excessive levels of the production throughout the channel, but also does not predict accurately the increase in production that follows the imposition of the perturbation. The time development of the production of SGS energy integrated over the channel height is shown Fig. 8; the integral normalized by its initial value [Fig. 8(a)] indicates that the scale-similar models^{8,9} and the dynamic model^{6,7} follow the trend more closely. The unnormalized values [shown in Fig. 8(b)] indicate that the scale-similar models tend to underpredict the production of SGS energy, consistent with the findings of Bardina *et al.*,⁸ who developed the mixed model, which includes a dissipative as well as a scale-similar part, to overcome this shortcoming.

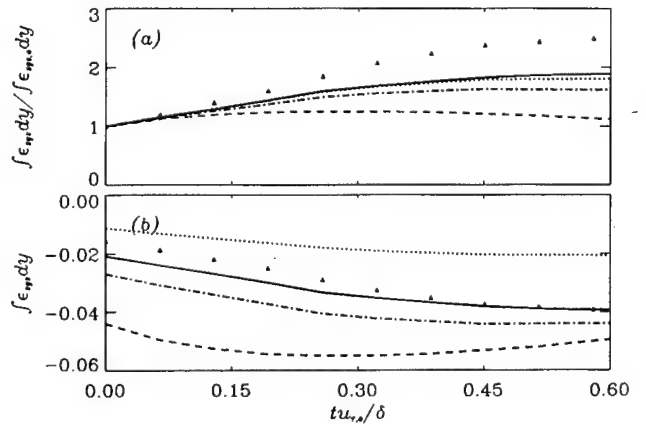


FIG. 8. Time development of the integral of the production of SGS energy. Accelerating channel flow. Tophat filter; $\Delta_f = 2\Delta x_i$. Δ Exact; —, dynamic eddy viscosity model;^{6,7} ---, Smagorinsky model¹ [Eq. (8)]; - · - · -, scale similar model;⁹ · · · ·, scale similar model.⁸ (a) Normalized by its initial value; (b) unnormalized.

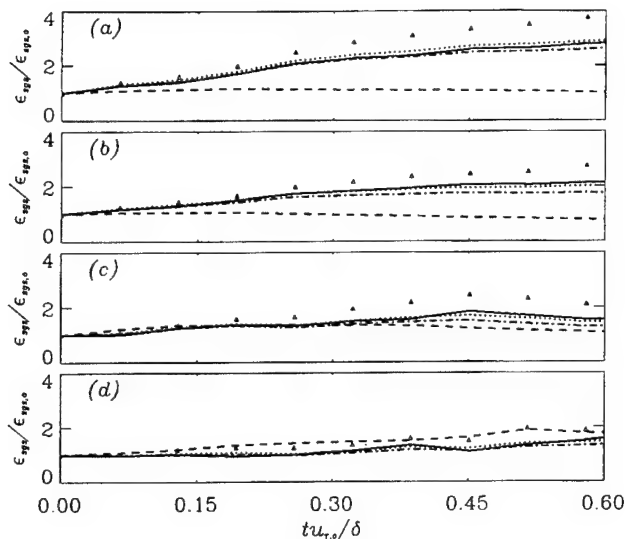


FIG. 9. Time development of exact and modeled production of SGS energy. Accelerating channel flow. Tophat filter, $\Delta_i = 2\Delta x_i$. All quantities are normalized by $u_{\tau,0}$ and ν , and their initial value. \triangle Exact; —, dynamic eddy viscosity model;^{6,7} - - -, Smagorinsky model¹ [Eq. (8)]; ·····, scale similar model;⁹ ·····, scale similar model.⁸ (a) $y^+ = 8$; (b) $y^+ = 13$; (c) $y^+ = 31$; (d) $y^+ = 110$.

The increased production predicted by the Smagorinsky model is particularly significant in the near-wall layer, where the scale-similar and dynamic models predict the response to the perturbation fairly accurately (Fig. 9). In the buffer layer and above the perturbation does not appear to have such a strong effect.

The principal shortcoming of eddy-viscosity models is the fact that the time scale, $|\bar{S}|^{-1}$, is mostly affected by the

large scales; thus they do not, in general, respond well to perturbations that affect mostly the small scales. This is the reason for the poor performance of the Smagorinsky model in this flow. The dynamic eddy-viscosity model appears to compensate for this deficiency by adjusting the model coefficient according to the state of the smallest resolved scales; the scale-similar models have a similar behavior. This is evidenced in Fig. 10, in which the development of the kinetic energy spectrum at $y^+ = 13$ is shown. The increase in energy at the high wave numbers is apparent. The scales that contribute most to the resolved turbulent stresses \mathcal{L}_{ij} (to a first approximation, the wave numbers contained between the two ellipses in the figure) also increase significantly during the transient, more so than the largest scales of motion (the contours near the origin), which remain essentially unchanged. Thus it appears that the double filtering operation employed by both dynamic and scale-similar models is beneficial in isolating the scales that most closely represent the smallest scales of motion.

C. Three-dimensional boundary layer

Similar results were obtained from the three-dimensional boundary layer simulation. In this flow the perturbation is applied more gradually, and is also localized in space (at the wall), while the Reynolds number change of the previous flow is felt everywhere. The SGS energy (Fig. 11) can be observed to react more quickly to the imposition of the perturbation than the large-scale energy (especially near the wall), but the phenomenon is not as clear as in the preceding case, due to the local nature of the perturbation.

The more accurate predictions obtained by the dynamic and scale-similar models are evidenced in Figs. 12 and Figs.

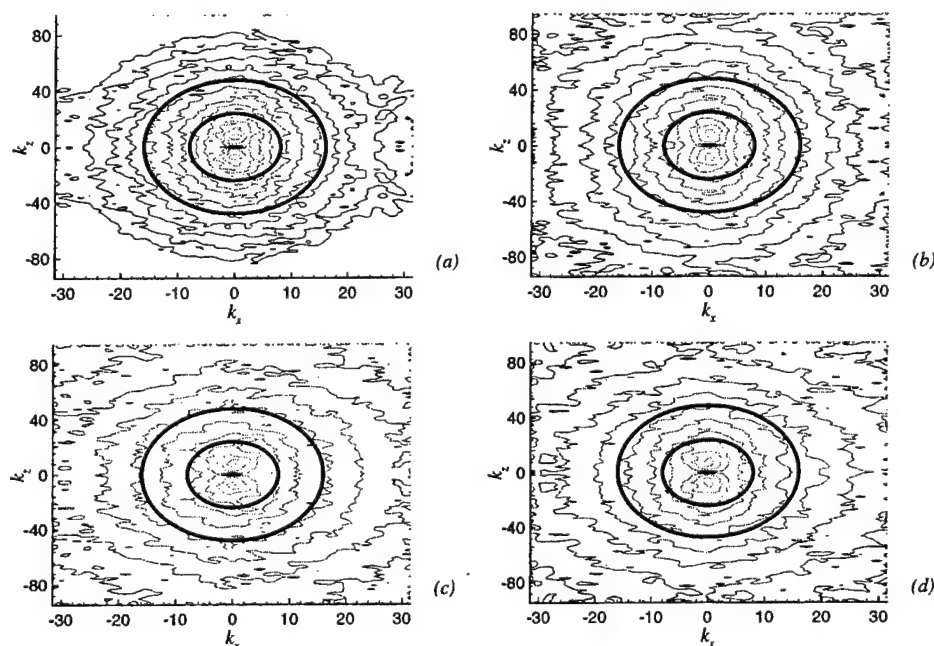


FIG. 10. Kinetic energy spectra (normalized by $u_{\tau,0}$) at $y^+ = 13$. Accelerating channel flow. The contour levels are exponentially spaced between 10^{-7} (black) and 10^0 (grey); the two ellipses roughly correspond to the grid- and test-filter wave numbers. (a) $tu_{\tau,0}/\delta = 0$; (b) $tu_{\tau,0}/\delta = 0.13$; (c) $tu_{\tau,0}/\delta = 0.32$; (d) $tu_{\tau,0}/\delta = 0.58$.

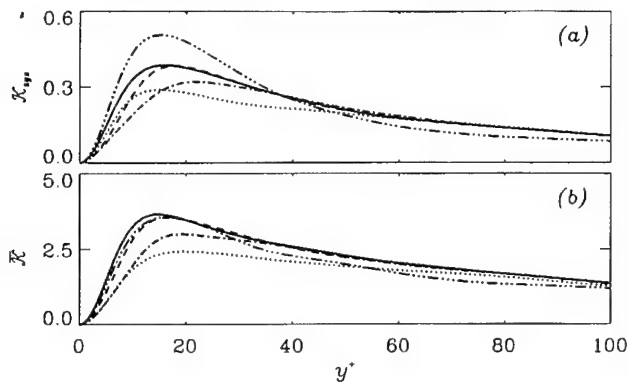


FIG. 11. SGS and large-scale energy, normalized by $u_{\tau,o}$. Three-dimensional boundary layer. Tophat filter, $\Delta_i = 2\Delta x_i$. —, $tu_{\tau,o}/\delta = 0$; ---, $tu_{\tau,o}/\delta = 0.075$; - · - · -, $tu_{\tau,o}/\delta = 0.15$; · · · · ·, $tu_{\tau,o}/\delta = 0.30$; — · — · —, $tu_{\tau,o}/\delta = 0.75$. (a) SGS energy; (b) large-scale energy.

13, in which, respectively, the integrated production of SGS energy, $-\varepsilon_{sgs}$, and its development at several wall-normal locations are shown. The Smagorinsky model initially predicts increased production in the near-wall region (instead of the reduced dissipation that is observed in the DNS data), reflecting the imposition of the transverse shear $\partial W/\partial y$, which gives an increase in the eddy viscosity. The other models follow the correct trend, because the smallest resolved scales are used to evaluate the coefficient. This is confirmed by the kinetic energy spectra (Fig. 14), which show features similar to those observed in the accelerating channel flow. The scales included between the two filters behave in a manner very similar to the unresolved scales.

Another useful feature of scale-similar models is that they parametrize the unresolved scales in terms of the smallest resolved ones, which have been shown^{15–17} to be responsible for most of the energy transfer between resolved and unresolved scales. Piomelli and co-workers¹² observed significant correlation between regions of high Reynolds stress and production of SGS energy. This correlation can be observed in the present data as well. Figure 15 compares contours of total production and production of SGS energy. A strong correlation can be observed between the exact

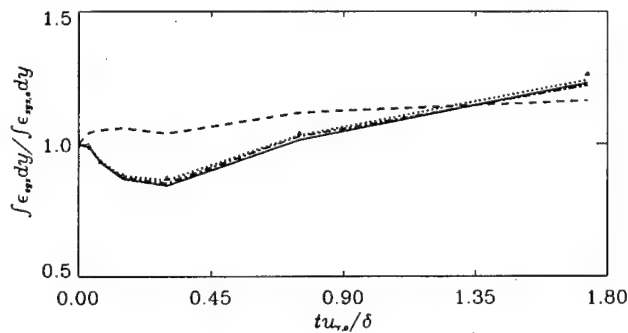


FIG. 12. Time development of the integral of the production of SGS energy. Three-dimensional boundary layer. Tophat filter, $\Delta_i = 2\Delta x_i$. All quantities are normalized by $u_{\tau,o}$ and ν , and their initial value. Δ Exact; —, dynamic eddy viscosity model;^{6,7} ---, Smagorinsky model¹ [Eq. (8)]; - · - · -, scale similar model;⁹ · · · · ·, scale similar model.⁸

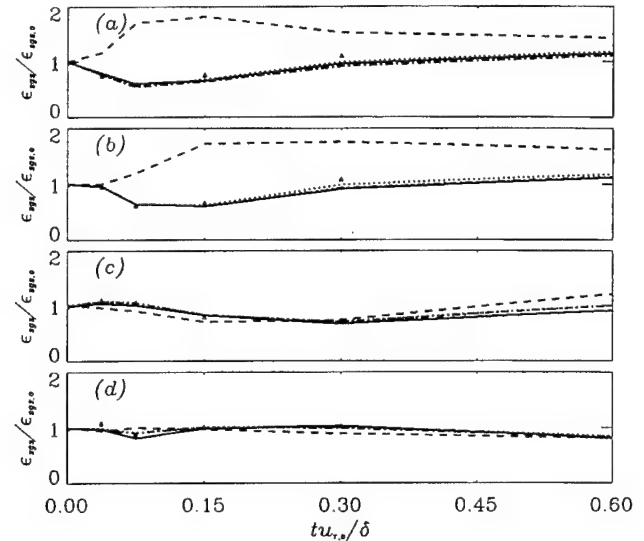


FIG. 13. Time development of exact and modeled production of SGS energy. Three-dimensional boundary layer. Tophat filter, $\Delta_i = 2\Delta x_i$. All quantities are normalized by $u_{\tau,o}$ and ν , and their initial value. Δ Exact; —, dynamic eddy viscosity model;^{6,7} ---, Smagorinsky model¹ [Eq. (8)]; - · - · -, scale similar model;⁹ · · · · ·, scale similar model.⁸ (a) $y^+ = 8$; (b) $y^+ = 13$; (c) $y^+ = 31$; (d) $y^+ = 110$.

$-\varepsilon_{sgs}$ and the total production; this correlation is reproduced well by the scale-similar model, but less accurately by the eddy viscosity model, which, being statistical in nature, cannot be expected to be as successful in reproducing deterministic events of the type responsible for the distribution of $-\varepsilon_{sgs}$.

IV. CONCLUSIONS

The velocity fields obtained from the direct simulation of two nonequilibrium flows, an accelerating channel flow and a three-dimensional boundary layer, were studied to determine the response to perturbations of the subgrid scales of motion, and their return to equilibrium.

The subgrid scales have a reduced turnover time compared with the resolved scales of motion. The fact that this time-scale is not a small fraction of the large-eddy turnover time is partly due to the low Reynolds number of the DNS data used in the present *a priori* study; in such situations, the strongest interactions between resolved and unresolved scales occur between structures within two octaves of the cutoff wave number. At high Reynolds numbers, when widely separated scales are present, this local interaction may be less dominant, but is still expected to be relevant.

In both flows under consideration, equilibrium turbulence is perturbed, and a new equilibrium is reached. In both cases the subgrid scales reach the new equilibrium substantially faster than the large, resolved, ones. However, the return to equilibrium of the subgrid scales requires a finite time and is not instantaneous.

From a modeling point of view, this result indicates that SGS models would benefit from incorporating nonequilibrium behavior to predict more accurately engineering flows, in which a variety of effects (pressure gradients, secondary shear, etc.) may act to perturb the canonical flows. An effi-

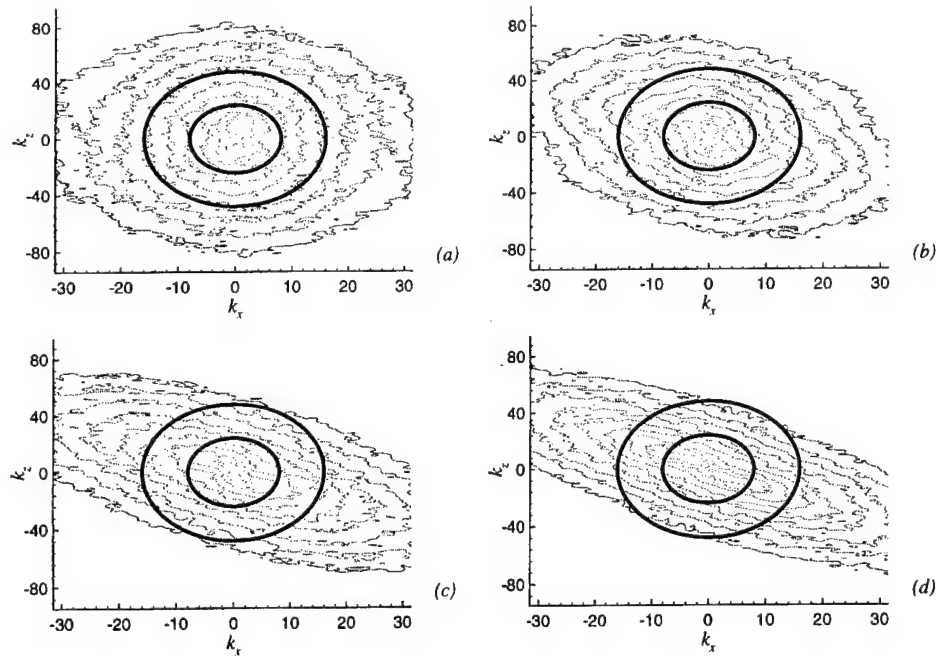


FIG. 14. Kinetic energy spectra (normalized by u_τ) at $y^+ = 15$. Three-dimensional boundary layer. The contour levels are exponentially spaced between 10^{-7} (black) and 10^0 (grey); the two ellipses roughly correspond to the grid- and test-filter wave numbers. (a) $tu_{\tau,o}/\delta = 0$; (b) $tu_{\tau,o}/\delta = 0.14$; (c) $tu_{\tau,o}/\delta = 0.29$; (d) $tu_{\tau,o}/\delta = 0.60$.

cient and inexpensive way to take those effects into account is to use the smallest resolved scales to parametrize the unresolved ones, as is done in scale-similar and dynamic models. These models have been found to respond more accurately to perturbations than models, like the Smagorinsky model, that are mostly affected by the largest scales of mo-

tion. The present results further confirm the robustness of dynamic SGS models in computing nonequilibrium flows.

While the dynamic eddy viscosity model predicts the overall levels of energy drained from the large scales quite accurately, scale-similar models are much more effective at representing the correlation between the production of large-

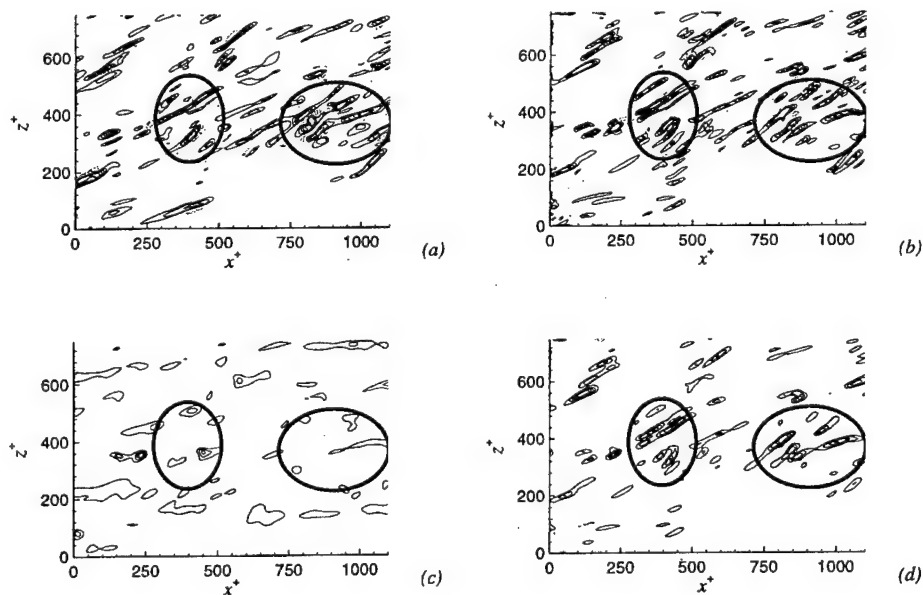


FIG. 15. Spatial distribution of the large-scale and SGS energy production on the $y^+ = 12$ plane at $tu_{\tau,o}/\delta = 0.3$. Three-dimensional boundary layer. Tophat filter, $\Delta_i = 2\Delta x_i$. All quantities are normalized by $u_{\tau,o}$ and ν . Positive contours are grey, negative are black. (a) Total production, $u'_i u'_j (\partial U_i / \partial x_j)$; contour level intervals are ± 0.8 . (b) Production of SGS energy (exact); contour level intervals are ± 0.06 . (c) Production of SGS energy (dynamic eddy-viscosity model^{6,7}); contour level intervals are ± 0.06 . (d) Production of SGS energy (scale similar model⁹); contour level intervals are ± 0.06 . The ellipses highlight regions of significant production.

scale energy and production of SGS energy that has been observed in these nonequilibrium flows, and also in the near-wall region of equilibrium boundary layers.¹² Mixed models, which combine a scale-similar model with a dissipative, eddy-viscosity term, are likely to be very effective parametrizations of the SGS stresses in nonequilibrium flows.

ACKNOWLEDGMENTS

Support for this research was provided by the Office of Naval Research, Grants No. N00014-91-J-1638 (UP) and No. N0014-94-1-0016 (GNC and JK) monitored by Dr. L. Patrick Purtell. Computer time was provided by the Naval Oceanographic Office, the NAS program at NASA-Ames Research Center, and the San Diego Supercomputer Center.

- ¹J. Smagorinsky, "General circulation experiments with the primitive equations. I. The basic experiment," *Mon. Weather Rev.* **91**, 99 (1963).
- ²D. K. Lilly, "The representation of small-scale turbulence in numerical simulation experiments," *Proceedings of the IBM Scientific Computing Symposium on Environmental Sciences*, Yorktown Heights, NY (unpublished).
- ³L. M. Smith and V. Yakhot, "Short and long-time behavior of eddy viscosity models," *Theor. Comput. Fluid Dyn.* **4**, 197 (1993).
- ⁴J. Bardina, J. H. Ferziger, and R. S. Rogallo, "Effect of rotation on isotropic turbulence: Computation and modelling," *J. Fluid Mech.* **154**, 321 (1985).
- ⁵G. N. Coleman, J. Kim, and A.-T. Le, "A numerical study of three-

- dimensional boundary layers," *Proceedings of the 10th Turbulent Shear Flow Conference*, State College, PA, 1995 (unpublished).
- ⁶M. Germano, U. Piomelli, P. Moin, and W. H. Cabot, "A dynamic subgrid-scale eddy viscosity model," *Phys. Fluids A* **3**, 1760 (1991).
- ⁷D. K. Lilly, "A proposed modification of the Germano subgrid-scale closure method," *Phys. Fluids A* **4**, 633 (1992).
- ⁸J. Bardina, J. H. Ferziger, and W. C. Reynolds, "Improved subgrid scale models for large eddy simulation," AIAA Paper No. 80-1357, 1980.
- ⁹S. Liu, C. Meneveau, and J. Katz, "On the properties of similarity subgrid-scale models as deduced from measurements in a turbulent jet," *J. Fluid Mech.* **275**, 83 (1994).
- ¹⁰E. R. Van Driest, "On the turbulent flow near a wall," *J. Aero. Sci.* **23**, 1007 (1956).
- ¹¹U. Piomelli, "High Reynolds number calculations using the dynamic subgrid-scale stress model," *Phys. Fluids A* **5**, 1484 (1993).
- ¹²U. Piomelli, Y. Yu, and R. J. Adrian, "Subgrid-scale energy transfer and near-wall turbulence structure," *Phys. Fluids* **8**, 215 (1996).
- ¹³J. Kim, P. Moin, and R. D. Moser, "Turbulence statistics in fully-developed channel flow at low Reynolds number," *J. Fluid Mech.* **177**, 133 (1987).
- ¹⁴N. N. Mansour, J. Kim, and P. Moin, "Reynolds stress and dissipation-rate budgets in a turbulent channel flow," *J. Fluid Mech.* **194**, 15 (1988).
- ¹⁵R. H. Kraichnan, "Eddy viscosity in two and three dimensions," *J. Atmos. Sci.* **33**, 1521 (1976).
- ¹⁶J. A. Domaradzki, W. Liu, and M. E. Brachet, "An analysis of subgrid-scale interactions in numerically simulated isotropic turbulence," *Phys. Fluids A* **5**, 1747 (1993).
- ¹⁷J. A. Domaradzki, W. Liu, C. Härtel, and L. Kleiser, "Energy transfer in numerically simulated wall-bounded turbulent flows," *Phys. Fluids* **6**, 1583 (1994).



A numerical study of three-dimensional wall-bounded flows

Gary N. Coleman, John Kim, and Anh-Tuan Le

Mechanical and Aerospace Engineering Department, University of California, Los Angeles, Los Angeles, CA, USA

Nonequilibrium three-dimensional (3-D) turbulent boundary layers are studied using direct numerical simulation (DNS). Time-developing flows are used to investigate the physics of spatial-developing ones. We find that application of a spanwise shear leads to the reduction of both the turbulent kinetic energy and drag, with the most dramatic reduction of the latter occurring when the shear is applied between $y^+ \approx 5$ and 15. When the three-dimensionality is produced by transverse skewing, the resulting alteration of the relationship between the Reynolds stresses is associated in large part with the effect of the pressure gradient upon the amplification or attenuation of the turbulent kinetic energy.

Keywords: turbulence; direct numerical simulation; channel flow; three-dimensional boundary layers

Introduction

Flows over swept-wing aircraft, within turbomachines, and over hulls of marine vehicles all share a common feature: their velocities change not only magnitude but also direction with distance from the surface. Thus, they can all be classified as three-dimensional (3-D) boundary layers (3DBL), the subject of the present study. Here our attention is limited to the nonequilibrium case, in which the 3DBL is created by an abrupt change of the mean flow to which the turbulence has not yet adjusted. This choice is motivated by its relevance to many technically important flows (such as the three cited above), and by the fact that the physics of nonequilibrium 3DBLs is not well understood. For example, when an initially two-dimensional (2-D) equilibrium boundary layer is suddenly subjected to a spanwise shearing force by the impulsive motion of the surface, the resulting nonequilibrium flow can experience a *decrease* of turbulent kinetic energy (see below); because the addition of a mean strain typically causes the turbulence to become *more* energetic, this behavior is somewhat paradoxical. On the other hand, when the mean streamwise vorticity appears, not because of a moving wall, but by skewing of spanwise vorticity with a transverse strain (such as that produced by a curved duct) that deflects the entire layer, the turbulent kinetic energy has been observed to both increase (Schwarz and Bradshaw 1994) and decrease (Bradshaw and Pontikos 1985), presumably depending upon the nature of the streamwise pressure gradient. Moreover, regardless of whether the three-dimensionality is due to surface shear or transverse straining (i.e., for both the "shear-driven" and "pressure-driven" versions), the "structure" of the Reynolds stresses is usually altered, because the ratio of the turbulent shear stress magnitude

to the turbulent kinetic energy decreases. This implies that turbulence in nonequilibrium 3DBLs is "less efficient" at extracting energy from the mean.

These observations illustrate the difficulty associated with correctly modeling 3DBLs. Another problem, related to the "structural" one mentioned above, is that as the turbulence reacts to the imposed crossflow, the Reynolds stresses do not instantaneously adjust to changes in the mean shear. Therefore, models based on an isotropic eddy-viscosity, or, indeed, any concept developed for 2-D equilibrium boundary layers, cannot, in general, be assumed to be valid for this flow. It is hoped that this study, in which we perform numerical experiments on "canonical" 3DBLs in an attempt to isolate various effects of three-dimensionality, will remove some of these modeling uncertainties by improving our understanding of the physics of nonequilibrium 3DBLs.

Approach

Three flow configurations are considered, with the mean three-dimensional flow created by shear for the first two, and by transverse strain for the third. All three assume a plane channel geometry and are studied using direct numerical simulation (DNS); because all relevant scales of motion are resolved, no turbulence or subgrid-scale model is needed. The shear-driven cases (denoted here by an SD prefix) are the result of impulsive motion of the lower channel wall, either by suddenly imposing a constant spanwise velocity w_x upon fully developed 2-D Poiseuille flow or by suddenly stopping the wall after the turbulence has adjusted to the wall motion. The runs subjected to transverse strain (indicated by prefix TS) utilize a constant uniform irrotational mean deformation $dU/dx = -dW/dz$ in the streamwise-spanwise (x - z) plane. This deformation represents either a streamwise expansion or contraction, and thus corresponds to either a favorable or adverse streamwise pressure gradient in a boundary layer. (The actual streamwise pressure gradient is

Address reprint requests to Dr. G. N. Coleman, Mechanical and Aerospace Engineering Department, University of California, Los Angeles, 48-121 Engr. IV, Box 951597, Los Angeles, CA 90095-1597, USA.

Received 6 November 1995; accepted 30 January 1996

Int. J. Heat and Fluid Flow 17: 333-342, 1996
© 1996 by Elsevier Science Inc.
655 Avenue of the Americas, New York, NY 10010

0142-727X/96/\$15.00
PII S0142-727X(96)00042-2

turned off during the straining.) Therefore, it produces, for a flow with nonzero mean spanwise velocity \bar{w} , a skewed 3-D boundary layer that allows, for example, investigation of the "inviscid skewing" mechanism (Bradshaw 1987). (Throughout this paper, the terms streamwise and spanwise are used respectively to indicate the x - and z -directions, and u - and w -components of velocity, even when the x -axis does not correspond to the actual downstream direction of the mean flow; the y -coordinate denotes the wall-normal direction, and v , the wall-normal velocity.) Whereas previous DNS studies have assumed both the strain and turbulence were homogeneous (Rogallo 1981), here we apply the uniform strain to turbulence between two no-slip surfaces. For this we deform both the flow and the (elastic) channel walls. Consequently, the near-wall turbulence for the present and actual skew-induced 3-D boundary layers will not always correspond. Nevertheless, because the outer flow behavior is of primary interest for this type of 3DBL, the transversely strained results are expected to be useful, especially for differentiating between physics of the shear-driven and pressure-driven cases.

The results to follow have been obtained using the spectral channel-flow code of Kim et al. (1987), after it was modified to compute the cases described above. All variables are nondimen-

Table 1 Case parameters

Case	w_s	u_s	dU/dx	IC
SD1	-8.5	0	0	2D*
SD2	0	0	0	collateral†
SD3	0	+8.5	0	2D*
TS1	-8.5	0	-100	collateral†
TS2	-8.5	0	+100	collateral†

* Kim et al. (1987); † Case SD1 at $t = 1.73$

sionalized by the channel half-width δ^* , and (in order to highlight changes in time) the constant wall-shear velocity from the 2-D Poiseuille flow initial condition. Because of the time-dependence of the results, mean quantities (denoted by an overbar) are obtained by averaging over planes parallel to the walls, and for Case SD1 also over three independent simulations. A summary of case parameters is given in Table 1. In addition to those listed, a series of runs using a time-independent spanwise shear are also discussed (see Table 2 below). Three sets of numerical parameters are used: for Cases SD1, SD2, TS1, and TS2, the streamwise and spanwise domain size L_x^* and L_z^* are $4\pi\delta^*$ and $8\pi\delta^*/3$,

Notation

a_1	Reynolds stress structure parameter, $(\bar{u}^2 \bar{v}^2 + \bar{v}^2 \bar{w}^2)^{1/2}/q^2$
dU_i/dx_i	constant uniform rate of irrotational strain
h	height below which constant spanwise shear is applied
L_x^*, L_z^*	streamwise and spanwise dimensions of computation domain, respectively
n_x, n_y, n_z	number of equivalent grid points in the streamwise, wall-normal, and spanwise directions, respectively
q^2	twice the turbulent kinetic energy, $\bar{u}_i \bar{u}_i$
Re_τ	Reynolds number, $(u_\tau^*)_{ic} \delta^*/\nu^*$
S	magnitude of strain rate, $ dU_i/dx_i $
t	nondimensional time, $t^*(u_\tau^*)_{ic}/\delta^*$
T	oscillation period of spanwise pressure gradient or spanwise wall motion
u, v, w	nondimensional streamwise, wall-normal, and spanwise velocity components, respectively, $(u^*, v^*, w^*)/(u_\tau^*)_{ic}$
\bar{u}, \bar{w}	mean streamwise and spanwise velocities, respectively
$\bar{u}'\bar{v}', \bar{v}'\bar{w}'$	streamwise and spanwise Reynolds shear stresses, respectively
u_s, w_s	constant streamwise and spanwise velocities of lower channel wall, respectively
$(u_\tau^*)_{ic}$	mean surface friction velocity of initial fully developed 2-D Poiseuille flow field
x, y, z	nondimensional streamwise, wall-normal, and spanwise coordinates, respectively, $(x^*, y^*, z^*)/\delta^*$
y_w	distance from lower wall, $(\delta^* + y^*)/\delta^*$
y^+	nondimensional distance from the wall, $y_w^* u_\tau^*/\nu^*$

Greek

α	local skewing angle, $\arctan(S)$
β	angle between the collateral flow and local skewing directions

δ^*	half-width of channel
ε	rate of dissipation of turbulent kinetic energy
ζ	Stokes's second problem similarity variable, $y^+(\pi)^{1/2}/(T^*)^{1/2}$
η	Stokes's first problem similarity variable, $y_w^*/2(\nu^* t^*)^{1/2}$
θ	angular difference in orientation of skewed mean vorticity between cases with and without initial component of mean vorticity in pure skewing direction, as predicted by generalized Squire-Winter-Hawthorne relationship
λ	angle between mean shear and Reynolds stress, $\arctan[(\partial \bar{w}/\partial y)/(\partial \bar{u}/\partial y)] - \arctan[(\bar{v}'\bar{w}')/(\bar{u}'\bar{v}')]^2$
ν^*	kinematic viscosity
ξ	eddy-viscosity ratio, $[\bar{v}'\bar{w}']/(\partial \bar{w}/\partial y)/[\bar{u}'\bar{v}']/(\partial \bar{u}/\partial y)$
$(\bar{\tau}_x, \bar{\tau}_z)_w$	mean streamwise and spanwise shear, respectively, at $y^* = \pm \delta$ (averaged over both walls)
ω_i	vorticity, $\omega_i^*/[(u_\tau^*)_{ic}/\delta^*]$

Indices

Q^*	dimensional quantity
Q^+	quantity nondimensionalized by u_τ^* and ν^*
\bar{Q}	average over (x, z) -planes (and where noted, over independent simulations)
Q'	fluctuation component, $Q - \bar{Q}$
Q_c	variable measure at channel centerline
Q_w or Q_s	value of Q at lower wall, $y^* = -\delta^*$
Q_{ic}	value from initial fully developed 2-D Poiseuille flow field

respectively, while the number of streamwise (n_x), wall-normal (n_y), and spanwise (n_z) grid points is $(n_x, n_y, n_z) = (256, 129, 256)$; Case SD3 uses $(L_x^*, L_z^*) = (4\pi\delta^*, 4\pi\delta^*/3)$ and $(n_x, n_y, n_z) = (128, 129, 128)$, while $(L_x^*, L_z^*) = (4\pi\delta^*, 4\pi\delta^*/3)$ and $(n_x, n_y, n_z) = (32, 65, 32)$ for the constant spanwise-shear simulations. The results presented below verify that with these parameters all essential scales of motion are fully resolved (see, for example, Figures 5, 6, 7, and 12, and compare diagnostics discussed in Kim et al.).

Results: shear-driven cases

Spanwise moving wall ($w_s \neq 0$)

Three-dimensional boundary layers free of adverse pressure gradient effects can be created by introducing mean streamwise vorticity at the surface. We begin our examination of this so-called shear-driven case with Run SD1, for which an impulsive spanwise motion is applied to the lower wall of a stationary 2-D plane channel flow—hence, the ‘2-D’ in the ‘IC’ column in Table 1. The fully developed initial field is as described in Kim et al. (1987), with Reynolds number based on surface friction velocity and channel half-width $Re_\tau \approx 180$. The boundary layer that develops above the moving wall is analogous to that found in rotating cylinder experiments (Furuya et al. 1966; Lohmann 1976; Driver and Hebbbar 1991) in the region where the longitudinal flow along the cylinder first encounters the rotating section. It is also similar to that found by Moin et al. (1990) and Sendstad and Moin (1992), who used DNS to study the transient response of a 2-D channel flow to a suddenly imposed spanwise pressure gradient. This similarity is no surprise, given that the effect of the spanwise pressure gradient is equivalent (because of the streamwise homogeneity of the plane channel) to subjecting the walls to a uniform spanwise acceleration. Many of the results found here are qualitatively similar to those found earlier by Sendstad and Moin. There are fundamental differences, however, between the accelerating and constant-velocity wall flows: the equilibrium state of the former is a reoriented Poiseuille flow, while here the moving wall leads first to an equilibrium ‘collateral’ boundary layer (a flow for which the (new) direction of the mean velocity remains constant in y), and eventually—once the spanwise shear diffuses across the channel centerline to the stationary wall—to an equilibrium skewed 3DBL Poiseuille/Couette configuration (because the direction of the mean velocity varies approximately linearly in y). (Had we set both walls in motion in the same direction, the final state would have been two equilibrium collateral boundary layers.) In this paper, we consider times shorter than those required for the spanwise mean shear to diffuse across the centerline; therefore, only the nonequilibrium-to-collateral transition. Another difference between the present and Sendstad and Moin’s study is that, because they were interested only in the nonequilibrium state, their domain size and numerical resolution were insufficient to capture their reoriented 2-D flow accurately, with its associated smaller streamwise scales. Here, however, because of the central role played by the collateral boundary layer, it is necessary to use numerical parameters sufficient to correctly represent both the transient and long-time behaviors.

The imposed spanwise wall velocity for Case SD1, $w_s = -8.5$, is about half the initial mean streamwise velocity at the centerline \bar{u}_c [and, therefore the collateral flow angle will be about $26^\circ \approx \arctan(0.5)$]. To avoid a discontinuity in y , an early-time Stokes solution for the impulsively started flat plate is used to specify the initial distribution of $\bar{w}(y)$. At this Reynolds number, the \bar{w} -profile imposed at $t = 0$ corresponds to the Stokes solution at $t = 0.0045$. The resulting variation in time of the mean span-

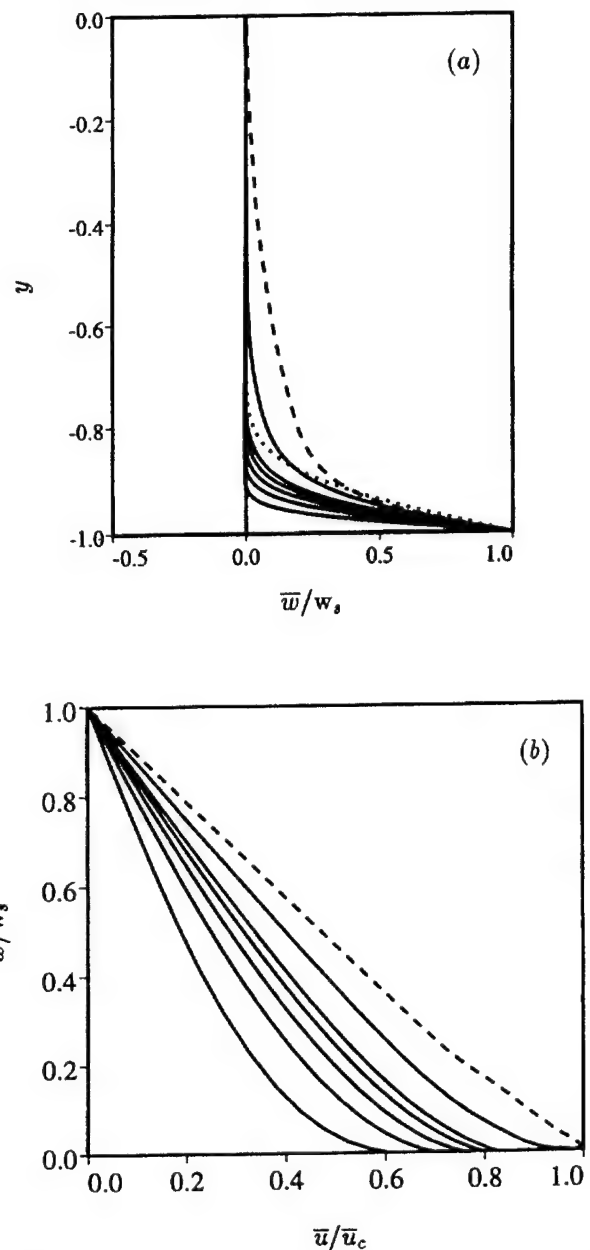


Figure 1 Mean (a) spanwise velocity and (b) hodograph for Case SD1: —, ensemble average over three independent realizations for time sequence $t = 0.075, 0.150, 0.225, 0.300, 0.375$, and 0.750 ; ----, laminar Stokes solution at $t = 0.75$; ----, plane average over single realization at $t = 1.73$; time normalized by channel half-width and surface friction velocity from initial field

wise velocity profile is shown in Figure 1a. The solid curves represent an average over planes parallel to the walls and over three independent realizations beginning from three different initial fields. The dotted curve illustrates the Stokes solution at the time corresponding to the last ensemble-averaged result ($t = 0.750$). Even at this last time, the laminar and turbulent profiles are not drastically different; at $t = 0.375$ the agreement between the Stokes solution (not shown), and the Case SD1 profile is significantly better—a consequence of the slow development of the spanwise Reynolds stress $\overline{v'w'}$. The dashed curve in Figure 1a shows the spanwise velocity at $t = 1.73$. As the polar

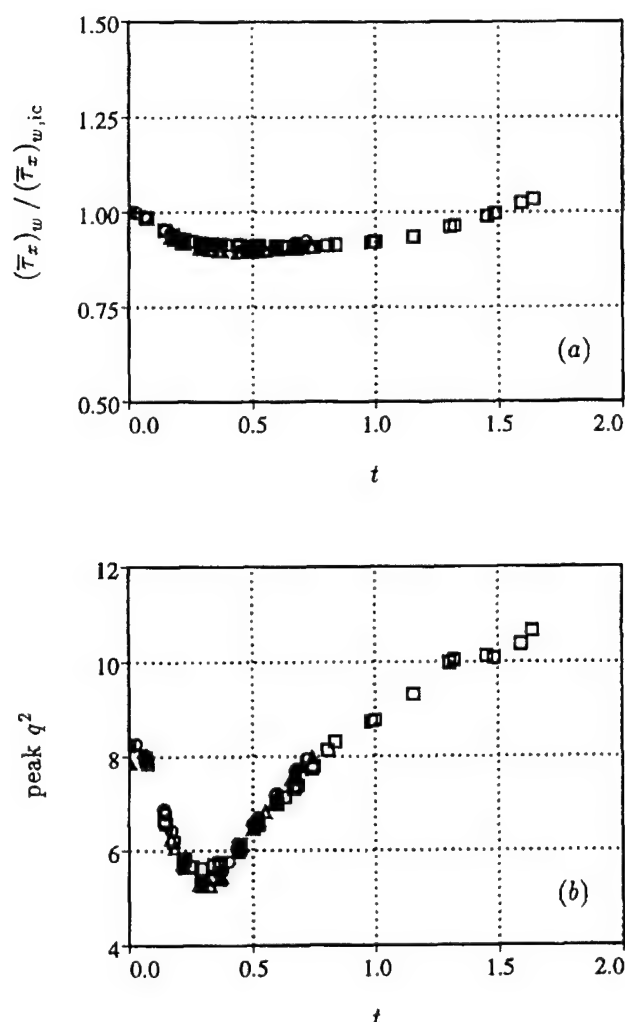


Figure 2 History of (a) mean streamwise wall shear stress (normalized by initial value) and (b) maximum q^2 for Case SD1: symbols denote planar averages from three independent realizations

velocity plot in Figure 1b indicates (because the direction of the mean velocity is very nearly constant with distance from the surface) the flow at this time is to a good approximation collateral. The $t = 1.73$ field is used as initial conditions for some of the cases described below (see Table 1).

Adding a spanwise component to the shear at the wall causes a reduction in the streamwise component, as Figure 2a shows. The streamwise wall shear drops to a minimum of about 90% of its initial value before the added shear leads to its eventual growth. (Simulations other than those presented here indicate that imposing a larger shear produces a larger wall-shear reduction than found for Case SD1.) The drop in turbulent kinetic energy $(1/2)q^2 = (1/2)\overline{u'u'}$, associated with the wall-shear decrease can be seen in Figure 3a. The effect spreads away from the wall in time, as more and more of the layer experiences a drop in q^2 as time passes. A trace of the history of the near-wall peak of q^2 is presented in Figure 2b. Its behavior is similar to that of the wall shear, in that an initial reduction precedes growth to greater than initial values. The maximum q^2 begins to grow sooner than the wall shear does, however.

Figure 3b shows how the relationship between the components of the Reynolds stress tensor is altered by the spanwise

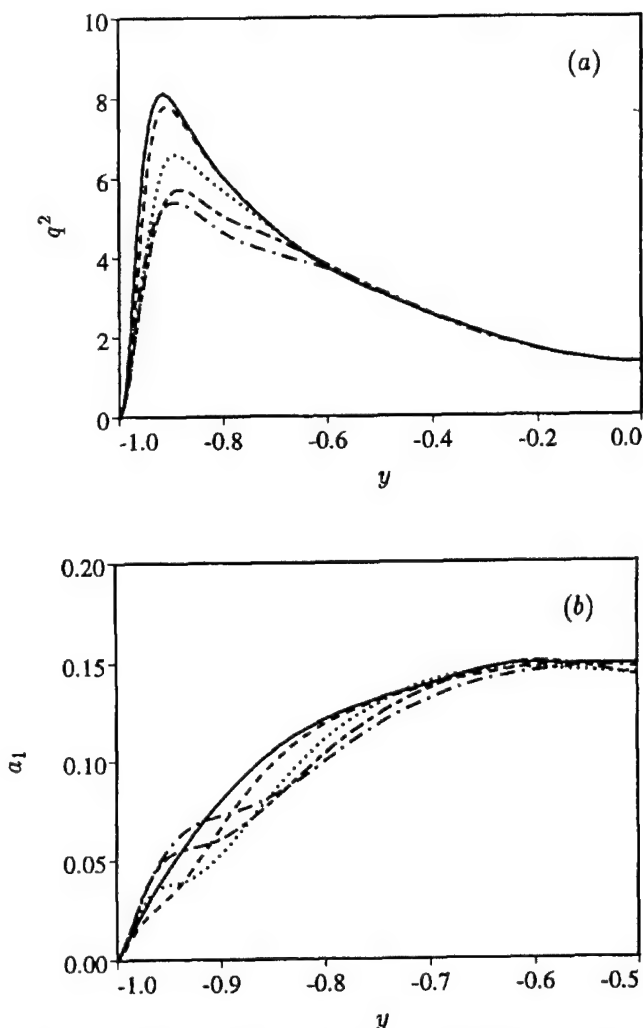


Figure 3 Profiles of (a) q^2 and (b) structure parameter for Case SD1: —, $t=0$; ---, $t=0.075$; ····, $t=0.150$; —·—, $t=0.225$; —·—, $t=0.300$; structure parameter $a_1 = [(\overline{u'u'})^2 + (\overline{v'v'})^2]^{1/2}/q^2$; ensemble average over three realizations

shear: the structure parameter a_1 is significantly reduced. This reduction, which is a central feature of nonequilibrium 3DBLs, implies that for the shear-driven case the decrease in magnitude of the lateral shear stress is even more rapid than that of the turbulent kinetic energy. Note that the shear-induced reduction of both a_1 and q^2 propagates away from the wall in time. The finite lag between the angles of the mean shear and shear stress (Figure 4a) is such that, while they eventually coincide as the collateral state is approached, initially the two angles differ by almost 40° . The shear always "leads" the stress so that $\arctan[(\partial \overline{w}/\partial y)/(\partial \overline{u}/\partial y)] - \arctan(\overline{v'w'}/\overline{u'v'})$ remains positive. A more straightforward demonstration of the difficulty associated with using a scalar eddy-viscosity to model this flow is presented in Figure 4b, which illustrates the evolution of the ratio of the spanwise to streamwise eddy-viscosity; only after q^2 begins to grow (cf. Figures 2b and 4b) does this ratio begin to approach one.

The spatial structure of the turbulence is also modified by the moving wall. We find that the smallest scales of motion adjust most rapidly to changes in mean flow conditions. This observation, which was previously made by Sendstad and Moin (1992) in

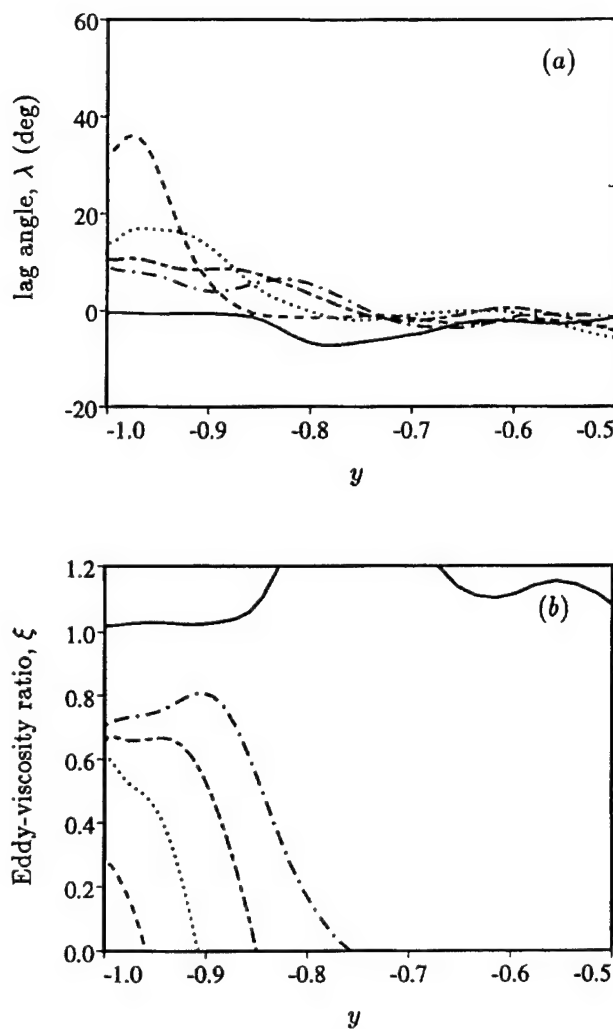


Figure 4 Profiles of (a) difference between angles of mean shear and shear stress and (b) ratio of spanwise to streamwise eddy-viscosity for Case SD1: —, $t = 1.73$; other symbols as in Figure 3. Lag angle, $\lambda = \arctan[(\partial \bar{w}/\partial y)/(\partial \bar{u}/\partial y)] - \arctan[(v'w')/(\bar{u}'v')]$; eddy-viscosity ratio, $\xi = [v'w']/(\partial \bar{w}/\partial y)/[\bar{u}'v']/(\partial \bar{u}/\partial y)$

their 3DBL DNS study, is supported by the two-dimensional energy spectra shown in Figure 5. These spectra also indicate the numerical fidelity of the DNS results, over the entire 2-D-to-collateral flow range. (The same conclusion is also reached when the one-dimensional (1-D) spectra (not shown here) are examined.) At this y -location (which in wall units initially corresponds to $y^+ \approx 15$), the high-level contours at low wavenumbers are "turned" more slowly than are their low-level high-wave number counterparts. The enstrophy profiles in Figure 6a also imply that at this location ($y = -0.92$) the smaller scales initially become more energetic. Part of the previously noted drop in the peak q^2 —in addition to being the result of reduced production caused by lower mean shear and turbulent shear stress (Figures 2a and 3b)—is, therefore, due to an increase in the rate of turbulent kinetic energy dissipation ε . Near the wall, however, the vorticity fluctuations weaken in time, indicating that here the energy at smaller scales (and, hence, the dissipation rate) is diminished. The time-dependent influence of the spanwise shear on the location of the maximum enstrophy can be accounted for to some degree by using the similarity variable of the laminar Stokes solution,

$\eta = y_w^*/2(v^*t^*)^{1/2}$ (using the $*$ superscript to denote dimensional variables, with v^* the kinematic viscosity, and $y_w^* = \delta^* + y^*$), to rescale the wall-normal coordinate. When this is done (Figure 6b) the enstrophy maximum is found for the times considered to remain near $\eta \approx 1$.

More instantaneous structural information is available in Figure 7, which shows contours of wall-normal vorticity in x - z planes just above the moving wall from one of the Case SD1 realizations, revealing the effect of the imposed spanwise shear upon the streaks. They are first weakened and "torn" into smaller structures; later they become stronger and more elongated as they realign in the collateral flow direction.

A complication in the analysis of Case SD1 is the time-dependent nature of the imposed mean spanwise shear. Although some of the time-dependence can be removed by using laminar theory, as in Figure 6b, the fact that $\partial \bar{w}/\partial y$ varies in both y and t makes it difficult to determine the mechanisms responsible for, for example, the turbulent drag reduction, because different near-wall structures exist at different y^+ locations. We have, therefore, performed a series of runs using "synthetic" time-independent mean spanwise velocities: a uniform spanwise shear $d\bar{w}/dy$ of equal magnitude is applied over various regions, and held constant in time. Because we are primarily interested in the initial response of the turbulence to the applied shear, we do not allow the imposed initial \bar{w} profile to change in time under the influence of viscosity, and the turbulence; $d\bar{w}/dy$ is held fixed to make comparisons more straightforward than they would be if \bar{w} evolved naturally. Because our attention is upon near-wall behavior, it is possible to specify a lower-Reynolds number for these runs than was used to obtain the Case SD1 results described above. Instead of 180, here the initial Re_τ is 112. This greatly reduces the computational expense, because at $Re_\tau = 112$ only $(n_x, n_y, n_z) = (32, 65, 32)$ collocation points are required, which allows us to explore a wider parameter range for a given amount of CPU time than would be possible at higher-Reynolds numbers. (We have also used the "minimal channel" geometry (Jiménez and Moin 1991) to investigate the effect of constant spanwise shear upon 2-D channel flow. However, because in the present study we choose to impose $d\bar{w}/dy$ at locations fairly far away from the walls, those results are not presented here, in order to avoid uncertainties that might be present in minimal-channel statistics from far-wall regions.)

Three series of constant-shear simulations were made; these are denoted by a CSD prefix and summarized in Table 2. Each series uses a distinct value of constant $d\bar{w}/dy$ (either 50, 200, or 800% of the initial mean streamwise wall shear), and contains eight individual runs, which are defined by the height h above the wall over which $d\bar{w}/dy$ is imposed. The region of uniform shear extends from the surface to h^+ , measured in wall-units of the initial 2-D field, which varies from 5 to 40 in increments of 5. To prevent a discontinuity in the \bar{w} profile, above $1 - |y| = h$ the spanwise shear drops to zero as a Gaussian that falls to 1% of its nominal value over five initial wall units. The shear is applied over both sides of the channel, so that both walls are set in motion in the same direction at a constant spanwise velocity proportional to $h d\bar{w}/dy$.

A comparison of mean streamwise surface drag histories is shown in Figure 8; a reduction with time is found in all instances, with the drop proportional to the magnitude of the applied shear (cf. Figure 8a, b, and c). The weakest effect occurs when the shear is imposed between $y_{ic}^+ = 0$ and 5 (y_{ic}^+ is the wall-normal coordinate in wall-units of the initial field), with a cumulative drag reduction as the depth of the sheared region increases. Note, however, that once the shear extends beyond $y_{ic}^+ \approx 25$ for the weakest shear (Series CSD1; Figure 8a), and $y^+ \approx 15$ for the largest $d\bar{w}/dy$ (Series CSD3; Figure 8c), further increases in h^+

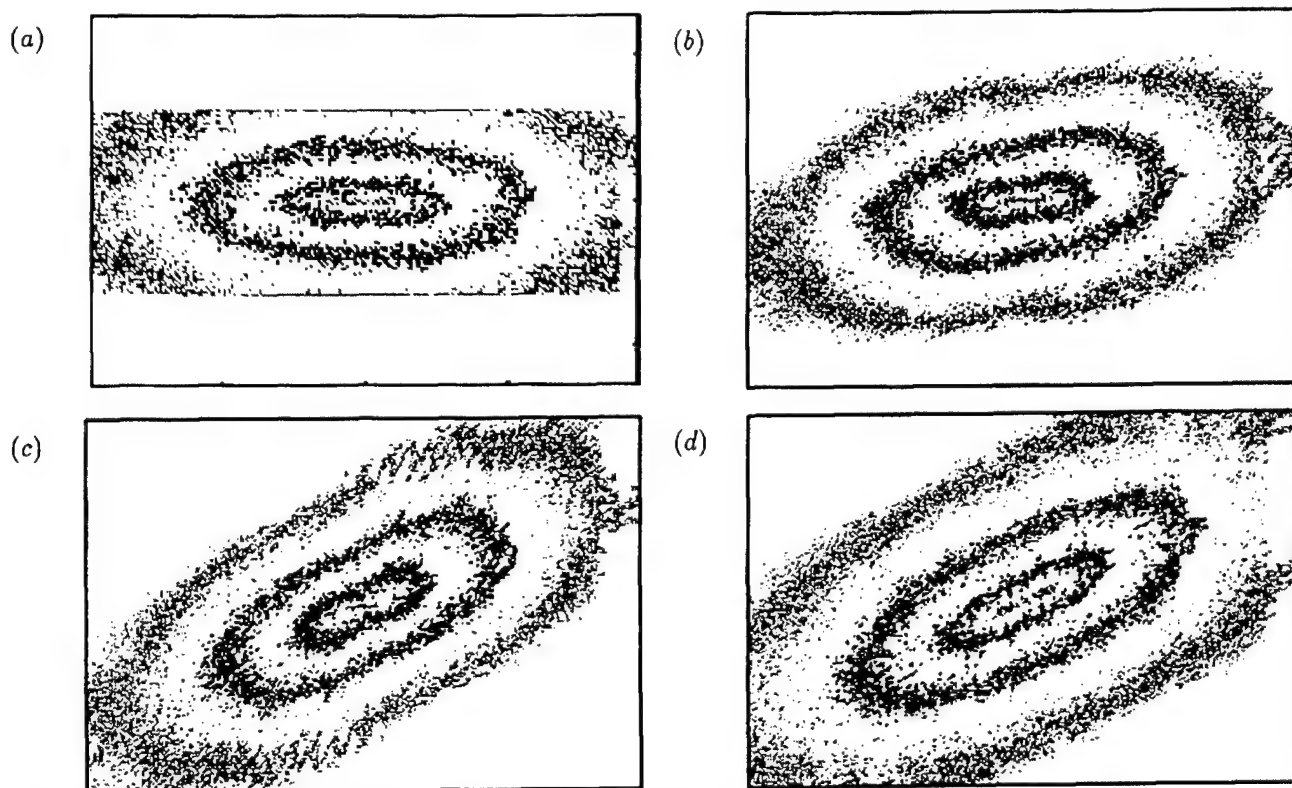


Figure 5 Two-dimensional energy spectra at $y_w = 1 + y = 0.08$ ($y_{ic}^+ \approx 15$) at (a) $t=0$, (b) 0.14, (c) 0.29, and (d) 1.73 for one realization of Case SD1: contours indicate constant values, in intervals of -1.8 , of logarithm of spectra, normalized by maximum value at each time; horizontal and vertical axes are spanwise and streamwise wave numbers, respectively, with mean mode at center

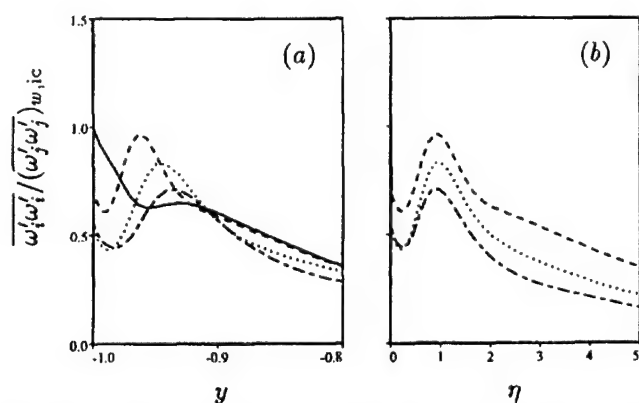


Figure 6 Vorticity fluctuation profiles, normalized by initial wall value, versus (a) y and (b) η for Case SD1: symbols as in Figure 3

do not lead to a significant change in the rate of drag decrease. Moreover, the greatest "jump" in the drag reduction occurs when h^+ moves from $y_{ic}^+ = 10$ to 15 for the weak shear runs (CSD1), and from $h^+ = 5$ to 10 for Series CSD3, for which $d\bar{w}/dy$ is largest. This indicates that the "optimal shearing"—that which most deeply disrupts the 2-D equilibrium state—is application of $d\bar{w}/dy$ to the region between $y^+ \approx 5$ and 15, with a tendency for the "critical region" to shift towards the lower limit as the spanwise shear increases.

In the version of this paper presented at TSF-10, the upper limit of the range of maximum influence was found to be

$y^+ \approx 10$, not $y^+ \approx 15$, as it is here. This is because there instead of considering histories of mean surface shear stress, turbulent kinetic energy histories were analyzed. It was subsequently discovered that the development of the streamwise surface drag is a better measure of 3DBL behavior, because it is less sensitive than q^2 to the magnitude of the applied spanwise shear; at very large shear rates, the surface drag and kinetic energy histories show opposite trends, with the former decreasing in time, while the latter experiences rapid growth. (Another, less significant, reason for the difference is that the q^2 -histories previously presented were not taken from the minimal-channel runs described earlier, as claimed, but from preliminary coarse-grid simulations; however, because results from the two runs were quite similar, the influence of this error was slight.)

These constant-shear findings are perhaps related to the effect of an oscillating spanwise mean pressure gradient (or equivalently spanwise oscillating walls) upon turbulent boundary layers. Numerical (Jung et al. 1992) and experimental (Laadhari et al. 1994) studies have shown that maximum suppression of turbulence occurs when the spanwise oscillation period in wall units is about $T^+ = 100$. Because of the applicability of the laminar theory for the mean spanwise velocity for the oscillating wall flow (Jung et al.), a connection can be made between the $T^+ \approx 100$ optimum, and the above observation that shear below $y^+ = 15$ is most effective: at $T^+ = 100$ and $y^+ = 15$, the similarity variable ζ for the laminar solution, which can be written as $\zeta = y^+(\pi)^{1/2}/(T^+)^{1/2}$, gives $\zeta/(\pi)^{1/2} = 1.5$, which is close to the effective depth of the boundary layer created by the oscillating wall, as shown in Figure 9.

Finally, we comment on the significance of the present results for theories regarding the structural mechanisms responsible for

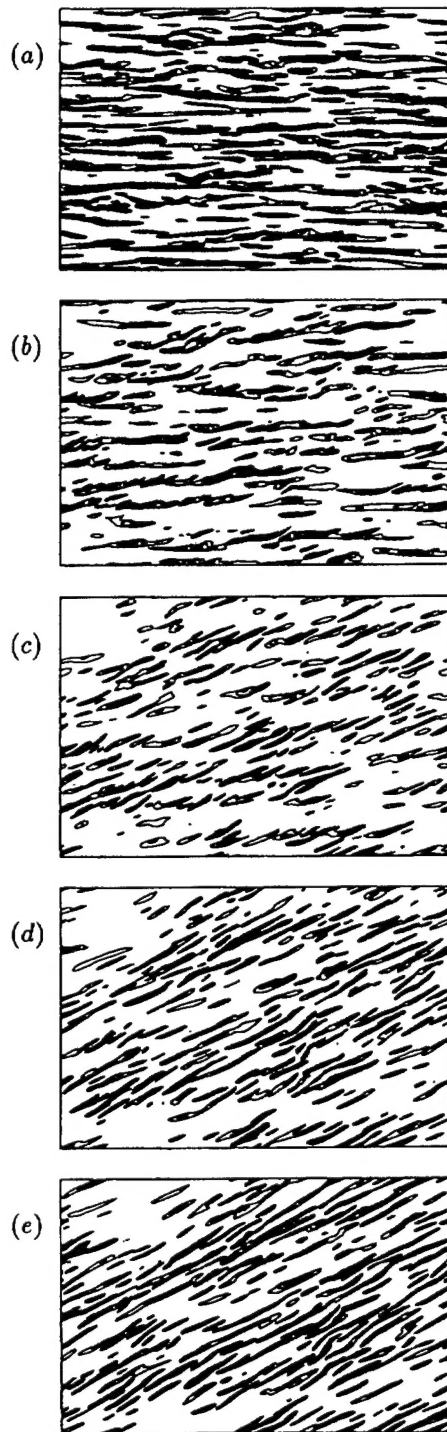


Figure 7 Contours of wall-normal vorticity on (x, z) -planes at $y_w = 1 + y = 0.003$ ($y_{ic}^+ \approx 0.5$) at (a) $t=0$, (b) 0.075, (c) 0.150, (d) 0.225, and (e) 0.300 for one realization of Case SD1; —, $\omega_y > 0$; contour interval = 1; flow at centerline from left to right; spanwise wall motion from top to bottom; planes represent full flow domain

the drag reduction in shear-driven 3DBLs. One suggestion is that the reduction is due to the spanwise shear directly modifying the near-wall quasi-streamwise vortices, thereby weakening the energy production cycle (Eaton 1995). Although the present results are not inconsistent with this theory, because on average, the quasi-streamwise vortices are found near $y^+ = 20$ (which is just

Table 2 Constant spanwise-shear runs

Series	$\frac{d\bar{w}}{dy} / \left(\frac{\partial \bar{u}}{\partial y} \right)_{w,ic}$
CSD1	0.5
CSD2	2.0
CSD3	8.0

above the "optimal shearing" region of $5 < y^+ < 15$), the greatest influence of shear-driven three-dimensionality appears to be due to modification of the "bottoms of" the vortices, the "tops of" the streaks, or of the interaction between the two. We also note that applying a spanwise shear in the region below $y^+ = 5$ produces a smaller drag reduction than when $d\bar{w}/dy$ is imposed between $y^+ \approx 15$ and 25 (Figure 8), which suggests that the weakening and "shredding" of the streaky structure observed very near the wall at $y_{ic}^+ \approx 0.5$ (Figure 7) is more a symptom of the three-dimensionality than an important part of the dynamics.

Stationary wall ($w_s=0$)

The other type of shear-driven 3DBL considered here also has an analog in the rotating cylinder experiments: by suddenly stopping the spanwise-moving wall in the channel after a collateral state has developed, an effect comparable to passing from the rotating to stationary section in the experiments is produced. The initial condition for this stopped-wall run, Case SD2, is obtained from Case SD1 at $t = 1.73$. As can be seen from the

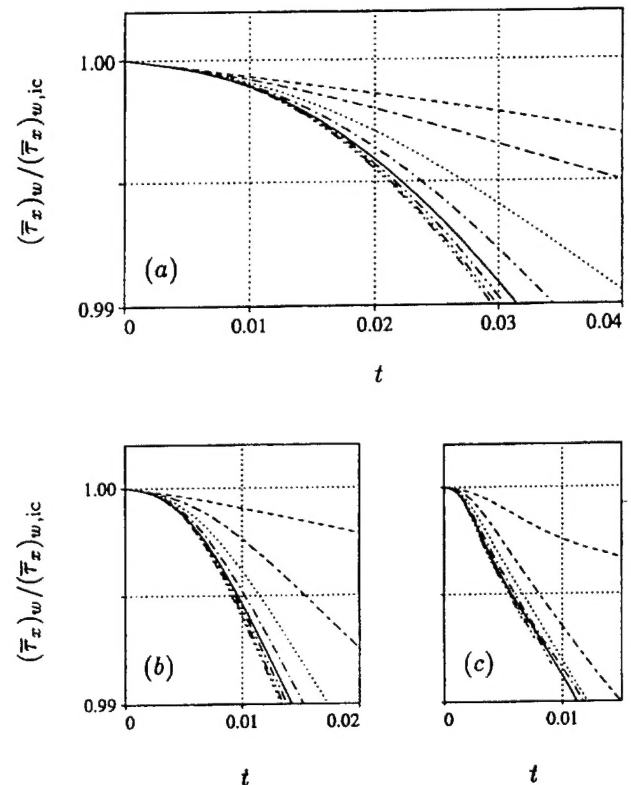


Figure 8 History of mean streamwise wall shear stress, normalized by initial value, for constant spanwise-shear runs, Series (a) CSD1, (b) CSD2 and (c) CSD3: —, $h^+ = 5$; — —, $h^+ = 10$; - - - -, $h^+ = 15$; — · —, $h^+ = 20$; — — —, $h^+ = 25$; — · · —, $h^+ = 30$; — · · · —, $h^+ = 35$; — · · · · —, $h^+ = 40$; results at each time averaged over both walls

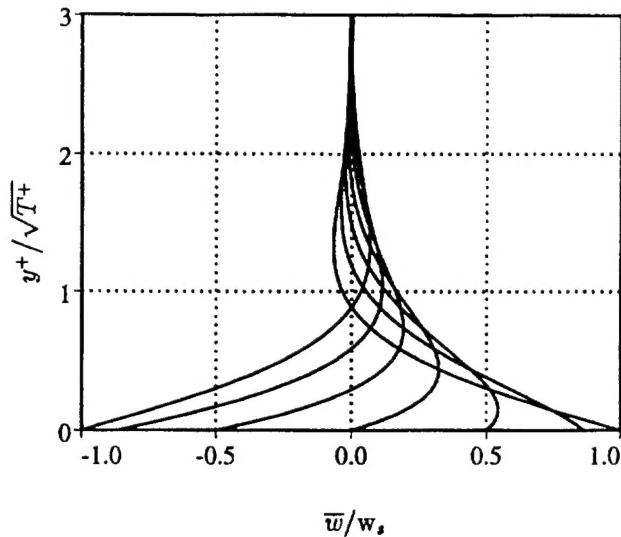


Figure 9 Stokes oscillating flat-plate solution: time sequence over half period in 30° increments

$t = 1.73$ results in the Case SD1 hodograph (Figure 1b) and the kinetic energy spectra (Figure 5d), the layer above the moving wall is effectively 2-D at this time. Thus, when the coordinate system coincides with the angle of the mean shear at the surface (26°), the resulting mean "spanwise" velocity has no y -variation (Figure 10). Consequently, the only difference between subjecting a 2-D boundary layer to an impulsive spanwise wall velocity and suddenly stopping the wall beneath a collateral boundary layer is that in the latter case the imposed wall shear has both a downstream and cross-stream component, the relative strengths of which depend upon the collateral flow angle. Because the applied downstream shear and the existing collateral surface shear are aligned and of opposite sign, the Case SD2 energy-drop (Figure 11) is due to both the cross-flow effect discussed above and also a straightforward reduction in the usual 2-D $-\overline{u'v'} \partial \overline{u} / \partial y$ production. However, although both the downstream and cross-stream components act to reduce the turbulent energy, their influence upon the flow structure is fundamentally different. Results from Case SD3, a run for which the lower channel wall is moved solely in the downstream direction, show, for

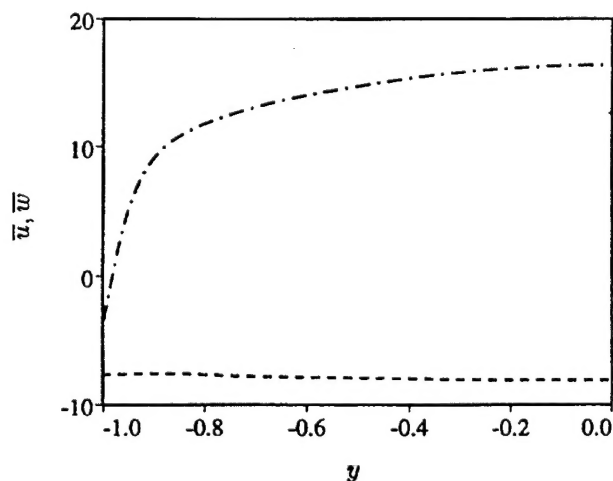


Figure 10 Mean velocity profiles in coordinate system aligned with direction of mean shear angle at the surface, for Case SD2 at $t=0$: —, \overline{u} ; ---, \overline{w}

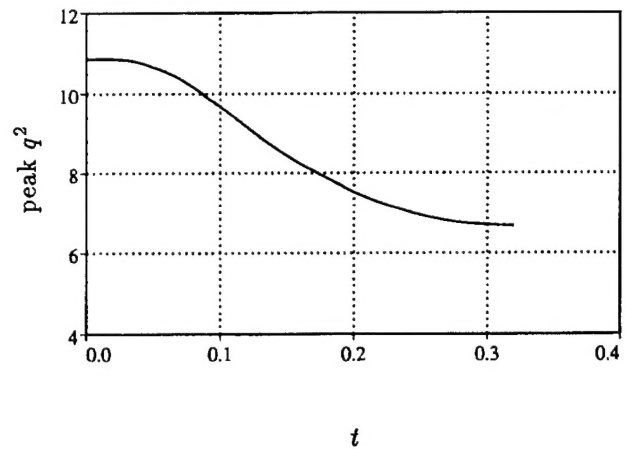


Figure 11 History of maximum q^2 for Case SD2

example, that the vorticity fluctuations are everywhere diminished by the streamwise shear (Figure 12), while the cross-flow (see Figure 6a) leads to an increase at some locations and a decrease at others.

Results: transversely strained cases

We conclude with some preliminary results from the strained channel simulations, Cases TS1 and TS2. The strain rate $S = |dU/dx|$ used for these runs is such that at the channel centerline the nondimensional strain-rate parameter $Sq^2/\varepsilon \approx 160$; this value of S is 48% of the mean shear at the surface, $[(\partial \overline{u} / \partial y)_w^2 + (\partial \overline{w} / \partial y)_w^2]^{1/2}$, of the initial collateral flow (Case TS1 at $t = 1.73$), and therefore represents a very rapid deformation. Note the opposite signs of dU/dx for the two simulations. If the collateral initial state were exactly aligned at 45° to the x -axis, the applied $dU/dx = -dW/dz$ strain would produce a pure irrotational skewing of the flow (i.e., in downstream coordinates the only nonzero terms of the strain rate would be the off-diagonal components $dU/dz = dW/dx$, as if a pressure gradient were acting at a right angle to the mean streamlines), and the only difference between Cases TS1 and TS2 would be that one would turn the flow (in time) to the right, and the other to the left,

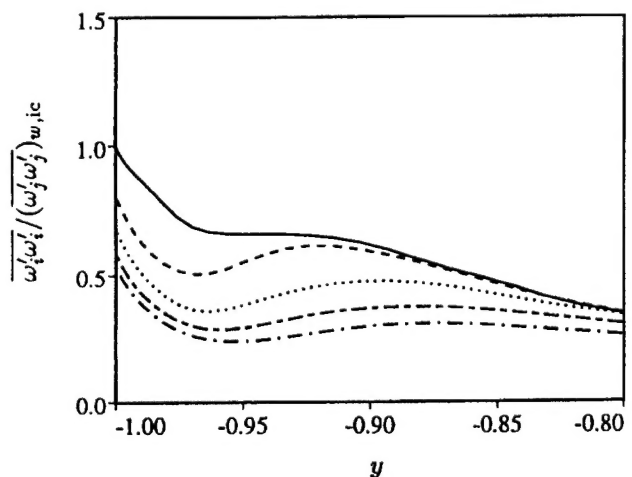


Figure 12 Vorticity fluctuation profiles, normalized by initial wall value, for Case SD3; symbols as in Figure 3

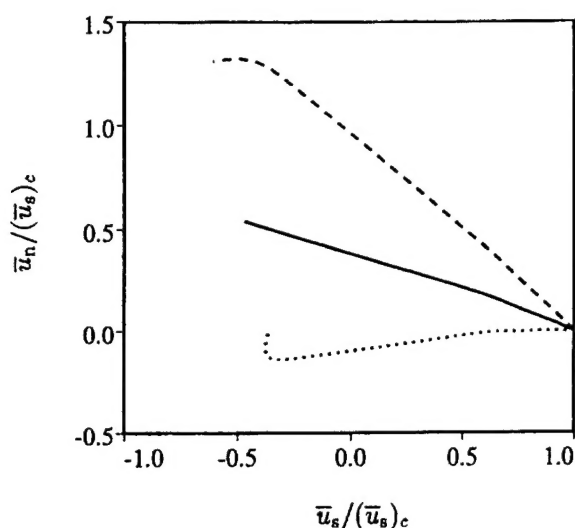


Figure 13 Mean velocity hodograph for Cases TS1 and TS2: —, $St=0$; ---, Case TS1 at $St=0.25$; ·····, Case TS2 at $St=0.25$; velocity components parallel \bar{u}_s and normal \bar{u}_n to local coordinates aligned with current direction of mean skewing, normalized by parallel component at centerline $(\bar{u}_s)_c$

respectively. However, because the collateral flow angle is 26° , the opposite signs of dU/dx correspond to a mean deceleration of the boundary layer in the downstream direction for Case TS1 and an acceleration for Case TS2.

Mean velocity hodographs are shown in Figure 13. The velocity components are measured with respect to the coordinate system defined by the turning angle of the irrotational skewing: the downstream direction is at $45^\circ + \alpha$ clockwise from the x -axis, where the effective turning angle $\alpha = \arctan(-t dU/dx)$. This choice allows us to check the validity of a generalized Squire-Winter-Hawthorne relationship for the mean velocity (Bradshaw 1987), derived by assuming that in the outer layer the evolution of the mean vorticity is simply given by skewing of vortex lines in the x - z plane (and taking into account that initially the mean vorticity has a component parallel to the pure-skewing direction of 45° to the x -axis). Thus, one can obtain that for the coordinate system used in Figure 13, the mean velocity should satisfy $\bar{u}_n = -\tan(\theta + 2\alpha)(\bar{u}_s - (\bar{u}_s)_c)$, where $\tan \theta = \tan \beta \cos 2\alpha / (1 + \tan \beta \sin 2\alpha)$, and $\beta = 45 - 26 = 19^\circ$ is the difference between the collateral flow and pure skewing directions. Measured clockwise from the horizontal axis, the predicted angles for Cases TS1 and TS2 are 43 and -8° , respectively, both of which are fairly close to the values observed in Figure 13. The behavior of q^2 (Figure 14a), and therefore, a_1 (Figure 14b) depends upon whether the effect of the mean strain represents that of an adverse or favorable pressure gradient. The kinetic energy increases, and structure parameter decreases, for the decelerating-strain flow, Case TS1; for Case TS2 the opposite occurs.

Conclusions

A DNS study of nonequilibrium 3DBLs indicates that for the shear-driven case, the greatest decrease in mean turbulent drag is obtained when a spanwise shear is applied in the region between $5 \leq y^+ \leq 15$; it is postulated that this result is related to the observation that maximum turbulence suppression occurs for boundary layers above oscillating surfaces when the spanwise-oscillation period is about $T^+ = 100$. The qualitatively different influence of suddenly applied spanwise and streamwise wall

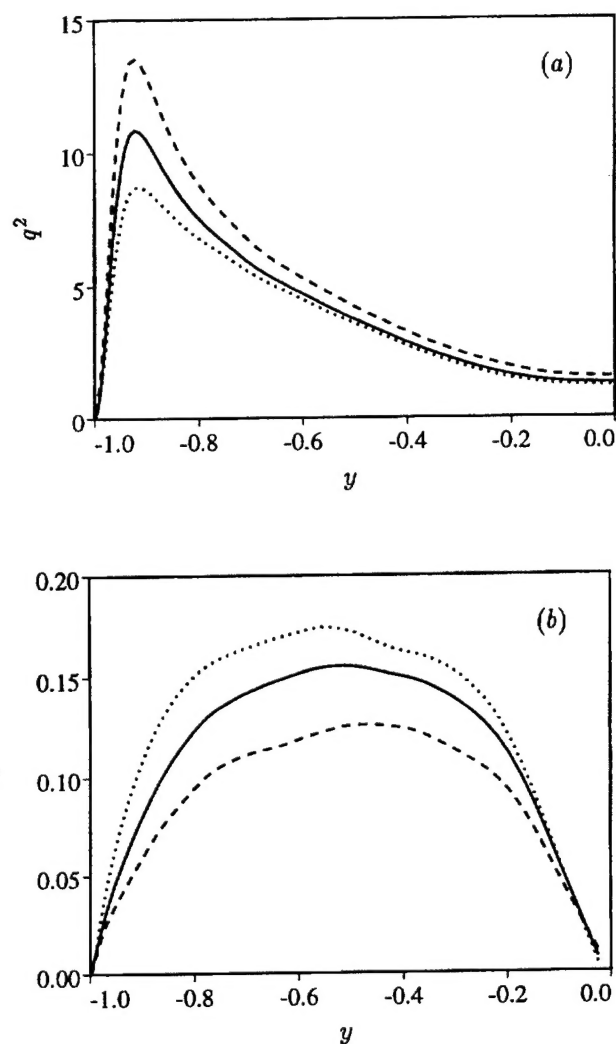


Figure 14 Profiles of (a) q^2 and (b) structure parameter for Cases TS1 and TS2; symbols as in Figure 13

shears on, for example, enstrophy profiles implies that nonequilibrium boundary layers produced by an abrupt mean-flow change are sensitive to the type—and not just the suddenness—of that change. Investigation of the pressure-driven flow using strained-channel simulations has begun to yield insight into differences between the two main versions of 3DBLs. In the future, we plan to continue this effort by considering less-rapid strain rates than that imposed here and utilize initial fields aligned at various orientations in order to isolate adverse pressure gradient and pure-skewing effects. An attempt will also be made to determine the Reynolds number dependence of our conclusions regarding the shear-driven 3DBL by performing large-eddy simulations of the moving-wall flow.

Acknowledgments

This work is sponsored by the Office of Naval Research (Program Officer, L. P. Purtell). Computer resources have been supplied by the NAS program at NASA-Ames Research Center and by the San Diego Supercomputer Center. We have benefited from discussions with P. Spalart and P. Bradshaw and T. Gotoh.

References

- Bradshaw, P. 1987. Turbulent secondary flows. *Annu. Rev. Fluid Mech.*, **19**, 53-74
- Bradshaw, P. and Pontikos, N. S. 1985. Measurements in the turbulent boundary layer on an "infinite" swept wing. *J. Fluid Mech.*, **159**, 105-130
- Driver, D. M. and Hebbbar, S. K. 1991. Three-dimensional turbulent boundary-layer flow over a spinning cylinder. NASA TM 102240
- Eaton, J. K. 1995. Effects of mean flow three-dimensionality on turbulent boundary-layer structure. *AIAA J.*, **33**, 2020-2025
- Furuya, Y., Nakamura, I. and Kawachi, H. 1966. The experiment on the skewed boundary layer on a rotating body. *Bull. Japan. Soc. Mech. Eng.*, **9**, 702-710
- Jiménez, J. and Moin, P. 1991. The minimal flow unit in near-wall turbulence. *J. Fluid Mech.*, **225**, 213-240
- Jung, W. J., Mangiavacchi, N. and Akhavan, R. 1992. Suppression of turbulence in wall-bounded flows by high-frequency spanwise oscillations. *Phys. Fluids*, **4**, 1605-1607
- Kim, J., Moin, P. and Moser, R. 1987. Turbulence statistics in fully developed channel flow at low-Reynolds number. *J. Fluid Mech.*, **177**, 133-166
- Laadhari, F., Skandaji, L. and Morel, R. 1994. Turbulence reduction in a boundary layer by a local spanwise oscillating surface. *Phys. Fluids*, **6**, 3218-3220
- Lohmann, R. P. 1976. The response of a developed turbulent boundary layer to local transverse surface motion. *J. Fluids Eng.*, **98**, 354-363
- Moin, P., Shih, T.-H., Driver, D. M. and Mansour, N. N. 1990. Direct numerical simulation of a three-dimensional turbulent boundary layer. *Phys. Fluids*, **2**, 1846-1853
- Rogallo, R. S., 1981. Numerical experiments in homogeneous turbulence. NASA TM 81315
- Schwarz, W. R. and Bradshaw, P. 1994. Turbulence structural changes for a three-dimensional turbulent boundary layer in a 30° bend. *J. Fluid Mech.*, **272**, 183-209
- Sendstad, O. and Moin, P. 1992. The near-wall mechanics of three-dimensional turbulent boundary layers. Report No. TF-57, Thermosciences Div., Dept. Mech. Engr., Stanford Univ., Stanford, CA